Charles University in Prague
Faculty of Mathematics and Physics

ELECTROMAGNETIC INDUCTION IN A HETEROGENEOUS EARTH'S MANTLE: TIME-DOMAIN MODELLING

Jakub Velímský

Prague 2003

Charles University in Prague
Faculty of Mathematics and Physics

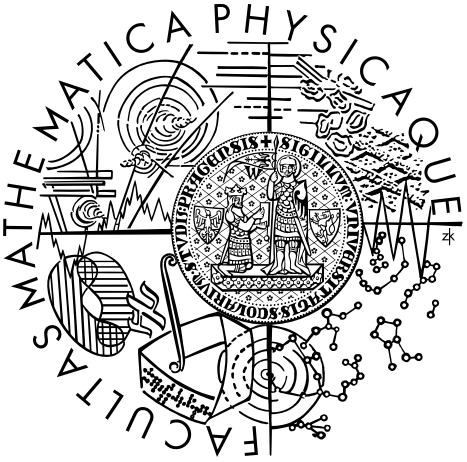

ELECTROMAGNETIC INDUCTION IN A HETEROGENEOUS EARTH'S MANTLE: TIME-DOMAIN MODELLING

Jakub Velímský
Ph.D. thesis
Supervisor: Zdeněk Martinec

Department of Geophysics
V Holešovičkách 2
180 00 Praha 8
Czech Republic

mámě a tátovi

Děkuji svému školiteli Zdeňku Martincovi za veškerou pomoc, radu, motivaci i kritiku, kterých se mi od něj v průběhu mého studia hojně dostávalo. Děkuji také Jiřímu Zahradníkovi, Ctiradu Matyskovi, Ladislavu Hanykovi i ostatním kolegům z Katedry geofyziky MFF UK za báječnou atmosféru, která zde panuje.
I thank Mark Everett for his help, motivation, and for fruitful discussions we had during my staying at Texas A&M.

Contents

Chapter 1

Introduction

1.1 EM induction as a tool for Earth's mantle studies

Studies of the electrical conductivity are an important constraint on the physical properties of the Earth's mantle. The electrical conductivity is particularly sensitive to temperature, chemical composition of mantle rocks and minerals, and to the presence of interstitial fluids in the form of aqueous phases or partial melts. Our knowledge of the conductivity distribution complements the information provided by seismology, simulations of thermochemical mantle convection, geoid studies, laboratory measurements, and other geophysical disciplines in the efforts to understand the physical processes in the mantle.

The response of the conductive Earth's mantle to long-periodic variations of the ionospheric and magnetospheric currents represents the most effective way to determine the mantle conductivity and it has been intensively studied for a long time. The first inversions of the geomagnetic variations measured at the surface assumed a spherically symmetric distribution of conductivity in the Earth's mantle (Price, 1930; Lahiri & Price, 1939; Rikitake, 1950; Banks, 1969).

Results obtained by mantle convection modelling and by the 3-D seismic tomography suggest that the lateral variations of temperature in the mantle are of orders of 10^2–10^3 K on the scales of 10^2–10^3 km (Duffy & Hemley, 1995). These results and the laboratory measurements of conductivity under mantle pressure and temperature conditions (e.g. Shankland et al., 1993; Xu et al., 1998, 2000) yield that the lateral conductivity variations of orders of magnitude can be expected in the mantle. Local 1-D interpretations of carefully processed data strongly support this idea. Schultz & Larsen (1987) demonstrated that no single 1-D conductivity model is compatible with geomagnetic responses observed at geographically distributed observatories. The existence of lateral conductivity variations in the upper and mid-mantle has been confirmed in other local 1-D and regional studies (Roberts, 1984; Schultz & Larsen, 1990; Schultz, 1990; Petersons & Anderssen, 1990; Tarits, 1994; Olsen, 1998; Semenov, 1998, a.o.).

These results represented a strong motivation for the development of efficient forward solvers of the electromagnetic (EM) induction problem in a radially and laterally inhomogeneous Earth's mantle. A brief overview of these solvers using various mathematical approaches and numerical methods is given in the next section.

One of the main obstacles in the inversion of the ground based long-periodic data to reveal a 3-D conductivity structure is the uneven spatial distribution of the geomagnetic observatories, especially the poor coverage of the oceanic areas. On the other hand, the satellite magnetometer data such as those obtained from the MAGSAT, Ørsted and CHAMP spacecrafts have excellent spatial coverage and offer an unprecedented opportunity to improve our knowledge of electrical conductivity in the Earth's mantle.

The problem of EM induction in the mantle is traditionally approached in the frequency domain. The equation of EM induction is solved with the assumption of harmonic signals at discrete frequencies usually from the range of 10^{-2}–10^{0} cpd, covering the spectrum that corresponds to solar quiet (Sq), and disturbed (Dst) geomagnetic variations. However, the transient signals, such as magnetic storms, are sources of strong induction effects in the mantle due to abrupt changes of the system of external inducing electrical currents in the ionosphere and magnetosphere. It is inconvenient to study the Earth's response to transient signals in the frequency domain because they have a broad spectrum. Moreover, the complicated spatio-temporal distribution of satellite data favors a time-domain approach.

In this work we present two different time-domain approaches to the forward EM induction problem in a heterogeneous mantle. The spectral-finite element method introduced in Chapter 2 uses a traditional parameterization by spherical harmonic function. Chapter 3 introduces an approach based on the 3-D finite element discretization, a method common in the world of electrical engineering. In Chapter 4 which is the extended version of a GRL paper (Velímský et al., 2003) we employ the former method to compute the response of a realistic 3-D model of mantle conductivity to a transient signal with simplified spatial structure and realistic time evolution.

1.2 Overview of previous 3-D approaches

The development of forward solvers of the EM induction problem in a spherical Earth with laterally varying conductivity has been subject of active research recently. Following the traditional frequency-domain approach, Fainberg et al. (1990) assumed a thin heterogeneous conductive sheet representing the high contrast between conducting oceans and resistive continents with underlying radially stratified medium. The problem was formulated as an integral equation for surface currents in the sheet and solved by means of an iterative-dissipative method. The method was later generalized for an arbitrary position of the heterogeneous thin sheet in the spherically symmetric Earth (Kuvshinov & Pankratov, 1994).

Zhang & Schultz (1992) developed a perturbation method for a radially symmetric conductivity model superposed by small lateral heterogeneities. The magnetic field was expressed in terms of toroidal and poloidal modes which were expanded into perturbation

series truncated at 2. The zero-th, first, and second order terms were parameterized by spherical harmonic functions and finite differencing was used to solve the ordinary differential equations with respect to radius.

Everett & Schultz (1996) applied the finite element method to the problem formulated in terms of electromagnetic potentials in the mantle and surrounding insulating atmosphere. The tetrahedralization of the sphere was based on Delauney triangulation of a spherical surface, piecewise linear nodal finite elements were used to parameterize the potentials, and iterative refinement scheme with incomplete LU factorization was used to solve the sparse linear system.

Martinec (1999a) formulated the problem in the integral sense for the magnetic induction vector $\boldsymbol{B}$. Using vector spherical harmonic functions and piecewise linear elements for angular and radial parameterization, respectively, he constructed a complex sparse linear system that was solved by biconjugate gradient iteration. An efficient preconditioner was based on a spherically symmetric conductivity profile. The original formulation prescribed the boundary condition on the Earth's surface in terms of total toroidal electrical intensity. However, the method was later modified in such a way that the Gauss coefficient of the external inducing field can be prescribed on the Earth's surface.

A staggered-grid finite difference method was implemented by Uyeshima & Schultz (2000). The computational domain was divided into curved rectangular H-prisms with a constant conductivity value assigned to each one. The integral form of the Ampère law for magnetic intensity $\boldsymbol{H}$ was cast in each H-prism, while the integral form of the Faraday law for electrical intensity $\boldsymbol{E}$ was cast in staggered E-prisms whose vertices were positioned in centers of the H-prisms. The sparse linear system was solved using the minimum residual conjugate gradient algorithm with incomplete Cholesky preconditioning. The computational domain enclosed the conductive mantle as well as the atmosphere which was approximated by prescribing a small conductivity value.

An edge-based finite element formulation was introduced by Yoshimura & Oshiman (2002). This parameterization allowed to formulate the problem in terms of only one vector magnetic potential.

The time-domain approach to the EM induction problem was recently applied by Hamano (2002). The problem was formulated in terms of poloidal and toroidal functions. Spherical harmonic expansion and finite differences were used in the angular and radial parameterization, respectively. The Crank-Nicolson scheme was employed for the time integration.

Concurrently with the development of the 3-D methods, the question of their testing and validation was addressed. Everett & Schultz (1995) introduced a semi-analytical frequency-domain solution for a conductivity model consisting of a homogeneous host sphere and a homogeneous spherical inclusion nested eccentrically on the axis of symmetry z. Martinec (1998) generalized the solution to the case of multiple off-axis sub-

sequently nested spheres. The spectral-finite element approach to the axially symmetric 2-D EM induction was implemented by Martinec (1997) and Martinec et al. (2002) in the frequency-domain and time-domain, respectively.

Chapter 2

Time-domain, spectral-finite element approach

2.1 Formulation of the initial-value problem

2.1.1 Classical formulation

Let us start with notation and basic assumptions. By $\boldsymbol{r}$ we denote the position vector which is further expressed by spherical coordinates $\boldsymbol{r} = (r, \Omega) = (r, \vartheta, \varphi)$. We approximate the Earth by a sphere G with surface ∂G of radius a. We assume that the sphere G has constant magnetic permeability μ_0 and positive, finite, continuous 3-D varying electrical conductivity $\sigma(\boldsymbol{r}) \in L^+_\infty(G) \cap C^1(G)$ (see Appendix F.2 for a summary of used functional spaces). It is also useful to introduce the electrical resistivity $\rho(\boldsymbol{r}) = 1/\sigma(\boldsymbol{r})$, $\rho(\boldsymbol{r}) \in L^+_\infty(G) \cap C^1(G)$. The magnetic field in G is induced by time-varying electrical currents $\boldsymbol{j}^{(e)}$ in the ionosphere and the magnetosphere which are separated from the Earth by a perfectly insulating spherical atmosphere A. The model configuration is sketched in Figure 2.1. The characteristic time scales of the external current variations range from several hours to hundreds of days, so the quasi-static approximation of Maxwell's equations is applicable.

Under these assumptions, the equation of electromagnetic induction can be derived directly from Maxwell's equations (Parkinson & Hutton, 1989):

$$\mu_0 \frac{\partial \boldsymbol{B}}{\partial t} + \operatorname{curl}(\rho \operatorname{curl} \boldsymbol{B}) = 0 \quad \text{in } G, \tag{2.1}$$

where $\boldsymbol{B}(\boldsymbol{r}; t) \in C^2(G)^3 \times C^1(\langle 0, \infty \rangle))^3$ is the vector of magnetic induction. Equation (2.1) is a parabolic differential equation. The initial value and the boundary value conditions of $\boldsymbol{B}$ have to be specified. The initial value ${}^0\boldsymbol{B}$ at time $t = 0$ is specified by a function from $C^2(G)^3$ that satisfies the divergence-free condition

$$\operatorname{div} {}^0\boldsymbol{B} = 0 \quad \text{in } G. \tag{2.2}$$

Applying the divergence operator on equation (2.1) yields

$$\frac{\partial(\operatorname{div} \boldsymbol{B})}{\partial t} = 0 \quad \text{in } G. \tag{2.3}$$

Equation (2.3) and the choice of ${}^0\boldsymbol{B}$ in accordance with (2.2) assure that $\operatorname{div} \boldsymbol{B} = 0$ at any time $t > 0$, i.e. the divergence-free condition on $\boldsymbol{B}$ is implicitly satisfied by the equation of electromagnetic induction (2.1).

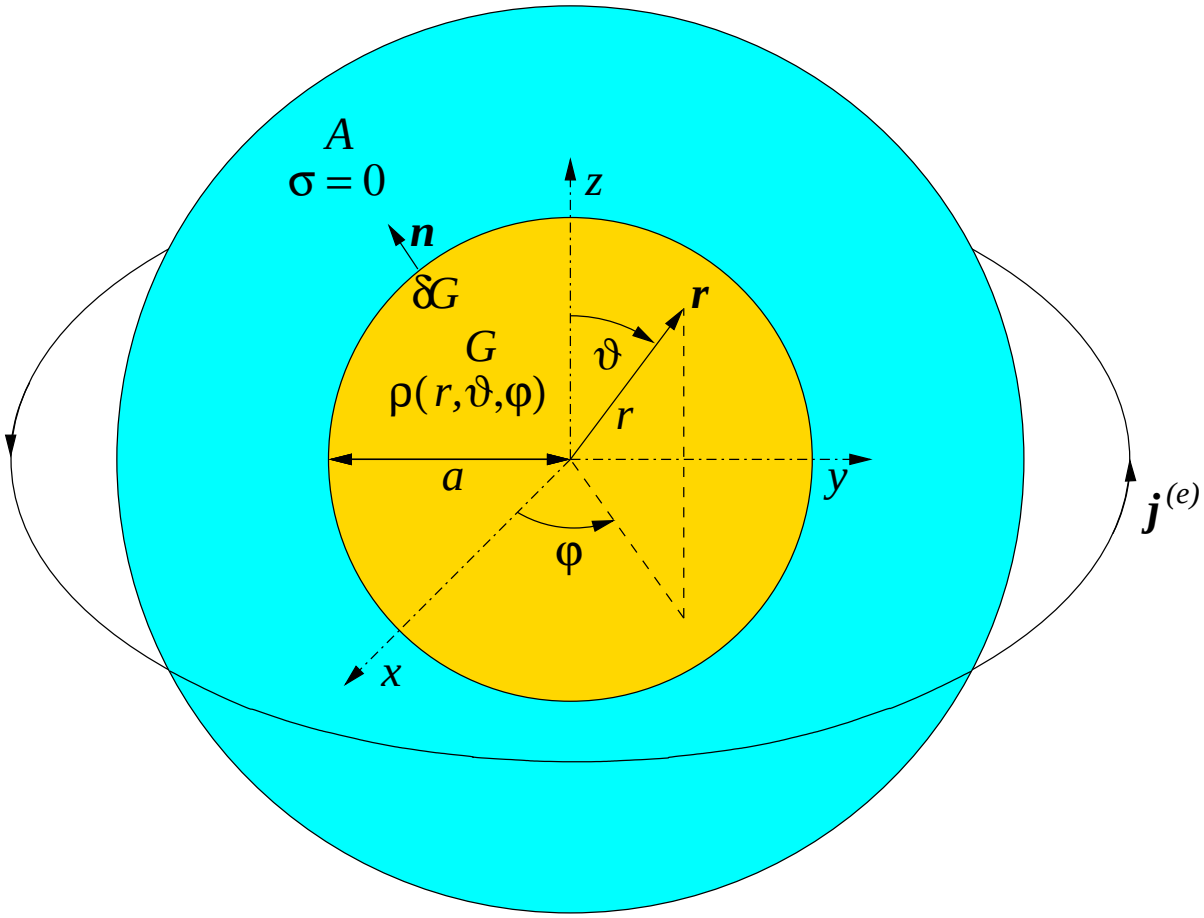

Figure 2.1: A schematic figure of model configuration. Heterogeneous conductive sphere G of radius a with surface ∂G is surrounded by an insulating spherical layer A. Above A, a system of primary inducing electrical currents $\boldsymbol{j}^{(e)}$ is prescribed.

The general form of the boundary conditions imposed on the magnetic field by Maxwell's equations on any material interface is,

$$[\boldsymbol{n} \cdot \boldsymbol{B}]_-^+ = 0, \tag{2.4}$$

$$[\boldsymbol{n} \times \boldsymbol{H}]_-^+ = \boldsymbol{j}_S, \tag{2.5}$$

where $\boldsymbol{H}$, $\boldsymbol{j}_S$, and $\boldsymbol{n}$ are the magnetic intensity vector, the density of free surface currents, and the unit normal vector on the interface, respectively. Because of the assumption of constant magnetic permeability μ_0 in the material relation

$$\boldsymbol{B} = \mu_0 \boldsymbol{H}, \tag{2.6}$$

and because no free surface currents are generated on the surfaces of finitely conducting, or insulating bodies, the boundary conditions imposed on $\boldsymbol{B}$ on ∂G reduce to

$$[\boldsymbol{B}]^{+}_{-} = 0. \tag{2.7}$$

The magnetic induction vector $\boldsymbol{B}$ changes continuously across the spherical surface ∂G.

The magnetic induction in the insulating atmosphere A is a divergence-free and irrotational field, and can be represented at any time $t \geq 0$ by a gradient of scalar magnetic potential $U(\boldsymbol{r};t)$,

$$\boldsymbol{B}(\boldsymbol{r};t) = -\mathrm{grad}\, U(\boldsymbol{r};t) \quad \text{in } A, \tag{2.8}$$

where U satisfies the Laplace equation,

$$\nabla^2 U(\boldsymbol{r};t) = 0 \quad \text{in } A. \tag{2.9}$$

Expanding the magnetic potential into a series of spherical harmonics $Y_{jm}(\Omega)$ (Varshalovich et al., 1989) allows us to write the analytical solution of (2.9) as a sum of two parts,

$$U = U^{(e)} + U^{(i)}. \tag{2.10}$$

The external part,

$$U^{(e)}(\boldsymbol{r};t) = a \sum_{j=1}^{\infty} \sum_{m=-j}^{j} G^{(e)}_{jm}(t) \left(\frac{r}{a}\right)^{j} Y_{jm}(\Omega), \tag{2.11}$$

represents the magnetic field induced by ionospheric and magnetospheric currents $\boldsymbol{j}^{(e)}$ above the atmospheric layer A. The internal part,

$$U^{(i)}(\boldsymbol{r};t) = a \sum_{j=1}^{\infty} \sum_{m=-j}^{j} G^{(i)}_{jm}(t) \left(\frac{a}{r}\right)^{j+1} Y_{jm}(\Omega), \tag{2.12}$$

represents the magnetic field of induced currents inside the sphere G (e.g., Langel, 1987). Substituting from (2.10), (2.11), and (2.12) into (2.8), and taking into account the formula for gradient of spherical harmonic functions (A 15), yields

$$\boldsymbol{B}(\boldsymbol{r};t) = \boldsymbol{B}^{(e)}(\boldsymbol{r};t) + \boldsymbol{B}^{(i)}(\boldsymbol{r};t) \quad \text{in } A, \tag{2.13}$$

where

$$\boldsymbol{B}^{(e)}(\boldsymbol{r};t) = -\sum_{jm} G^{(e)}_{jm}(t) \left(\frac{r}{a}\right)^{j-1} \left[j\, \boldsymbol{S}^{(-1)}_{jm}(\Omega) + \boldsymbol{S}^{(1)}_{jm}(\Omega)\right], \tag{2.14}$$

$$\boldsymbol{B}^{(i)}(\boldsymbol{r};t) = \sum_{jm} G^{(i)}_{jm}(t) \left(\frac{a}{r}\right)^{j+2} \left[(j+1)\, \boldsymbol{S}^{(-1)}_{jm}(\Omega) - \boldsymbol{S}^{(1)}_{jm}(\Omega)\right]. \tag{2.15}$$

The vector spherical harmonic functions $\boldsymbol{S}^{(\lambda)}_{jm}(\Omega)$, $\lambda = -1, 0, 1$, are introduced in Appendix A. The limits in the sums over j and m remain the same as in equation (2.11) and will be omitted from now on. The downward, northward, and eastward components of magnetic induction in the atmosphere can be derived from the definitions (A 4–A 6),

$$\begin{aligned} Z(\boldsymbol{r};t) &= -\boldsymbol{e}_r \cdot \boldsymbol{B}(\boldsymbol{r};t) = \\ &= \sum_{jm} \left[j\, G^{(e)}_{jm}(t) \left(\frac{r}{a}\right)^{j-1} - (j+1)\, G^{(i)}_{jm}(t) \left(\frac{a}{r}\right)^{j+2} \right] Y_{jm}(\Omega), \qquad (2.16) \\ X(\boldsymbol{r};t) &= -\boldsymbol{e}_\vartheta \cdot \boldsymbol{B}(\boldsymbol{r};t) = \\ &= \sum_{jm} \left[G^{(e)}_{jm}(t) \left(\frac{r}{a}\right)^{j-1} + G^{(i)}_{jm}(t) \left(\frac{a}{r}\right)^{j+2} \right] \frac{\partial Y_{jm}}{\partial \vartheta}(\Omega), \qquad (2.17) \\ Y(\boldsymbol{r};t) &= \boldsymbol{e}_\varphi \cdot \boldsymbol{B}(\boldsymbol{r};t) = \\ &= \frac{-1}{\sin\vartheta} \sum_{jm} \left[G^{(e)}_{jm}(t) \left(\frac{r}{a}\right)^{j-1} + G^{(i)}_{jm}(t) \left(\frac{a}{r}\right)^{j+2} \right] \frac{\partial Y_{jm}}{\partial \varphi}(\Omega). \qquad (2.18) \end{aligned}$$

The unit vectors corresponding to the radial coordinate r, colatitude ϑ, and longitude φ, are denoted by $\boldsymbol{e}_r$, $\boldsymbol{e}_\vartheta$, and $\boldsymbol{e}_\varphi$. Spherical harmonic coefficients of the external and internal potential, $G^{(e)}_{jm}(t)$ and $G^{(i)}_{jm}(t)$, can be determined from components X, Y, Z measured at ground based observatories or at a low-altitude satellite orbit. This problem, although important in 3-D inversions for the conductivity structure, is not discussed in this work.

To express the boundary condition at the Earth's surface, we expand the magnetic induction vector inside the sphere G into a series of vector spherical harmonics,

$$\boldsymbol{B}(r,\Omega;t) = \sum_{j=1}^{\infty} \sum_{m=-j}^{j} \sum_{\lambda=-1}^{1} B^{(\lambda)}_{jm}(r;t)\, \boldsymbol{S}^{(\lambda)}_{jm}(\Omega), \qquad (2.19)$$

where $B^{(\lambda)}_{jm}(r;t)$ are complex functions of radius and time. Because we use complex parameterization to represent real functions, the property (A 11) of the spherical harmonics yields

$$B^{(\lambda)}_{j\,-m}(r;t) = (-1)^m \overline{B}^{(\lambda)}_{jm}(r;t). \qquad (2.20)$$

Assuming the continuity of $\boldsymbol{B}$ for $r = a$ in equations (2.13–2.15) and (2.19) leads to

$$\begin{aligned} B^{(0)}_{jm}(a;t) &= 0, \qquad (2.21) \\ B^{(-1)}_{jm}(a;t) &= -\left[j\, G^{(e)}_{jm}(t) - (j+1)\, G^{(i)}_{jm}(t) \right], \qquad (2.22) \\ B^{(1)}_{jm}(a;t) &= -\left[G^{(e)}_{jm}(t) + G^{(i)}_{jm}(t) \right]. \qquad (2.23) \end{aligned}$$

The spherical harmonic coefficients appropriate to the toroidal part, $B_{jm}^{(0)}$, vanish at the boundary ∂G, the external and internal parts of the magnetic potential are present in the vertical spheroidal components $B_{jm}^{(-1)}$ and in the horizontal spheroidal components $B_{jm}^{(1)}$. By eliminating $G_{jm}^{(i)}(t)$ from (2.22) and (2.23), we can reduce the boundary conditions to

$$B_{jm}^{(0)}(a;t) = 0, \tag{2.24}$$

$$B_{jm}^{(-1)}(a;t) + (j+1)\, B_{jm}^{(1)}(a;t) = -(2j+1)\, G_{jm}^{(e)}(t). \tag{2.25}$$

The boundary conditions (2.24–2.25) are connected to the spherical harmonic expansion of $\boldsymbol{B}$, and cannot be expressed as simple Dirichlet or Neumann boundary conditions imposed on $\boldsymbol{B}$. Therefore, they are difficult to implement in other numerical schemes, such as 3-D finite elements, or 3-D finite differences. In such cases, the Laplace equation (2.9) is solved numerically, and boundary condition on potential U is prescribed on the outer surface of A. This approach is implemented in the 3-D finite element approach in Chapter 3, see also Everett & Schultz (1996) and Uyeshima & Schultz (2000). However, using the orthogonality of the spherical harmonic functions (A 8), it is possible to reformulate equations (2.24–2.25) as a set of integral equations

$$\int_{\Omega} \boldsymbol{B}(a,\Omega;t) \cdot \overline{\boldsymbol{S}}_{jm}^{(0)}(\Omega)\, d\Omega = 0, \tag{2.26}$$

$$\int_{\Omega} \boldsymbol{B}(a,\Omega;t) \cdot \left[\overline{\boldsymbol{S}}_{jm}^{(-1)}(\Omega) + \frac{1}{j}\, \overline{\boldsymbol{S}}_{jm}^{(1)}(\Omega) \right] d\Omega = -(2j+1)\, G_{jm}^{(e)}(t) \tag{2.27}$$

which hold for each $j \geq 1$ and m, such that $|m| \leq j$. Bar denotes complex conjugation.

Now we can finally summarize the formulation of the electromagnetic induction problem in the time-domain in the classical sense:

Let $\mu_0 > 0$ and $\rho(\boldsymbol{r}) \in L_{\infty}^{+}(G) \cap C^1(G)$. Let the initial value ${}^0\boldsymbol{B}(\boldsymbol{r}) \in C^2(G)^3$ be a divergence-free function, $\operatorname{div} {}^0\boldsymbol{B} = 0$ in G. Let $U^{(e)}(r,\Omega;t)$ be the external part of magnetic potential in the atmosphere defined by (2.11). Find such a function $\boldsymbol{B}(\boldsymbol{r};t) \in C^2(G)^3 \times C^1\left(\langle 0,\infty)\right)^3$ that satisfies

$$\mu_0 \frac{\partial \boldsymbol{B}}{\partial t} + \operatorname{curl}\left(\rho \operatorname{curl} \boldsymbol{B}\right) = 0 \quad \text{in } G, \tag{2.28}$$

$$\boldsymbol{B}(\boldsymbol{r};0) = {}^0\boldsymbol{B}(\boldsymbol{r}) \quad \text{in } G, \tag{2.29}$$

$$\tag{2.30}$$

and $\forall j \geq 1,\ |m| \leq j$,

$$\int_\Omega \boldsymbol{B}(a,\Omega;t) \cdot \overline{\boldsymbol{S}}^{(0)}_{jm}(\Omega)\, d\Omega = 0, \tag{2.31}$$

$$\int_\Omega \boldsymbol{B}(a,\Omega;t) \cdot \left[\overline{\boldsymbol{S}}^{(-1)}_{jm}(\Omega) + \frac{1}{j}\, \overline{\boldsymbol{S}}^{(1)}_{jm}(\Omega) \right] d\Omega = -(2j+1)\, G^{(e)}_{jm}(t). \tag{2.32}$$

It is also possible to extend the classical formulation (2.28–2.32) to the case of discontinuous resistivity in G. Let us assume internal surfaces Γ_i, where resistivity $\rho(\boldsymbol{r})$ changes discontinuously, separating the sphere G into subdomains G_i, where $\rho(\boldsymbol{r})$ is continuous. Then the equation (2.28) holds in each subdomain G_i, and continuity of $\boldsymbol{B}$ (2.7) is imposed on the internal interfaces Γ_i.

2.1.2 Integral (weak) formulation

To reformulate the problem of electromagnetic induction in a heterogeneous sphere in the integral sense, we introduce the solution spaces H_{curl}, $H_{\mathrm{curl},0}$ (Křížek & Neittaanmäki, 1990), and the L_2 scalar product $(\cdot,\cdot)$ (see Appendix F.2). Then we can pose the problem as follows:

Let $\mu_0 > 0$ and $\rho(\boldsymbol{r}) \in L^+_\infty(G)$. Let the initial value ${}^0\boldsymbol{B}(\boldsymbol{r}) \in H_{\mathrm{curl}}$ be a divergence-free function, $\operatorname{div} {}^0\boldsymbol{B} = 0$ in G. Let $U^{(e)}(r,\Omega;t)$ be the external part of magnetic potential in the atmosphere defined by (2.11). Find $\boldsymbol{B}(\boldsymbol{r};t) \in H_{\mathrm{curl}} \times C^1\left(\langle 0,\infty)\right)^3$, such that

$$\mu_0 \left(\frac{\partial \boldsymbol{B}}{\partial t}, \delta\boldsymbol{B} \right) + a(\boldsymbol{B}, \delta\boldsymbol{B}) = 0 \quad \forall\, \delta\boldsymbol{B} \in H_{\mathrm{curl},0}, \tag{2.33}$$

$$\boldsymbol{B}(\boldsymbol{r};0) = {}^0\boldsymbol{B}(\boldsymbol{r}) \quad \text{in } G, \tag{2.34}$$

and $\forall j \geq 1,\ |m| \leq j$,

$$\int_\Omega \boldsymbol{B}(a,\Omega;t) \cdot \overline{\boldsymbol{S}}^{(0)}_{jm}(\Omega)\, d\Omega = 0, \tag{2.35}$$

$$\int_\Omega \boldsymbol{B}(a,\Omega;t) \cdot \left[\overline{\boldsymbol{S}}^{(-1)}_{jm}(\Omega) + \frac{1}{j}\, \overline{\boldsymbol{S}}^{(1)}_{jm}(\Omega) \right] d\Omega = -(2j+1)\, G^{(e)}_{jm}(t). \tag{2.36}$$

The sesquilinear form $a(\cdot,\cdot)$ is defined as

$$a(\boldsymbol{B},\delta\boldsymbol{B}) = \int_G \rho(\operatorname{curl}\boldsymbol{B})\cdot(\operatorname{curl}\delta\boldsymbol{B})\,dV. \tag{2.37}$$

Let us show that if there exists a weak solution of (2.33–2.36), such that $\boldsymbol{B}\in C^2(G)^3\times C^1\left(\langle 0,\infty)\right)^3$, for $\rho\in C^1(G)$ and ${}^0\boldsymbol{B}\in C^2(G)^3$, it is also the classical solution of (2.28–2.32). Since $C^2(G)^3\subset H_{\mathrm{curl}}$, we can take $\delta\boldsymbol{B}\in C^2(G)$, such that $\boldsymbol{e}_r\times\delta\boldsymbol{B}=0$ on ∂G, and apply on (2.33) Green's theorem,

$$\int_G \operatorname{curl}\,(h\operatorname{curl}\boldsymbol{f})\cdot\boldsymbol{g}\,dV = \int_G h\,(\operatorname{curl}\boldsymbol{f})\cdot(\operatorname{curl}\boldsymbol{g})\,dV - \int_{\partial G} h\,(\operatorname{curl}\boldsymbol{f})\cdot(\boldsymbol{e}_r\times\boldsymbol{g})\,dS, \tag{2.38}$$

valid for any $h\in C^1(G)$, $\boldsymbol{f},\boldsymbol{g}\in C^2(G)^3$. The surface integral is canceled because of the choice of $\delta\boldsymbol{B}$, and we are left with

$$\int_G \left[\mu_0\frac{\partial\boldsymbol{B}}{\partial t} + \operatorname{curl}\,(\rho\operatorname{curl}\boldsymbol{B})\right]\cdot\delta\boldsymbol{B}\,dV = 0. \tag{2.39}$$

This can be satisfied for all $\delta\boldsymbol{B}\in C^2(G)$, $\boldsymbol{e}_r\times\delta\boldsymbol{B}=0$ on ∂G, only if

$$\mu_0\frac{\partial\boldsymbol{B}}{\partial t} + \operatorname{curl}\,(\rho\operatorname{curl}\boldsymbol{B}) = 0 \quad \text{in } G. \tag{2.40}$$

The integral formulation also implicitly satisfies the divergence-free constraint on $\boldsymbol{B}$. Let us introduce an auxiliary function $\xi\in D^0(G)$, and construct a particular test functions $\delta\boldsymbol{B}=\operatorname{grad}\xi$. Note that $\delta\boldsymbol{B}\in H_{\mathrm{curl},0}$ because $\operatorname{grad}\xi\in L_2(G)^3$, $\operatorname{curl}\operatorname{grad}\xi=0$, and $\boldsymbol{e}_r\times\operatorname{grad}\xi=0$ on ∂G. Then equation (2.33) yields

$$\int_G \frac{\partial\boldsymbol{B}}{\partial t}\cdot\operatorname{grad}\xi\,dV = 0 \quad \forall\,\xi\in D^0(G). \tag{2.41}$$

Because $H_{\mathrm{curl}}\subset L_2(G)^3$ and $D^0(G)\subset L_2(G)$, we can use another Green's theorem which holds for any square integrable scalar h and vector $\boldsymbol{f}$,

$$\int_G \boldsymbol{f}\cdot\operatorname{grad}h\,dV = -\int_G (\operatorname{div}\boldsymbol{f})\,h\,dV + \int_{\partial G}(\boldsymbol{e}_r\cdot\boldsymbol{f})\,h\,dS. \tag{2.42}$$

The surface integral is zero because $\xi = 0$ on ∂G, and the time and space derivatives are interchangeable, therefore we can write

$$\int_G \frac{\partial(\operatorname{div} \boldsymbol{B})}{\partial t}\, \xi \, dV = 0 \quad \forall\, \xi \in D^0(G). \tag{2.43}$$

This can be satisfied only with

$$\frac{\partial(\operatorname{div} \boldsymbol{B})}{\partial t} = 0 \quad \text{in}\, G. \tag{2.44}$$

However, numerical errors can introduce spurious magnetic monopoles during the time integration. This can be avoided either by adding the divergence-free constraint to (2.33) in the form of the Lagrange multipliers (Martinec, 1999a), or by a projection to the divergence-free solution (Uyeshima & Schultz, 2000). Although a modified formulation of the presented method which uses the former approach to assure solenoidality of $\boldsymbol{B}$ was also developed, we have not observed any recognizable deviations from the divergence-free solution while testing the code for a wide selection of resistivity models and external source currents, and the constraint was dropped from the algorithm in favour of increased speed and lower memory requirements of the numerical method.

2.1.3 Time integration scheme

Implicit time integration schemes for solving parabolic differential equations are generally preferred to explicit ones (Press et al., 1992). However, with fully 3-D resistivity distribution, and due to the traditional spherical harmonic parameterization used in the angular coordinates, the form $a(\cdot,\cdot)$ leads to a very large matrix. Martinec (1999a) proposed a method for a fast iterative solution of such a system, but it would still require to compute many iterations at each level of the time discretization. We present a different, semi-implicit approach, based on splitting of the form $a(\cdot,\cdot)$ into two parts.

Let us express the resistivity as a sum of two components,

$$\rho(r,\Omega) = \rho_0(r) + \rho_1(r,\Omega), \tag{2.45}$$

where $\rho_0(r) \in L^+_\infty(G)$ is a spherically symmetric, finite, and positive resistivity model, and $\rho_1(r,\Omega)$ represents the deviations (not necessarily small) of the actual resistivity ρ from the spherically symmetric model. We experienced the best numerical results by prescribing ρ_0 as a maximum of ρ over angular coordinates,

$$\rho_0(r) \;\; = \;\; \max_\Omega \rho(r,\Omega). \tag{2.46}$$

Now we can split the sesquilinear form (2.37) into two parts corresponding to ρ_0 and ρ_1, respectively,

$$a(\boldsymbol{B}, \delta\boldsymbol{B}) = a_0(\boldsymbol{B}, \delta\boldsymbol{B}) + a_1(\boldsymbol{B}, \delta\boldsymbol{B}), \tag{2.47}$$

where

$$a_0(\boldsymbol{B}, \delta\boldsymbol{B}) = \int_G \rho_0(\operatorname{curl}\boldsymbol{B}) \cdot (\operatorname{curl}\delta\boldsymbol{B})\, dV, \tag{2.48}$$

$$a_1(\boldsymbol{B}, \delta\boldsymbol{B}) = \int_G \rho_1(\operatorname{curl}\boldsymbol{B}) \cdot (\operatorname{curl}\delta\boldsymbol{B})\, dV. \tag{2.49}$$

As we will show later, form $a_0(\cdot,\cdot)$ is represented by a banded matrix with 9 non-zero diagonals. Therefore, it is easy to treat it implicitly in the time integration scheme, while more complex form $a_1(\cdot,\cdot)$ is considered on the right hand side of equation (2.33), and is evaluated using the solution $\boldsymbol{B}$ from the previous time step.

Approximating the time derivative by the difference between the values of magnetic field at two following time steps,

$$\frac{\partial\boldsymbol{B}}{\partial t} \approx \frac{{}^{i+1}\boldsymbol{B} - {}^{i}\boldsymbol{B}}{\Delta t}, \tag{2.50}$$

where ${}^{i}\boldsymbol{B} = \boldsymbol{B}(\boldsymbol{r}; t_i) \in H_{\mathrm{curl}}$, and the time step $\Delta t = t_{i+1} - t_i$ is considered constant, we can formulate the time integration scheme as a sequence of elliptic problems with integral boundary conditions:

Find ${}^{i+1}\boldsymbol{B} \in H_{\mathrm{curl}}\ \forall\, i = 0, 1, \ldots$, such that

$$\frac{\mu_0}{\Delta t}\left({}^{i+1}\boldsymbol{B}, \delta\boldsymbol{B}\right) + a_0({}^{i+1}\boldsymbol{B}, \delta\boldsymbol{B}) = \frac{\mu_0}{\Delta t}\left({}^{i}\boldsymbol{B}, \delta\boldsymbol{B}\right) - a_1({}^{i}\boldsymbol{B}, \delta\boldsymbol{B}) \quad \forall\, \delta\boldsymbol{B} \in H_{\mathrm{curl},0}, \tag{2.51}$$

and $\forall j \geq 1,\ |m| \leq j$,

$$\int_\Omega {}^{i+1}\boldsymbol{B}(a, \Omega) \cdot \overline{\boldsymbol{S}}^{(0)}_{jm}(\Omega)\, d\Omega = 0, \tag{2.52}$$

$$\int_\Omega {}^{i+1}\boldsymbol{B}(a, \Omega) \cdot \left[\overline{\boldsymbol{S}}^{(-1)}_{jm}(\Omega) + \frac{1}{j}\,\overline{\boldsymbol{S}}^{(1)}_{jm}(\Omega)\right] d\Omega = -(2j+1)\, G^{(e)}_{jm}(t_{i+1}). \tag{2.53}$$

The initial value ${}^{0}\boldsymbol{B}$ from (2.34) is used on the right hand side of (2.51) for $i = 0$. Note that the solution ${}^{i+1}\boldsymbol{B}$ and the test functions $\delta\boldsymbol{B}$ are from different functional spaces H_{curl} and $H_{\mathrm{curl},0}$, respectively. The existence and uniqueness of the elliptic problem (2.51–2.53) are discussed in Appendix B.

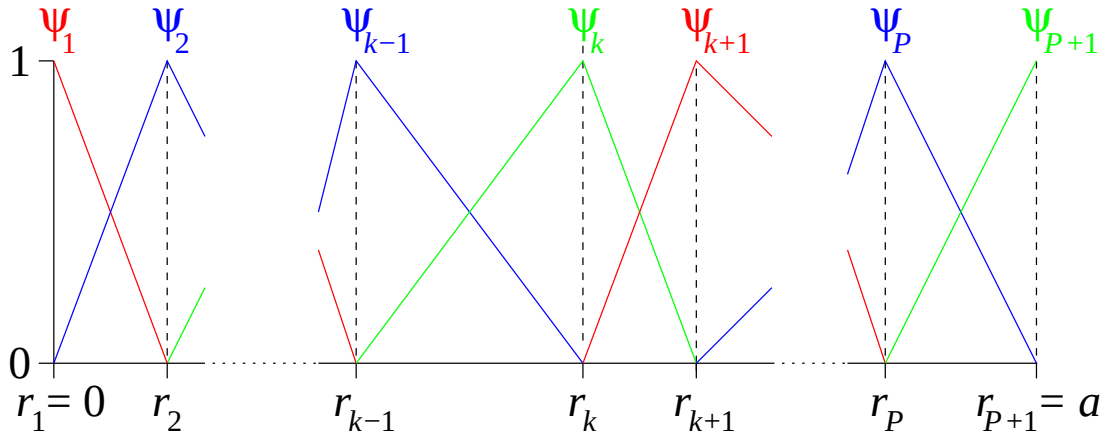

Figure 2.2: One-dimensional piecewise linear finite element functions.

2.1.4 Spherical harmonic-finite element parameterization

The expansion of the magnetic induction $\boldsymbol{B}$ into a series of vector spherical harmonics has been introduced by equation (2.19). To complete the spatial discretization of the problem (2.51–2.53), we need to define a parameterization over the radial coordinate. We use piecewise linear finite elements for this purpose. Let us divide the interval $\langle 0, a\rangle$ into P subintervals $\mathcal{I}_k = \langle r_k, r_{k+1}\rangle$, where $0 = r_1 < r_2 < \ldots < r_P < r_{P+1} = a$. In each interval $\mathcal{I}_k$, there are only two non-zero finite element functions, namely

$$\psi_k(r) = \frac{r_{k+1} - r}{h_k}, \qquad \psi_{k+1}(r) = \frac{r - r_k}{h_k}, \tag{2.54}$$

where $h_k = r_{k+1} - r_k$ is the length of the interval $\mathcal{I}_k$ (see Figure 2.2).

Now we are ready to introduce the discrete approximation of the functional space H_{curl},

$$H^h_{\mathrm{curl}} = \left\{ \boldsymbol{B} \,\middle|\, \boldsymbol{B} = \sum_{j=1}^{j_{max}} \sum_{m=-j}^{j} \sum_{k=1}^{P+1} \sum_{\lambda=-1}^{1} B^{(\lambda)}_{jm,k}\, \psi_k\, \boldsymbol{S}^{(\lambda)}_{jm} \right\}. \tag{2.55}$$

The spherical harmonic expansion is truncated at finite degree j_{max}. Note that the spherical harmonic coefficients $B^{(\lambda)}_{jm,k}$ must satisfy the discrete form of (2.20),

$$B^{(\lambda)}_{j\,-m,k} = (-1)^m \overline{B}^{(\lambda)}_{jm,k}, \tag{2.56}$$

since $\boldsymbol{B}$ is real. By excluding the basis functions $\psi_{P+1}\, \boldsymbol{S}^{(0)}_{jm}$ and $\psi_{P+1}\, \boldsymbol{S}^{(1)}_{jm}$ which have non-zero horizontal components at the surface we get an approximation of the space

$H_{\mathrm{curl},0}$,

$$H^h_{\mathrm{curl},0} = \left\{ \delta\boldsymbol{B} \,\middle|\, \delta\boldsymbol{B} = \sum_{jm} \left[\sum_{k=1}^{P} \sum_{\lambda=-1}^{1} \delta B^{(\lambda)}_{jm,k}\, \psi_k\, \boldsymbol{S}^{(\lambda)}_{jm} + \delta B^{(-1)}_{jm,P+1}\, \psi_{P+1}\, \boldsymbol{S}^{(-1)}_{jm} \right] \right\}. \quad (2.57)$$

The Galerkin approximation of the solution of (2.51–2.53) is then such a function ${}^{i+1}\boldsymbol{B} \in H^h_{\mathrm{curl}}$ that satisfies (2.51) for all test functions $\delta\boldsymbol{B} \in H^h_{\mathrm{curl},0}$, and the boundary conditions (2.52–2.53) for $j = 1, \ldots, j_{max}$, $m = 0, \ldots, j$.

Now we aim to derive the spherical harmonic-finite element approximations of the L_2 scalar product $(\cdot,\cdot)$, and of the sesquilinear forms $a_0(\cdot,\cdot)$ and $a_1(\cdot,\cdot)$. Since $\boldsymbol{B}$ is a real function, we can replace it by complex conjugation and make use of the orthogonality of the spherical harmonics (A 8). Separating the radial and angular parts of the volume integral, $\int_G dV = \int_0^a r^2\, dr \int_\Omega d\Omega$, and substituting for $\boldsymbol{B}$ and $\delta\boldsymbol{B}$ the basis functions $\psi_k(r)\, \boldsymbol{S}^{(\lambda)}_{jm}(\Omega)$, yields for the L_2 scalar product,

$$\left(\psi_k\, \overline{\boldsymbol{S}}^{(\lambda)}_{jm}, \psi_{k'}\, \boldsymbol{S}^{(\lambda')}_{j'm'}\right) = \delta_{jj'}\, \delta_{mm'}\, \delta_{\lambda\lambda'}\, N_{j\lambda} \left[I^{(2)}_k\, \delta_{k(k'-1)} + \left(I^{(1)}_k + I^{(3)}_{k-1} \right) \delta_{kk'} + I^{(2)}_k\, \delta_{k(k'+1)} \right]. \quad (2.58)$$

The norm $N_{j\lambda}$ is given by (A 9). In the previous equations we have introduced the integrals of the finite element products over intervals $\mathcal{I}_k$ which can be expressed analytically,

$$I^{(1)}_k = \int_{r_k}^{r_{k+1}} \psi_k(r)\, \psi_k(r)\, r^2\, dr = \frac{h_k}{30} \left(r^2_{k+1} + 3\, r_k r_{k+1} + 6\, r^2_k \right), \quad (2.59)$$

$$I^{(2)}_k = \int_{r_k}^{r_{k+1}} \psi_k(r)\, \psi_{k+1}(r)\, r^2\, dr = \frac{h_k}{60} \left(3\, r^2_{k+1} + 4\, r_k r_{k+1} + 3\, r^2_k \right), \quad (2.60)$$

$$I^{(3)}_k = \int_{r_k}^{r_{k+1}} \psi_{k+1}(r)\, \psi_{k+1}(r)\, r^2\, dr = \frac{h_k}{30} \left(6\, r^2_{k+1} + 3\, r_k r_{k+1} + r^2_k \right). \quad (2.61)$$

These are defined for $k = 1, \ldots, P$. To keep unified notation of formula (2.58) even for the lowermost $(k, k' = 1)$ and for the uppermost $(k, k' = P)$ layers, we formally define $I^{(\cdot)}_0 = I^{(\cdot)}_{P+1} = 0$.

Before we express the approximation of the form $a_0(\cdot,\cdot)$ we define on each interval $\mathcal{I}_k$ functions

$$\chi_k(r) = r \left(\frac{d}{dr} + \frac{1}{r} \right) \psi_k(r) = \frac{r_{k+1} - 2\, r}{h_k}, \quad (2.62)$$

$$\chi_{k+1}(r) = r \left(\frac{d}{dr} + \frac{1}{r} \right) \psi_{k+1}(r) = \frac{2\, r - r_k}{h_k}. \quad (2.63)$$

Then, using (A 16–A 18), we can write the rotation of the basis functions $\psi_k \, \overline{\boldsymbol{S}}^{(\lambda)}_{jm}$ from $H^h_{\rm curl}$ as

$$
\begin{aligned}
r\,\mathrm{curl}\,\Big[\psi_k(r)\,\boldsymbol{S}^{(0)}_{jm}(\Omega)\Big] &= -\Pi_j\psi_k(r)\,\boldsymbol{S}^{(-1)}_{jm}(\Omega) - \chi_k(r)\,\boldsymbol{S}^{(1)}_{jm}(\Omega), && (2.64)\\
r\,\mathrm{curl}\,\Big[\psi_k(r)\,\boldsymbol{S}^{(-1)}_{jm}(\Omega)\Big] &= -\psi_k(r)\,\boldsymbol{S}^{(0)}_{jm}(\Omega), && (2.65)\\
r\,\mathrm{curl}\,\Big[\psi_k(r)\,\boldsymbol{S}^{(1)}_{jm}(\Omega)\Big] &= \chi_k(r)\,\boldsymbol{S}^{(0)}_{jm}(\Omega). && (2.66)
\end{aligned}
$$

Introducing the piecewise constant parameterization of the radial resistivity profile $\rho_0(r)$,

$$
\rho_0(r) = \rho_{0,k} = \text{const} \quad \text{for } r \in \mathcal{I}_k, \tag{2.67}
$$

and substituting (2.64–2.66) into the definition (2.48), yields for the form $a_0(\cdot,\cdot)$,

$$
\begin{aligned}
a_0\left(\psi_k\,\overline{\boldsymbol{S}}^{(\lambda)}_{jm}, \psi_{k'}\,\boldsymbol{S}^{(0)}_{j'm'}\right) &= \delta_{jj'}\,\delta_{mm'}\,\delta_{\lambda 0}\,\Pi_j\,\rho_{0,k'}\Big[\Big(\Pi_j K^{(2)}_k + K^{(5)}_k\Big)\,\delta_{k(k'-1)} + \\
&+ \Big(\Pi_j K^{(1)}_k + K^{(4)}_k + \Pi_j K^{(3)}_{k-1} + K^{(6)}_{k-1}\Big)\,\delta_{kk'} + \\
&+ \Big(\Pi_j\,K^{(2)}_k + K^{(5)}_k\Big)\,\delta_{k(k'+1)}\Big], && (2.68)\\
a_0\left(\psi_k\,\overline{\boldsymbol{S}}^{(\lambda)}_{jm}, \psi_{k'}\,\boldsymbol{S}^{(-1)}_{j'm'}\right) &= \delta_{jj'}\,\delta_{mm'}\Pi_j\,\rho_{0,k'}\Big[K^{(2)}_{k-1}\,\delta_{k(k'-1)}\,\delta_{\lambda\,-1} - K^{(8)}_{k-1}\,\delta_{k(k'-1)}\,\delta_{\lambda 1} + \\
&+ \Big(K^{(1)}_k + K^{(3)}_{k-1}\Big)\,\delta_{kk'}\,\delta_{\lambda\,-1} - \Big(K^{(7)}_k + K^{(10)}_{k-1}\Big)\,\delta_{kk'}\,\delta_{\lambda 1} + \\
&+ K^{(2)}_k\,\delta_{kk'}\,\delta_{\lambda\,-1} - K^{(9)}_k\,\delta_{kk'}\,\delta_{\lambda 1}\Big], && (2.69)\\
a_0\left(\psi_k\,\overline{\boldsymbol{S}}^{(\lambda)}_{jm}, \psi_{k'}\,\boldsymbol{S}^{(1)}_{j'm'}\right) &= \delta_{jj'}\,\delta_{mm'}\Pi_j\,\rho_{0,k'}\Big[-K^{(9)}_{k-1}\,\delta_{k(k'-1)}\,\delta_{\lambda\,-1} + K^{(5)}_{k-1}\,\delta_{k(k'-1)}\,\delta_{\lambda 1} - \\
&- \Big(K^{(7)}_k + K^{(10)}_{k-1}\Big)\,\delta_{kk'}\,\delta_{\lambda\,-1} + \Big(K^{(4)}_k + K^{(6)}_{k-1}\Big)\,\delta_{kk'}\,\delta_{\lambda 1} - \\
&- K^{(8)}_k\,\delta_{k(k'+1)}\,\delta_{\lambda\,-1} + K^{(5)}_k\,\delta_{k(k'+1)}\,\delta_{\lambda 1}\Big], && (2.70)
\end{aligned}
$$

where Π_j is defined in (A 10). We have introduced additional integrals over $\mathcal{I}_k$, namely,

$$
\begin{aligned}
K^{(1)}_k &= \int_{r_k}^{r_{k+1}} \psi_k(r)\,\psi_k(r)\,dr = \frac{h_k}{3}, && (2.71)\\
K^{(2)}_k &= \int_{r_k}^{r_{k+1}} \psi_k(r)\,\psi_{k+1}(r)\,dr = \frac{h_k}{6}, && (2.72)
\end{aligned}
$$

$$K_k^{(3)} = \int_{r_k}^{r_{k+1}} \psi_{k+1}(r)\,\psi_{k+1}(r)\,dr = \frac{h_k}{3}, \tag{2.73}$$

$$K_k^{(4)} = \int_{r_k}^{r_{k+1}} \chi_k(r)\,\chi_k(r)\,dr = \frac{1}{3\,h_k}\left(r_{k+1}^2 - 2\,r_{k+1}\,r_k + 4\,r_k^2\right), \tag{2.74}$$

$$K_k^{(5)} = \int_{r_k}^{r_{k+1}} \chi_k(r)\,\chi_{k+1}(r)\,dr = -\frac{1}{3\,h_k}\left(r_{k+1}^2 + r_{k+1}\,r_k + r_k^2\right), \tag{2.75}$$

$$K_k^{(6)} = \int_{r_k}^{r_{k+1}} \chi_{k+1}(r)\,\chi_{k+1}(r)\,dr = \frac{1}{3\,h_k}\left(4\,r_{k+1}^2 - 2\,r_{k+1}\,r_k + r_k^2\right), \tag{2.76}$$

$$K_k^{(7)} = \int_{r_k}^{r_{k+1}} \psi_k(r)\,\chi_k(r)\,dr = \frac{1}{6}\left(r_{k+1} - 4\,r_k\right), \tag{2.77}$$

$$K_k^{(8)} = \int_{r_k}^{r_{k+1}} \psi_{k+1}(r)\,\chi_k(r)\,dr = -\frac{1}{6}\left(r_{k+1} + 2\,r_k\right), \tag{2.78}$$

$$K_k^{(9)} = \int_{r_k}^{r_{k+1}} \psi_k(r)\,\chi_{k+1}(r)\,dr = \frac{1}{6}\left(2\,r_{k+1} + r_k\right), \tag{2.79}$$

$$K_k^{(10)} = \int_{r_k}^{r_{k+1}} \psi_{k+1}(r)\,\chi_{k+1}(r)\,dr = \frac{1}{6}\left(4\,r_{k+1} - r_k\right), \tag{2.80}$$

for $k = 1, \ldots, P$. Analogously to $I_k^{(\cdot)}$, we formally define $K_0^{(\cdot)} = K_{P+1}^{(\cdot)} = 0$.

Note that both the L_2 scalar product and the form $a_0(\cdot,\cdot)$ are decoupled in indeces j and m, and the coupling in the index k is limited to neighbouring layers. The former is not valid in the approximation of the form $a_1(\cdot,\cdot)$ (2.49), where lateral variations of ρ_1 introduce coupling in j and m. In the evaluation of $a_1(\cdot,\cdot)$ we follow generally the technique developed by Martinec (1999a) with minor modifications due to our choice of different system of vector spherical harmonics.

We prescribe the resistivity variations on an angular grid of $N_\vartheta \times N_\varphi$ nodes, and piecewise constant with respect to the radial coordinate, i.e.,

$$\rho_1(r, \vartheta_p, \varphi_q) = \rho_{1,k}^{pq} = \text{const} \quad \text{for } r \in \mathcal{I}_k, \tag{2.81}$$

where colatitudinal grid nodes $\{\vartheta_p\}_{p=1}^{N_\vartheta}$ are the roots of Legendre polynomial of degree

N_ϑ,

$$P_{N_\vartheta}(\cos\vartheta_p) = 0, \tag{2.82}$$

and longitudinal grid nodes $\{\varphi_q\}_{q=0}^{N_\varphi-1}$ are equidistant,

$$\varphi_q = \frac{2\pi q}{N_\varphi}. \tag{2.83}$$

Moreover, we require that $N_\vartheta > 3\,j_{max}/2$, $N_\varphi > 3\,j_{max}$, and N_φ is an integer power of 2 (Martinec, 1989).

Now we define the following sums on the grid (ϑ_p, φ_q), and for all radial indeces $k = 1, \ldots, P+1$,

$$Q^{(1)}_{pq,k} = \sum_{jm} \Pi_j \, {}^i\overline{B}^{(0)}_{jm,k} \, \overline{Y}_{jm}(\vartheta_p, \varphi_q), \tag{2.84}$$

$$Q^{(2)}_{pq,k} = \sum_{jm} {}^i\overline{B}^{(0)}_{jm,k} \, \frac{\partial \overline{Y}_{jm}}{\partial \vartheta}(\vartheta_p, \varphi_q), \tag{2.85}$$

$$Q^{(3)}_{pq,k} = \sum_{jm} {}^i\overline{B}^{(0)}_{jm,k} \, \frac{1}{\sin\vartheta_p} \frac{\partial \overline{Y}_{jm}}{\partial \varphi}(\vartheta_p, \varphi_q), \tag{2.86}$$

$$Q^{(4)}_{pq,k} = \sum_{jm} {}^i\overline{B}^{(-1)}_{jm,k} \, \frac{\partial \overline{Y}_{jm}}{\partial \vartheta}(\vartheta_p, \varphi_q), \tag{2.87}$$

$$Q^{(5)}_{pq,k} = \sum_{jm} {}^i\overline{B}^{(-1)}_{jm,k} \, \frac{1}{\sin\vartheta_p} \frac{\partial \overline{Y}_{jm}}{\partial \varphi}(\vartheta_p, \varphi_q), \tag{2.88}$$

$$Q^{(6)}_{pq,k} = \sum_{jm} {}^i\overline{B}^{(1)}_{jm,k} \, \frac{\partial \overline{Y}_{jm}}{\partial \vartheta}(\vartheta_p, \varphi_q), \tag{2.89}$$

$$Q^{(7)}_{pq,k} = \sum_{jm} {}^i\overline{B}^{(1)}_{jm,k} \, \frac{1}{\sin\vartheta_p} \frac{\partial \overline{Y}_{jm}}{\partial \varphi}(\vartheta_p, \varphi_q). \tag{2.90}$$

Because of the exponential function $\exp(-im\varphi_q)$ in the spherical harmonic functions $\overline{Y}_{jm}$, the summation over m for each node φ_q can be computed by the FFT algorithm (Martinec, 1989; Press et al., 1992).

The sums $Q^{(\alpha)}_{pq,k}$ are then multiplied by discretized resistivity and spherical harmonics, or their angular derivatives, and numerically integrated over the angular coordinates,

$$C^{(11)}_{jm,k} = \frac{2\pi}{N_\varphi} \Pi_j \sum_{p=1}^{N_\vartheta} \sum_{q=0}^{N_\varphi-1} w_p \, \rho^{pq}_{1,k} \, Q^{(1)}_{pq,k} \, Y_{jm}(\vartheta_p, \varphi_q), \tag{2.91}$$

$$C^{(\alpha 2)}_{jm,k} = \frac{2\pi}{N_\varphi}\sum_{p=1}^{N_\vartheta}\sum_{q=0}^{N_\varphi-1} w_p\,\rho^{pq}_{1,k}\,Q^{(\alpha)}_{pq,k}\,\frac{\partial Y_{jm}}{\partial\vartheta}(\vartheta_p,\varphi_q), \tag{2.92}$$

$$C^{(\alpha 3)}_{jm,k} = \frac{2\pi}{N_\varphi}\sum_{p=1}^{N_\vartheta}\sum_{q=0}^{N_\varphi-1} w_p\,\rho^{pq}_{1,k}\,Q^{(\alpha)}_{pq,k}\,\frac{1}{\sin\vartheta_p}\,\frac{\partial Y_{jm}}{\partial\varphi}(\vartheta_p,\varphi_q), \tag{2.93}$$

$$D^{(11)}_{jm,k} = \frac{2\pi}{N_\varphi}\Pi_j\sum_{p=1}^{N_\vartheta}\sum_{q=0}^{N_\varphi-1} w_p\,\rho^{pq}_{1,k}\,Q^{(1)}_{pq,k+1}\,Y_{jm}(\vartheta_p,\varphi_q), \tag{2.94}$$

$$D^{(\alpha 2)}_{jm,k} = \frac{2\pi}{N_\varphi}\sum_{p=1}^{N_\vartheta}\sum_{q=0}^{N_\varphi-1} w_p\,\rho^{pq}_{1,k}\,Q^{(\alpha)}_{pq,k+1}\,\frac{\partial Y_{jm}}{\partial\vartheta}(\vartheta_p,\varphi_q), \tag{2.95}$$

$$D^{(\alpha 3)}_{jm,k} = \frac{2\pi}{N_\varphi}\sum_{p=1}^{N_\vartheta}\sum_{q=0}^{N_\varphi-1} w_p\,\rho^{pq}_{1,k}\,Q^{(\alpha)}_{pq,k+1}\,\frac{1}{\sin\vartheta_p}\,\frac{\partial Y_{jm}}{\partial\varphi}(\vartheta_p,\varphi_q), \tag{2.96}$$

for all $j = 1,\ldots,j_{max}$, $m = 0,\ldots,j$, and $k = 1,\ldots,P$. Index α ranges from 2 to 7. In the previous equations we employed the Gauss-Legendre formula with weights w_p (Press et al., 1992) for numerical integration over ϑ,

$$\int_0^\pi f(\vartheta)\,\sin\vartheta\,d\vartheta \approx \sum_{p=1}^{N_\vartheta} w_p\,f(\vartheta_p), \tag{2.97}$$

and the discrete FFT over φ,

$$\int_0^{2\pi} f(\varphi)\,e^{im\varphi}\,d\varphi \approx \frac{2\pi}{N_\varphi}\sum_{q=1}^{N_\varphi-1} f(\varphi_q)\,e^{im\varphi_q}. \tag{2.98}$$

The spherical harmonic-finite element approximation of the form $a_1(\cdot,\cdot)$ then can be evaluated for each basis function from $H^h_{\mathrm{curl},0}$ by combining the angular integrals (2.91–2.96) with the radial integrals (2.71–2.80), and taking into account the rotation formulae (2.64–2.66),

$$\begin{aligned} a_1({}^i\boldsymbol{B},\psi_k\,\boldsymbol{S}^{(0)}_{jm}) &= \left[C^{(11)}_{jm,k-1}\,K^{(2)}_{k-1} + D^{(11)}_{jm,k-1}\,K^{(3)}_{k-1} + C^{(11)}_{jm,k}\,K^{(1)}_{k} + D^{(11)}_{jm,k}\,K^{(2)}_{k}\right] + \\ &+ \left[C^{(22)}_{jm,k-1}\,K^{(5)}_{k-1} + D^{(22)}_{jm,k-1}\,K^{(6)}_{k-1} + C^{(22)}_{jm,k}\,K^{(4)}_{k} + D^{(22)}_{jm,k}\,K^{(5)}_{k}\right] + \\ &+ \left[C^{(33)}_{jm,k-1}\,K^{(5)}_{k-1} + D^{(33)}_{jm,k-1}\,K^{(6)}_{k-1} + C^{(33)}_{jm,k}\,K^{(4)}_{k} + D^{(33)}_{jm,k}\,K^{(5)}_{k}\right] + \\ &+ \left[C^{(43)}_{jm,k-1}\,K^{(9)}_{k-1} + D^{(43)}_{jm,k-1}\,K^{(10)}_{k-1} + C^{(43)}_{jm,k}\,K^{(7)}_{k} + D^{(43)}_{jm,k}\,K^{(8)}_{k}\right] - \end{aligned}$$

$$
\begin{aligned}
&- \left[C^{(52)}_{jm,k-1}\,K^{(9)}_{k-1} + D^{(52)}_{jm,k-1}\,K^{(10)}_{k-1} + C^{(52)}_{jm,k}\,K^{(7)}_{k} + D^{(52)}_{jm,k}\,K^{(8)}_{k}\right] - \\
&- \left[C^{(63)}_{jm,k-1}\,K^{(5)}_{k-1} + D^{(63)}_{jm,k-1}\,K^{(6)}_{k-1} + C^{(63)}_{jm,k}\,K^{(4)}_{k} + D^{(63)}_{jm,k}\,K^{(5)}_{k}\right] + \\
&+ \left[C^{(72)}_{jm,k-1}\,K^{(5)}_{k-1} + D^{(72)}_{jm,k-1}\,K^{(6)}_{k-1} + C^{(72)}_{jm,k}\,K^{(4)}_{k} + D^{(72)}_{jm,k}\,K^{(5)}_{k}\right], \qquad (2.99)
\end{aligned}
$$

$$
\begin{aligned}
a_1({}^i\boldsymbol{B}, \psi_k\,\boldsymbol{S}^{(-1)}_{jm}) \;=\; &\left[C^{(32)}_{jm,k-1}\,K^{(8)}_{k-1} + D^{(32)}_{jm,k-1}\,K^{(10)}_{k-1} + C^{(32)}_{jm,k}\,K^{(7)}_{k} + D^{(32)}_{jm,k}\,K^{(9)}_{k}\right] - \\
&- \left[C^{(23)}_{jm,k-1}\,K^{(8)}_{k-1} + D^{(23)}_{jm,k-1}\,K^{(10)}_{k-1} + C^{(23)}_{jm,k}\,K^{(7)}_{k} + D^{(23)}_{jm,k}\,K^{(9)}_{k}\right] + \\
&+ \left[C^{(42)}_{jm,k-1}\,K^{(2)}_{k-1} + D^{(42)}_{jm,k-1}\,K^{(3)}_{k-1} + C^{(42)}_{jm,k}\,K^{(1)}_{k} + D^{(42)}_{jm,k}\,K^{(2)}_{k}\right] + \\
&+ \left[C^{(53)}_{jm,k-1}\,K^{(2)}_{k-1} + D^{(53)}_{jm,k-1}\,K^{(3)}_{k-1} + C^{(53)}_{jm,k}\,K^{(1)}_{k} + D^{(53)}_{jm,k}\,K^{(2)}_{k}\right] - \\
&- \left[C^{(62)}_{jm,k-1}\,K^{(8)}_{k-1} + D^{(62)}_{jm,k-1}\,K^{(10)}_{k-1} + C^{(62)}_{jm,k}\,K^{(7)}_{k} + D^{(62)}_{jm,k}\,K^{(9)}_{k}\right] - \\
&- \left[C^{(73)}_{jm,k-1}\,K^{(8)}_{k-1} + D^{(73)}_{jm,k-1}\,K^{(10)}_{k-1} + C^{(73)}_{jm,k}\,K^{(7)}_{k} + D^{(73)}_{jm,k}\,K^{(9)}_{k}\right], \qquad (2.100)
\end{aligned}
$$

$$
\begin{aligned}
a_1({}^i\boldsymbol{B}, \psi_k\,\boldsymbol{S}^{(1)}_{jm}) \;=\; &\left[C^{(23)}_{jm,k-1}\,K^{(5)}_{k-1} + D^{(23)}_{jm,k-1}\,K^{(6)}_{k-1} + C^{(23)}_{jm,k}\,K^{(4)}_{k} + D^{(23)}_{jm,k}\,K^{(5)}_{k}\right] - \\
&- \left[C^{(32)}_{jm,k-1}\,K^{(5)}_{k-1} + D^{(32)}_{jm,k-1}\,K^{(6)}_{k-1} + C^{(32)}_{jm,k}\,K^{(4)}_{k} + D^{(32)}_{jm,k}\,K^{(5)}_{k}\right] - \\
&- \left[C^{(42)}_{jm,k-1}\,K^{(9)}_{k-1} + D^{(42)}_{jm,k-1}\,K^{(10)}_{k-1} + C^{(42)}_{jm,k}\,K^{(7)}_{k} + D^{(42)}_{jm,k}\,K^{(8)}_{k}\right] - \\
&- \left[C^{(53)}_{jm,k-1}\,K^{(9)}_{k-1} + D^{(53)}_{jm,k-1}\,K^{(10)}_{k-1} + C^{(53)}_{jm,k}\,K^{(7)}_{k} + D^{(53)}_{jm,k}\,K^{(8)}_{k}\right] + \\
&+ \left[C^{(62)}_{jm,k-1}\,K^{(5)}_{k-1} + D^{(62)}_{jm,k-1}\,K^{(6)}_{k-1} + C^{(62)}_{jm,k}\,K^{(4)}_{k} + D^{(62)}_{jm,k}\,K^{(5)}_{k}\right] + \\
&+ \left[C^{(73)}_{jm,k-1}\,K^{(5)}_{k-1} + D^{(73)}_{jm,k-1}\,K^{(6)}_{k-1} + C^{(73)}_{jm,k}\,K^{(4)}_{k} + D^{(73)}_{jm,k}\,K^{(5)}_{k}\right]. \qquad (2.101)
\end{aligned}
$$

Let us order the unknown coefficients ${}^{i+1}\overline{B}^{(\lambda)}_{jm,k}$ of the magnetic field at the $(i+1)$-th time step into a complex column vector

$$
\boldsymbol{x}^T = \left\{ \left[\left({}^{i+1}\overline{B}^{(0)}_{jm,k}, {}^{i+1}\overline{B}^{(-1)}_{jm,k}, {}^{i+1}\overline{B}^{(1)}_{jm,k} \right)_{k=1}^{P+1} \right]_{m=0}^{j} \right\}_{j=1}^{j_{max}}, \qquad (2.102)
$$

with dimension $d = 3(P+1)j_{max}(j_{max}+3)/2$. The complex coefficients for negative m are not included in vector $\boldsymbol{x}$, but, when needed in the evaluation of $a_1(\cdot,\cdot)$, they are computed using the symmetry (2.56). Now we construct the Galerkin system of d linear complex equations which represents a discrete approximation of (2.51–2.53),

$$
\mathcal{A} \cdot \boldsymbol{x} = \boldsymbol{y}. \qquad (2.103)
$$

The elements of matrix $\mathcal{A}$ and the right-hand side vector $\boldsymbol{y}$ are defined as

$$a_{n'n} = \frac{\mu_0}{\Delta t}\left(\psi_k\,\overline{\boldsymbol{S}}^{(\lambda)}_{jm}, \psi_{k'}\,\boldsymbol{S}^{(\lambda')}_{j'm'}\right) + a_0\left(\psi_k\,\overline{\boldsymbol{S}}^{(\lambda)}_{jm}, \psi_{k'}\,\boldsymbol{S}^{(\lambda')}_{j'm'}\right), \tag{2.104}$$

$$y_{n'} = \frac{\mu_0}{\Delta t}\sum_{j=1}^{j_{max}}\sum_{m=-j}^{j}\sum_{k=1}^{P+1}\sum_{\lambda=-1}^{1} {}^{i}\overline{B}^{(\lambda)}_{jm,k}\left(\psi_k\,\overline{\boldsymbol{S}}^{(\lambda)}_{jm}, \psi_{k'}\,\boldsymbol{S}^{(\lambda')}_{j'm'}\right) - a_1\left({}^{i}\boldsymbol{B}, \psi_{k'}\,\boldsymbol{S}^{(\lambda')}_{j'm'}\right), \tag{2.105}$$

where the multi-indeces n and n' are considered from intervals

$$n = \{j, m, k, \lambda\} = \{\{1, \ldots, j_{max}\}, \{0, \ldots, j\}, \{1, \ldots, P+1\}, \{0, -1, 1\}\}, \tag{2.106}$$

$$n' = \{j', m', k', \lambda'\} = \{\{1, \ldots, j_{max}\}, \{0, \ldots, j'\}, \{1, \ldots, P+\delta_{\lambda'-1}\}, \{0, -1, 1\}\}. \tag{2.107}$$

Because the test functions $\psi_{P+1}\,\overline{\boldsymbol{S}}^{(0)}_{jm}$ and $\psi_{P+1}\,\overline{\boldsymbol{S}}^{(1)}_{jm}$ were excluded from $H^h_{\mathrm{curl},0}$, there are two missing equations for each $j'm'$ in equations (2.104–2.107). Hence, the system must be completed by the boundary conditions (2.24–2.25). The constraint on the toroidal field on the surface ∂G is imposed by prescribing

$$a_{n'n} = \delta_{jj'}\delta_{mm'}\delta_{k(P+1)}\delta_{\lambda 0}, \quad y_{n'} = 0, \tag{2.108}$$

for $n' = \{\{1, \ldots, j_{max}\}, \{0, \ldots, j'\}, P+1, 0\}$. The load by external magnetic potential is implemented by setting

$$a_{n'n} = \delta_{jj'}\delta_{mm'}\delta_{k(P+1)}\left[(\delta_{\lambda-1} + (j+1)\delta_{\lambda 1}\right], \quad y_{n'} = -(2j'+1)\,\overline{G}^{(e)}_{j'm'}(t_{i+1}), \tag{2.109}$$

for $n' = \{\{1, \ldots, j_{max}\}, \{0, \ldots, j'\}, P+1, 1\}$.

Matrix $\mathcal{A}$ is a complex 9-banded matrix which depends only on the length of the time step Δt and on the radial resistivity structure ρ_0. Since the linear system (2.103) is repeatedly solved in each time step, it is effective to use the LU-decomposition of $\mathcal{A}$. Using a subroutine provided by LAPACK (Anderson et al., 1999), for $j_{max} = 40$ and $P = 100$, it takes only about 10 s on a 500 MHz PC to decompose $\mathcal{A}$. Evaluation of the right-hand side $\boldsymbol{y}$ is based on (2.84–2.96) and (2.99–2.101), and uses the solution ${}^{i}\boldsymbol{B}$ from the previous time step. It is the most time-consuming part of the algorithm, and takes about 20 s for each time step at given spatial resolution.

2.2 Validation

2.2.1 Nested-sphere conductivity models

In this section we validate the presented time-domain spectral-finite element approach using the conductivity models consisting of a homogeneous sphere with a nested spherical inclusion of different conductivity. The configuration of the nested-sphere conductivity

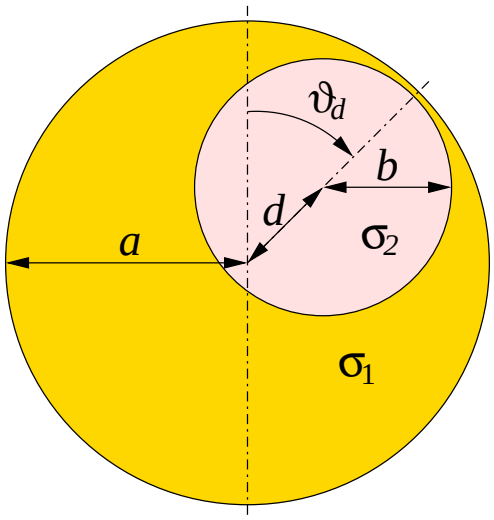

Figure 2.3: Nested-sphere conductivity model (cross-section). A homogeneous sphere with radius b and conductivity σ_2 is nested in the host sphere with radius a and conductivity σ_1. The centre of the inclusion is positioned at a distance d from the centre of the host sphere at colatitude ϑ_d and longitude φ_d.

model is shown in Figure 2.3. This class of models with a frequency-domain, semi-analytical solution developed by Everett & Schultz (1995) for axially symmetric models, and generalized by Martinec (1998) to treat an off-axis spherical inclusion, has become a standard tool for validation of 3-D EM forward solvers (Everett & Schultz, 1996; Martinec, 1999a; Uyeshima & Schultz, 2000).

In each homogeneous sphere the equation of EM induction reduces to a complex vector Helmholtz equation, $(\nabla^2 + k_n^2)\boldsymbol{B}_{SA} = 0$, where $k_n^2 = -i\omega\mu_0\sigma_n$, and the subscript SA stands for semi-analytical. The magnetic induction vector $\boldsymbol{B}_{SA}$ is expanded into truncated series of eigenfunctions of the Helmholtz operator. The coefficients of the expansion in both spheres are determined from the boundary conditions on the interface by solving a system of linear equations.

Although theoretically this method should provide results of almost analytical accuracy, caution must be paid when using a high-degree spherical harmonic expansion for high frequencies ω, where the method often breaks down numerically. However, this numerical instability has a physical background. As the frequency ω increases, the penetration depth of the damped EM wave decreases, and the solution becomes less sensitive to the position, size, and conductivity of the inclusion. For $\omega \to \infty$ the response of the nested spheres model converges to the response of a homogeneous sphere. In the case of dipolar excitation the response of a homogeneous sphere can be expressed by dipolar terms only. Therefore, the truncation degree j_{max} for a particular frequency band is cho-

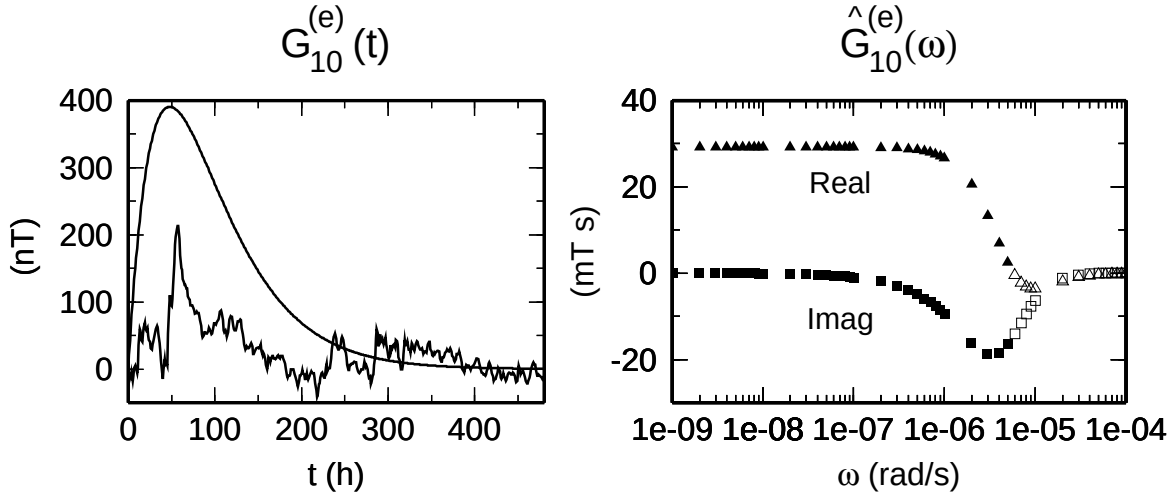

Figure 2.4: Analytical model of the geomagnetic storm defined by (2.111) is shown in the left panel. The $G_{10}^{(e)}$ coefficient derived from the Dst index during a real storm in February 1980 is plotted only for comparison. The Fourier spectrum of the analytical model is shown on the right panel with sampling that is used in the semi-analytical method. Solid and open symbols correspond to truncation degree of 18 and 12, respectively.

sen according to two criteria. Firstly, j_{max} is small enough to yield a stable solution, i.e., the power of magnetic field is a decreasing function of spherical harmonic degree j. Secondly, j_{max} is large enough to parameterize the model sufficiently, i.e., introducing small variations of j_{max} in both directions has no significant impact on the obtained solution.

We use two following models in the validation. In Model A, the host sphere with radius $a = 6371\,\mathrm{km}$ has conductivity $\sigma_1 = 1\,\mathrm{S/m}$. The centre of the spherical inclusion with radius $b = 3500\,\mathrm{km}$ and conductivity $\sigma_2 = 10\,\mathrm{S/m}$ is positioned at a distance $d = 2700\,\mathrm{km}$ from the centre of the host sphere at colatitude $\vartheta_d = 40°$ and longitude $\varphi_d = 35°$. The Model B is characterized by the same parameters, except for the conductivity of the host sphere which is set to $\sigma_1 = 0.1\,\mathrm{S/m}$, thus increasing the conductivity contrast in the model by two orders of magnitude.

2.2.2 Excitation

The presented method allows the excitation by an arbitrary spatio-temporal configuration of the external inducing field. In the following examples we excite the conductivity models by two different signals.

In order to compare the results in the frequency-domain we use a harmonic signal

(Load 1) with simple dipolar spatial structure,

$$G^{(e)}_{jm}(t) = \begin{cases} A\sqrt{\frac{4\pi}{3}}\,\sin(\omega t) & \text{for } j=1,\ m=0, \\ 0 & \text{otherwise,} \end{cases} \tag{2.110}$$

where $A = 100\,\mathrm{nT}$ is the amplitude, $\sqrt{4\pi/3}$ is the inverse norm of $P_{10}(\cos\vartheta)$, and $\omega = 3\times10^{-7}\,\mathrm{rad/s}$ is the angular frequency (period $T = 242\,\mathrm{d}$). It corresponds to a ring current with periodically varying intensity.

The second model (Load 2) of the excitation source used for validation of the time-domain approach is an analytical approximation of the complicated spatio-temporal structure of a geomagnetic storm (Daglis & Kozyra, 2002). We define a time-varying dipolar coefficient of the external magnetic potential as

$$G^{(e)}_{jm}(t) = \begin{cases} A\sqrt{\frac{4\pi}{3}}\,t\,e^{-\alpha t} & \text{for } j=1,\ m=0, \\ 0 & \text{otherwise,} \end{cases} \tag{2.111}$$

where $A = 0.003\,\mathrm{nT/s}$ is the amplitude, and $1/\alpha = 48\,\mathrm{h}$ is relaxation time of the storm. Regardless of its simplicity, this mathematical model characterizes two basic features of magnetic storms, the P_{10} spatial configuration, and the time evolution with relatively fast onset and slow relaxation (see Figure 2.4). The Fourier spectrum of signal (2.111) has analytical form,

$$\hat{G}^{(e)}_{10}(\omega) = \sqrt{\frac{4\pi}{3}}\,\frac{A}{2\,\pi}\,\frac{\alpha^2-\omega^2-2i\alpha\omega}{\left(\alpha^2+\omega^2\right)^2}. \tag{2.112}$$

2.2.3 Results

In the first example we validate the time-domain, spectral-finite element approach against the semi-analytical solution $\boldsymbol{B}_{SA}$ in the frequency-domain. The nested-sphere Model A is excited by the harmonic Load 1 with period $T = 242\,\mathrm{d}$. The same configuration was used also by Everett & Schultz (1996) and Martinec (1999a). The long period assures that the EM energy penetrates down to the centre of the sphere, allowing to test the 3-D methods throughout the model. The semi-analytical solution $\boldsymbol{B}_{SA}$ is truncated at $j_{max} = 18$.

The time-domain solution is started from zero initial condition and evolves for 4 periods, i.e. 968 days. The results are transformed to the frequency-domain using Fourier integration from T to $4T$. In order to avoid the bias from the transient switch-on effect, we exclude the data for $t < T$.

Figure 2.5 shows the convergence of the time integrated solution to the semi-analytical one as the spatial and temporal resolution increases. The response of the nested-sphere model to a slowly varying, long periodic signal is modelled with sufficient accuracy even by the runs with low spatial and temporal resolution. The B_φ component shows the

highest sensitivity to the spatial parameterization. The time-integration is stable even for 24 h time step, however, the differences from the semi-analytical solution in all three components of $\boldsymbol{B}$ increase with Δt.

In Figure 2.6 we display the time-evolution of the errors with respect to the reference solution $\boldsymbol{B}_{SA}$ as observed on the surface. For the high-resolution model, the initial 100% relative error due to the zero initial state is reduced below 2% after $t = T$, and goes well below 1% about $t = 2T$ after the onset of the time integration. Then the relative error slowly increases, as the numerical errors accumulate. The oscillation of the error is caused by the periodical change of $\boldsymbol{B}_{SA}$, the local maxima of the error curve correspond to the local minima of the reference harmonic solution.

Figure 2.7 shows that applying an additional divergence-free constraint is not necessary in the presented formulation. The deviation of the solution from the solenoidal state introduced by numerical errors increases for runs with high lateral resolution ($j_{max} = 40$), decreases for runs with high radial resolution ($P = 100$), and is insensitive to the length of time step. Nevertheless, it is negligible for all presented runs.

In the case of a high-contrast Model B excited by a simulated geomagnetic storm (Load 2), the reference semi-analytical solution is found for discretely sampled frequencies in the range 10^{-9}–10^{-4} rad/s (see Figure 2.4). The spherical harmonic expansion is truncated at $j_{max} = 18$ for frequencies below 5×10^{-6} rad/s, and at $j_{max} = 12$ for higher frequencies. The time-evolution of $\boldsymbol{B}_{SA}$ is computed by numerical evaluation of Fourier integrals of the frequency-domain solution.

Figures 2.8 and 2.9 compare the reference solution with the results of the time-domain, spectral-finite element method. Results obtained by integration with long time steps show considerable delay behind the reference solution. This is a consequence of the explicit treating of the effect of lateral conductivity variations. Although the nested spheres Model B has the same geometry as previous Model A, increased conductivity contrast transfers more energy into the higher degree terms of the spherical harmonic series, and good accuracy is obtained only for the highest truncation degree.

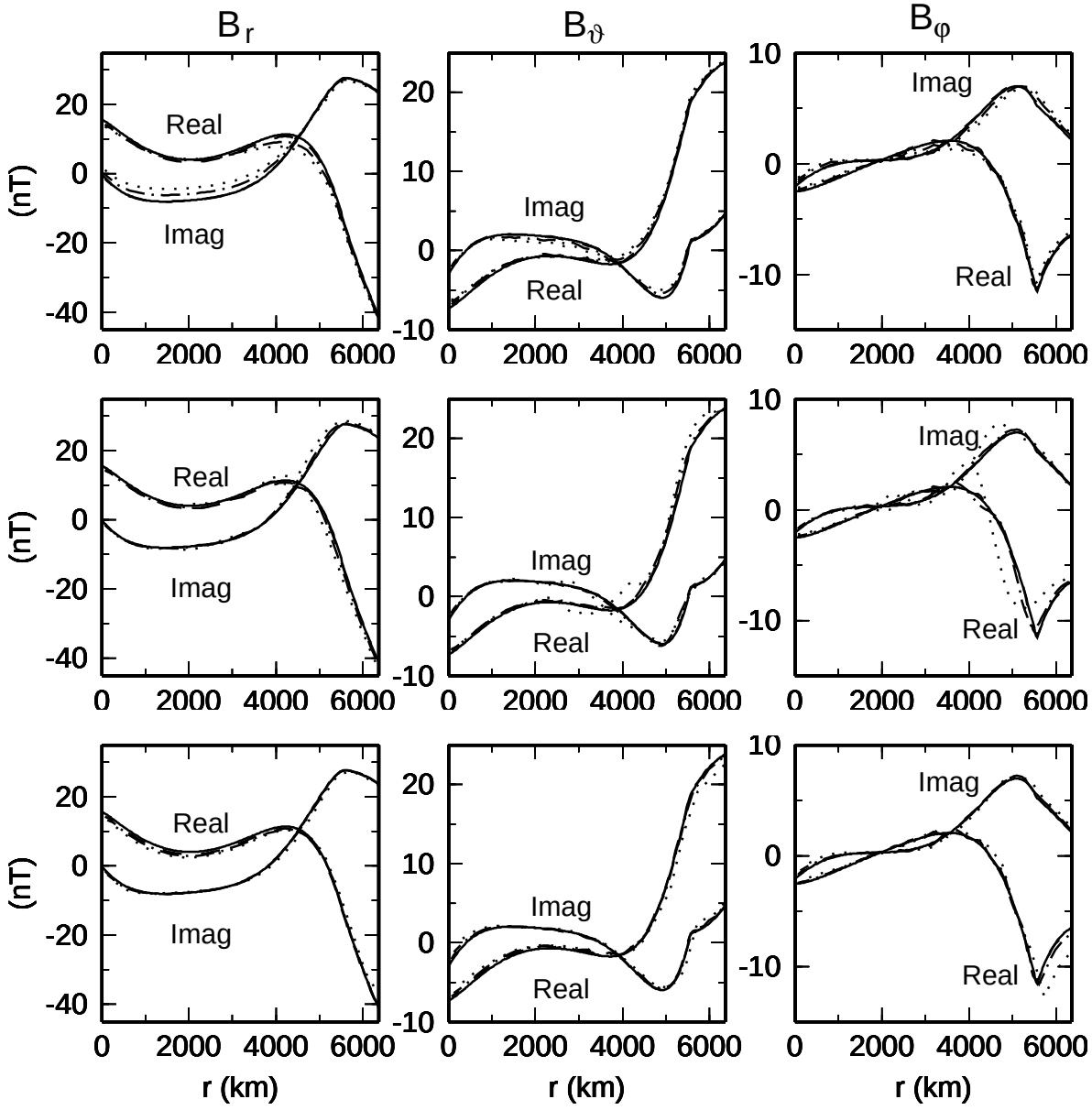

Figure 2.5: Resolution-dependent convergence of the time-domain method towards the semi-analytical solution for the conductivity Model A excited by Load 1. The components of $\boldsymbol{B}$ are plotted along radius at fixed colatitude $\vartheta = 13°$ and longitude $\varphi = 0°$. The semi-analytical solution is shown by solid line in all plates. Top row: $j_{max} = 40$, $P = 100$, dotted, dash-dotted, and dashed lines correspond to time steps $\Delta t = 24$, 12, and 1 h, respectively. Middle row: $P = 100$, $\Delta t = 1$ h, dotted, dash-dotted, and dashed lines correspond to truncation degrees $j_{max} = 10$, 20, and 40, respectively. Bottom row: $j_{max} = 40$, $\Delta t = 1$ h, dotted, dash-dotted, and dashed lines correspond to $P = 20$, 50, and 100 finite elements, respectively.

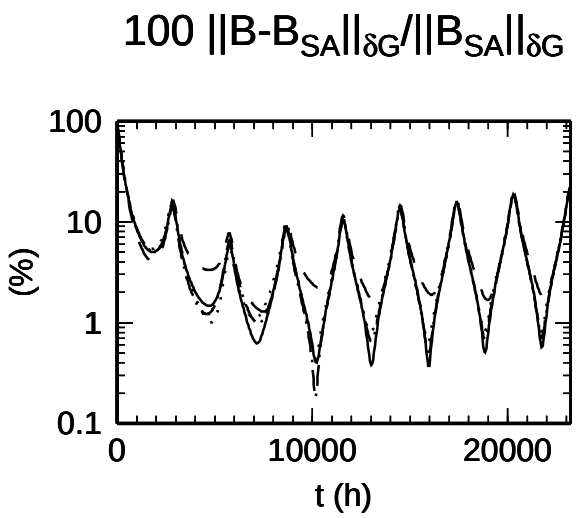

Figure 2.6: Relative error of the time-domain solution with respect to the semi-analytical one. The ratio of norms $||\boldsymbol{B}(t) - \boldsymbol{B}_{SA}(t)||_{L_2(\partial G)}/||\boldsymbol{B}_{SA}(t)||_{L_2(\partial G)}$ uses only the values of $\boldsymbol{B}$ observable at the surface ∂G. The solid, dashed, dash-dotted, and dotted lines correspond to solutions shown in Figure 2.5 with discretization parameters (j_{max}, P, Δt) set to (40, 100, 1 h), (40, 20, 1 h), (40, 100, 24 h), and (10, 100, 1 h), respectively.

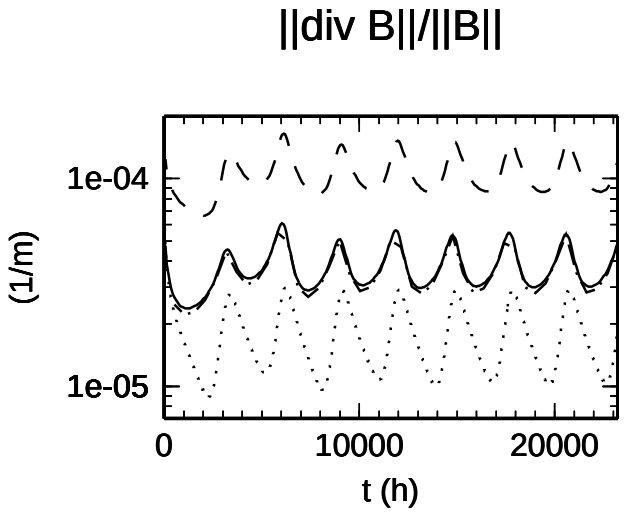

Figure 2.7: Deviation from the divergence-free condition introduced by numerical errors during the time integration measured by the ratio of norms $||\text{div}\,\boldsymbol{B}(t)||_{L_2}/||\boldsymbol{B}(t)||_{L_2}$. Same line styles as in Figure 2.6 are used.

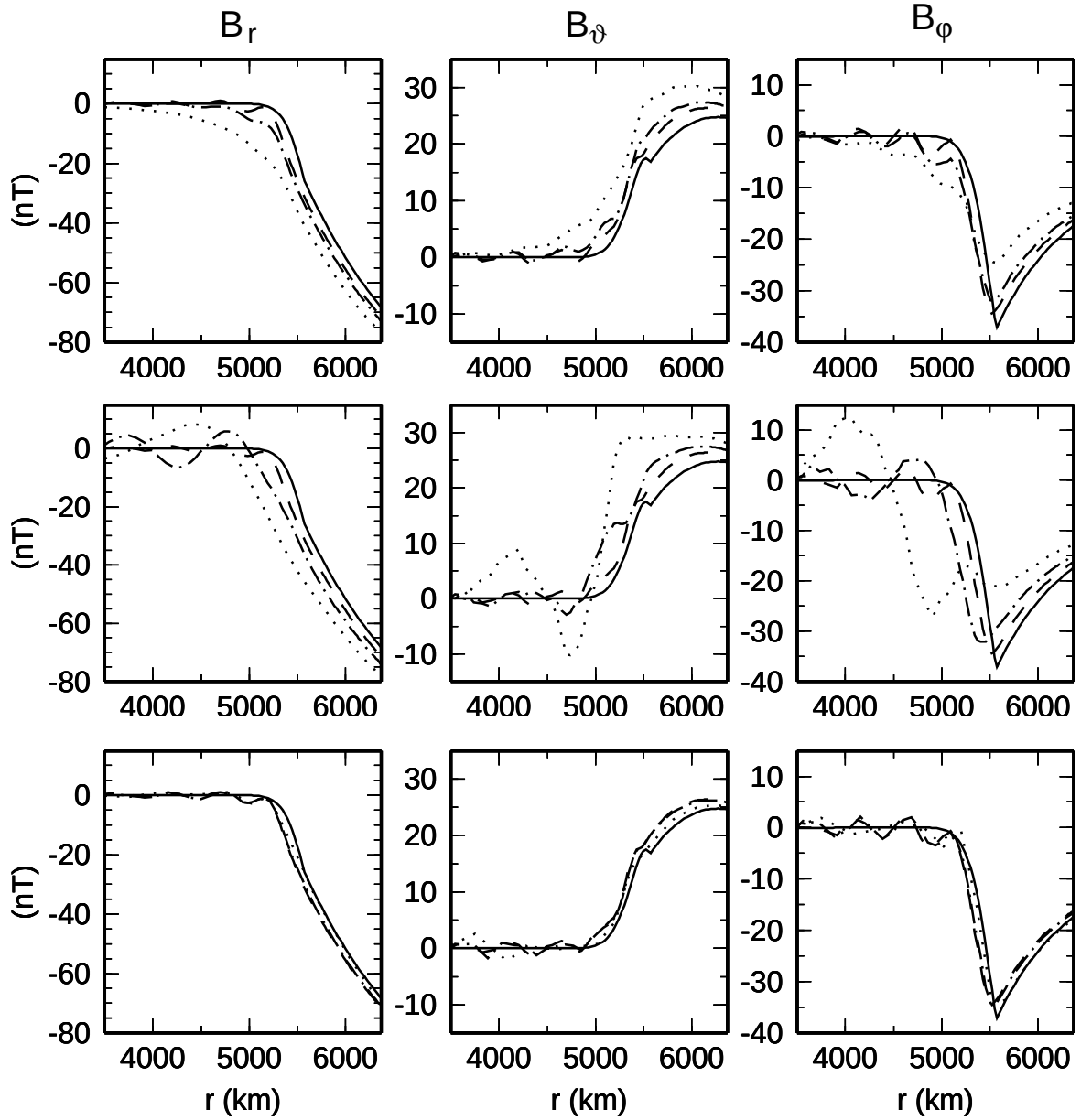

Figure 2.8: Resolution-dependent convergence of the time-domain method towards the semi-analytical solution for the conductivity Model B excited by Load 2. The components of $\boldsymbol{B}$ are plotted at $t = 96\,\mathrm{h}$. Colatitude and longitude are fixed at $\vartheta = 13^\circ$ and $\varphi = 0^\circ$. The semi-analytical solution is shown by solid line in all plates. Top row: $j_{max} = 40$, $P = 100$, dotted, dash-dotted, and dashed lines correspond to time steps $\Delta t = 4$, 1, and 0.25 h, respectively. Middle row: $P = 100$, $\Delta t = 0.25\,\mathrm{h}$, dotted, dash-dotted, and dashed lines correspond to truncation degrees $j_{max} = 10$, 20, and 40, respectively. Bottom row: $j_{max} = 40$, $\Delta t = 0.25\,\mathrm{h}$, dotted, dash-dotted, and dashed lines correspond to $P = 20$, 50, and 100 finite elements, respectively.

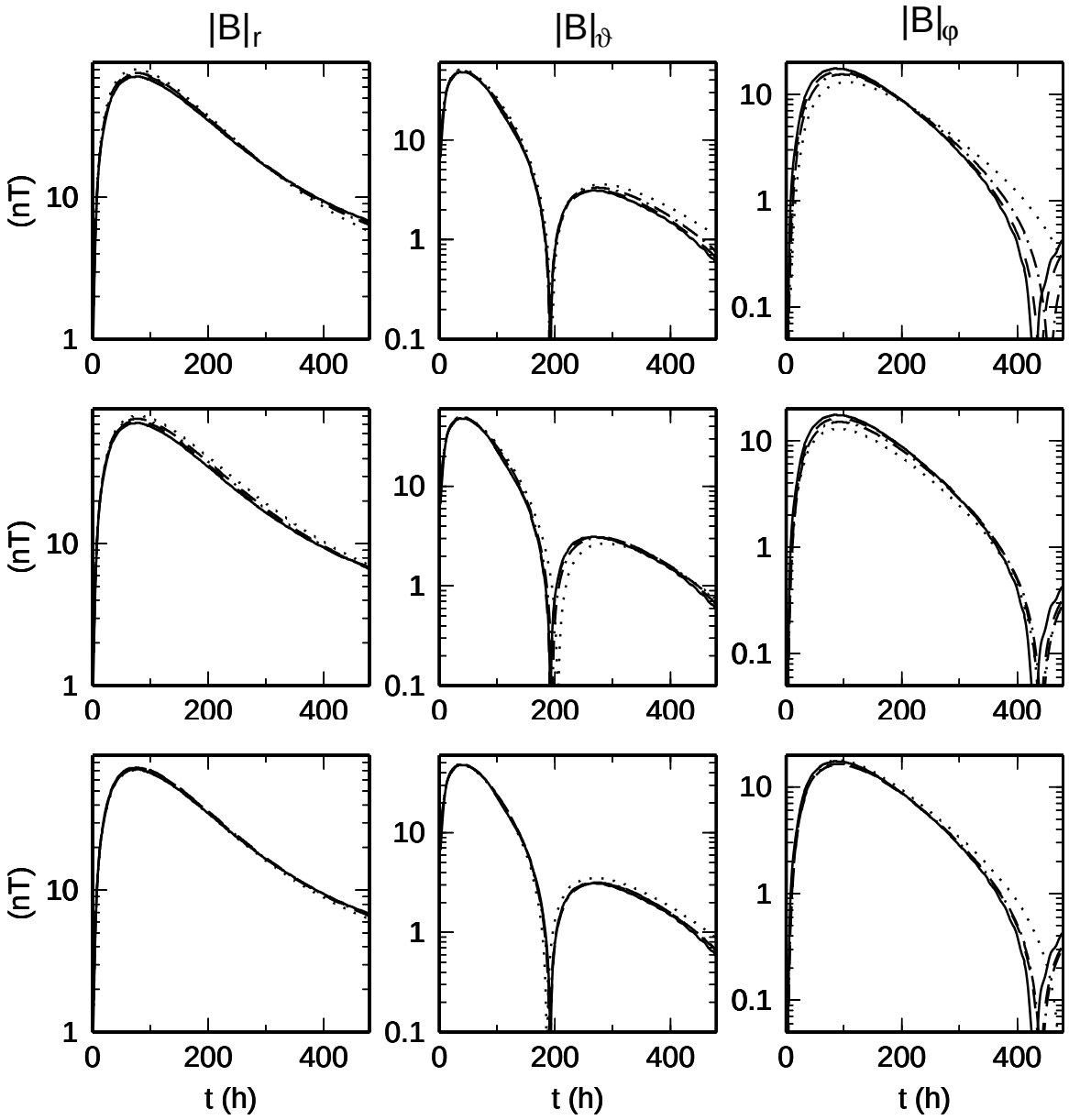

Figure 2.9: The same results as in Figure 2.8. The time evolution of the magnetic induction vector is plotted at fixed colatitude $\vartheta = 13^\circ$ and longitude $\varphi = 0^\circ$, on the surface of the sphere.

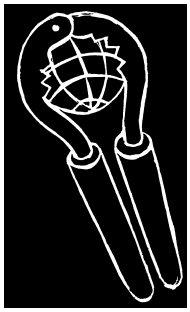

Chapter 3

Time-domain, 3-D finite element approach

3.1 $\boldsymbol{A} - \Phi, U$ formulation

3.1.1 Classical formulation

We have shown in Chapter 2 that the Galerkin formulation of the EM induction problem in terms of magnetic induction vector $\boldsymbol{B}$ is based on a discrete approximation of the functional space H_{curl}. Although mixed 3-D finite elements conforming to H_{curl} can be constructed (Nédelec, 1980), it is often advantageous to reformulate the EM induction problems using the scalar and vector electromagnetic potentials which can be parameterized by simple nodal finite element functions (Biro & Preis, 1989). Such a technique has already been successfully applied to the electromagnetic induction problem in the Earth's mantle in the frequency domain (Everett & Schultz, 1996). Here we aim to reformulate it in the time-domain both in the classical and integral sense, and to validate an associated numerical code.

The solution domain used in the 3-D finite element method differs from that used in the spectral-finite element approach. Firstly, we reduce the computational requirements by assuming an infinitely conductive core, removing it from the solution domain and replacing it by boundary conditions applied on the core-mantle boundary (CMB). Hence, we approximate the Earth's mantle by a spherical shell G with the inner boundary ∂G_1 at $r = a_{CMB}$ and the outer boundary ∂G_2 at $r = a$, filled with conductive material of spatially varying conductivity $\sigma(\boldsymbol{r})$.

Note that it is possible to reformulate the spectral-finite element method from Chapter 2 with an infinitely conductive core. However, since the usual choice of homogeneous, highly conductive core introduces no coupling in the spherical harmonic parameterization, the resulting reduction of the computational burden would be negligible. On the other hand, the 3-D finite element method introduced in this Chapter could incorporate a finitely conductive core, but at the cost of significant increase of computational and memory requirements, since the method does not take advantages of spherically symmetric conductivity. Both the finitely and infinitely conductive core approaches are suitable for the realistic configuration of the EM induction problem in the Earth's mantle.

Secondly, since the Laplace equation in the surrounding insulating spherical shell A is solved numerically, not analytically, as in the spectral-finite element method, we define explicitly both surfaces of the outer spherical shell A: the inner boundary $\partial A_1 \equiv \partial G_2$ of

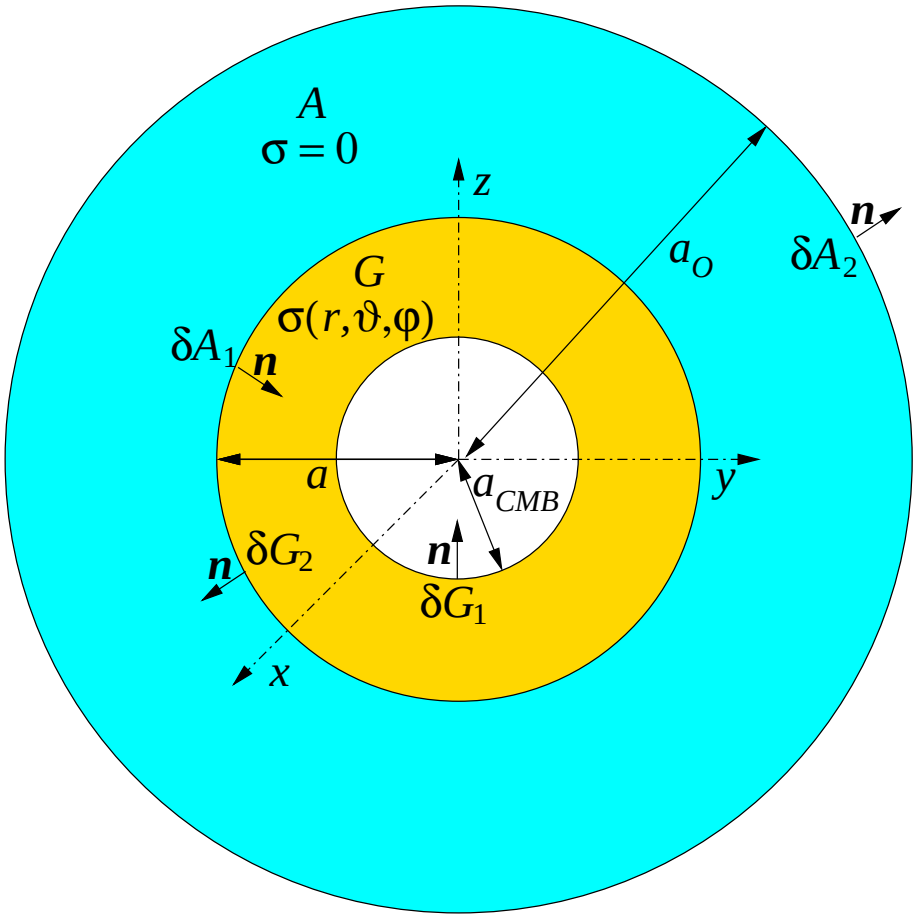

Figure 3.1: A schematic figure of model configuration. Heterogeneous conductive spherical shell G with inner surface ∂G_1 of radius a_{CMB} and outer surface ∂G_2 of radius a is surrounded by an insulating spherical layer A with inner surface $\partial A_1 \equiv \partial G_2$ and outer surface ∂A_2 of radius a_O. Note the orientation of outer normals on the surfaces.

radius $r = a$ and the outer boundary ∂A_2 of radius $r = a_O$. Note that the outer unit normal vector $\boldsymbol{n}$ is pointing to and from the Earth's centre on $\partial G_1 \cup \partial A_1$ and $\partial G_2 \cup \partial A_2$, respectively.

As can be seen from the analytical formulae (2.14–2.15), the primary inducing field grows as r^{j-1} in A, while the secondary induced field decays as r^{-j-2}, where j is the spherical harmonic degree. The outer surface ∂A_2 is placed at such a distance a_O that the field induced by the eddy currents in the conductive mantle is negligible, and only the inducing field due to external current systems can be considered in the boundary condition. A choice of a_O between $4\,a$ and $10\,a$ (Everett & Schultz, 1996; Uyeshima & Schultz, 2000) yields a decrease in the internal to external field ratio by 2–3 orders of

magnitude through the layer A.

The vectors of electric intensity and magnetic induction, $\boldsymbol{E}$ and $\boldsymbol{B}$, in conductors and insulators can be represented by various combinations of scalar and vector potentials. Following Biro & Preis (1989), we use the approach known as $\boldsymbol{A} - \Phi, U$ method. In this approach, the vector magnetic potential $\boldsymbol{A}$ and the scalar electrical potential ϕ are used in a conductive material in the forms

$$\boldsymbol{B}(\boldsymbol{r}; t) = -\operatorname{curl} \boldsymbol{A}(\boldsymbol{r}; t) \quad \text{in } G, \tag{3.1}$$

$$\boldsymbol{E}(\boldsymbol{r}; t) = -\frac{\partial \boldsymbol{A}}{\partial t}(\boldsymbol{r}; t) - \operatorname{grad} \phi(\boldsymbol{r}; t) \quad \text{in } G. \tag{3.2}$$

In the time-domain approach it is useful to replace the scalar electrical potential ϕ by its time integral Φ,

$$\phi(\boldsymbol{r}; t) = \frac{\partial}{\partial t} \Phi(\boldsymbol{r}; t) \quad \text{in } G, \tag{3.3}$$

since it leads to a symmetric Galerkin matrix. The solenoidal and irrotational magnetic induction $\boldsymbol{B}$ in the insulator is expressed as a gradient of scalar magnetic potential U,

$$\boldsymbol{B}(\boldsymbol{r}; t) = -\operatorname{grad} U(\boldsymbol{r}; t) \quad \text{in } A. \tag{3.4}$$

Substitution of (3.1–3.3) and of the Ohm law,

$$\boldsymbol{j} = \sigma \boldsymbol{E}, \tag{3.5}$$

into the quasi static form of the Ampère law,

$$\operatorname{curl} \left(\frac{1}{\mu_0} \boldsymbol{B} \right) = \boldsymbol{j} \quad \text{in } G, \tag{3.6}$$

yields

$$\operatorname{curl} \left(\frac{1}{\mu_0} \operatorname{curl} \boldsymbol{A} \right) + \sigma \frac{\partial}{\partial t} \left(\boldsymbol{A} + \operatorname{grad} \Phi \right) = 0 \quad \text{in } G. \tag{3.7}$$

Note that equation (3.7) implicitly satisfies the quasi static continuity equation for the current density,

$$\operatorname{div} \boldsymbol{j} = -\operatorname{div} \left[\sigma \frac{\partial}{\partial t} \left(\boldsymbol{A} + \operatorname{grad} \Phi \right) \right] = 0 \quad \text{in } G. \tag{3.8}$$

Equation (3.7) does not have a unique solution in terms of $\boldsymbol{A}$ and Φ. The uniqueness is enforced by applying the Coulomb gauge (Biro & Preis, 1989),

$$\operatorname{div} \boldsymbol{A} = 0 \quad \text{in } G. \tag{3.9}$$

Following Biro & Preis (1989), we apply the Coulomb gauge by addition of a penalty term in equation (3.7),

$$\operatorname{curl}\left(\frac{1}{\mu_0}\operatorname{curl}\boldsymbol{A}\right)-\operatorname{grad}\left(\frac{1}{\mu_0}\operatorname{div}\boldsymbol{A}\right)+\sigma\frac{\partial}{\partial t}\left(\boldsymbol{A}+\operatorname{grad}\Phi\right)=0\quad\text{in}\,G, \tag{3.10}$$

by constraining the solenoidality of current density (3.8) which is not automatically satisfied by (3.10), and by a homogeneous Dirichlet boundary condition applied on the normal component of the vector magnetic potential on the interface ∂G_2,

$$\boldsymbol{n}\cdot\boldsymbol{A}=0\quad\text{on}\,\partial G_2. \tag{3.11}$$

Assuming constant magnetic permeability μ_0, equations (3.10) and (3.8) can be further rewritten as,

$$-\nabla^2\boldsymbol{A}+\mu_0\,\sigma\frac{\partial}{\partial t}\left(\boldsymbol{A}+\operatorname{grad}\Phi\right) = 0\quad\text{in}\,G, \tag{3.12}$$

$$\operatorname{div}\left[\mu_0\,\sigma\frac{\partial}{\partial t}\left(\boldsymbol{A}+\operatorname{grad}\Phi\right)\right] = 0\quad\text{in}\,G. \tag{3.13}$$

Summed up, we replace the equations (3.7) and (3.9) by equations (3.12–3.13) holding in G and by the boundary condition (3.11) imposed on ∂G_2.

Since $\boldsymbol{B}=0$ and $\boldsymbol{E}=0$ in the infinitely conductive core, we impose the homogeneous Dirichlet boundary conditions on the core-mantle boundary,

$$\boldsymbol{A} = 0\quad\text{on}\,\partial G_1, \tag{3.14}$$

$$\Phi = 0\quad\text{on}\,\partial G_1. \tag{3.15}$$

As we have shown in Chapter 2, $\boldsymbol{B}$ changes continuously across the Earth's surface $\partial G_2\equiv\partial A_1$. Substitution of (3.1) and (3.4) into (2.7) implies the boundary condition for the vector and scalar magnetic potentials,

$$\operatorname{curl}\boldsymbol{A}=-\operatorname{grad}U\quad\text{on}\,\partial G_2\equiv\partial A_1. \tag{3.16}$$

Since no electrical current can flow into the insulator, the normal component of the current density must vanish at the Earth's surface,

$$\boldsymbol{n}\cdot\boldsymbol{j}=\boldsymbol{n}\cdot\sigma\boldsymbol{E}=-\sigma\frac{\partial}{\partial t}\left(\boldsymbol{n}\cdot\boldsymbol{A}+\boldsymbol{n}\cdot\operatorname{grad}\Phi\right)=0\quad\text{on}\,\partial G_2. \tag{3.17}$$

Taking into account (3.11), the equation (3.17) yields the boundary condition applied on the scalar electric potential only,

$$\boldsymbol{n}\cdot\operatorname{grad}\Phi=0\quad\text{on}\,\partial G_2. \tag{3.18}$$

In the insulating region, we solve the Laplace equation for scalar magnetic potential,

$$\nabla^2 U = 0 \quad \text{in } A. \tag{3.19}$$

The scalar potential of the primary inducing field of external origin is prescribed at the outer boundary ∂A_2,

$$U = U^{(e)} \quad \text{on } \partial A_2. \tag{3.20}$$

To complete the formulation we have to specify the initial conditions. The time evolution of the problem can be started from any initial state $({}^0\boldsymbol{A}, {}^0\Phi, {}^0U)$ that satisfies (3.9) and the boundary conditions (3.11), (3.14–3.16), (3.18), and (3.20).

Let us summarize the classical formulation of the $\boldsymbol{A}-\Phi, U$ method in the time-domain:

Let $\mu_0 > 0$ and $\sigma(\boldsymbol{r}) \in L^+_\infty(G) \cap C^1(G)$. Let $U^{(e)} \in C^2(\partial A_2) \times C^1(\langle 0, \infty))$ be the magnetic potential of the primary inducing field on ∂A_2. Let ${}^0\boldsymbol{A}(\boldsymbol{r}) \in C^2(G)^3$, ${}^0\Phi(\boldsymbol{r}) \in C^2(G)$, and ${}^0U(\boldsymbol{r}) \in C^2(A)$ be the initial values, such that $\operatorname{div} {}^0\boldsymbol{A} = 0$, ${}^0\boldsymbol{A} = 0$ and ${}^0\Phi = 0$ on ∂G_1, $\boldsymbol{n} \cdot {}^0\boldsymbol{A} = \boldsymbol{n} \cdot \operatorname{grad} {}^0\Phi = 0$ on ∂G_2, $\operatorname{curl} {}^0\boldsymbol{A} = -\operatorname{grad} {}^0U$ on $\partial G_2 \equiv \partial A_1$, and ${}^0U(a_O) = U^{(e)}(\Omega; 0)$. Find such functions $\boldsymbol{A}(\boldsymbol{r}; t) \in C^2(G)^3 \times C^1(\langle 0, \infty))^3$, $\Phi(\boldsymbol{r}; t) \in C^2(G) \times C^1(\langle 0, \infty))$, and $U(\boldsymbol{r}; t) \in C^2(A) \times C^1(\langle 0, \infty))$ that satisfy

$$\begin{aligned}
-\nabla^2 \boldsymbol{A} + \mu_0 \sigma \frac{\partial}{\partial t} (\boldsymbol{A} + \operatorname{grad} \Phi) &= 0 \quad \text{in } G, && (3.21)\\
\operatorname{div} \left[\mu_0 \sigma \frac{\partial}{\partial t} (\boldsymbol{A} + \operatorname{grad} \Phi) \right] &= 0 \quad \text{in } G, && (3.22)\\
\nabla^2 U &= 0 \quad \text{in } A, && (3.23)\\
\boldsymbol{A}(\boldsymbol{r}; 0) &= {}^0\boldsymbol{A} \quad \text{in } G, && (3.24)\\
\Phi(\boldsymbol{r}; 0) &= {}^0\Phi \quad \text{in } G, && (3.25)\\
U(\boldsymbol{r}; 0) &= {}^0U \quad \text{in } A, && (3.26)\\
\boldsymbol{A} &= 0 \quad \text{on } \partial G_1, && (3.27)\\
\Phi &= 0 \quad \text{on } \partial G_1, && (3.28)\\
\operatorname{curl} \boldsymbol{A} &= -\operatorname{grad} U \quad \text{on } \partial G_2 \equiv \partial A_1, && (3.29)\\
\boldsymbol{n} \cdot \boldsymbol{A} &= 0 \quad \text{on } \partial G_2, && (3.30)\\
\boldsymbol{n} \cdot \operatorname{grad} \Phi &= 0 \quad \text{on } \partial G_2, && (3.31)\\
U &= U^{(e)} \quad \text{on } \partial A_2. && (3.32)
\end{aligned}$$

We refer to Appendix F.2 for definitions of functional spaces.

3.1.2 Integral (weak) formulation

In order to derive the integral $\boldsymbol{A}-\Phi,U$ formulation of the EM induction problem (3.21–3.32), we respectively multiply equations (3.21), (3.22), and (3.23) by test functions $\delta\boldsymbol{A}\in W_{01}^{1,2}(G)^3\cap C^2(G)^3$, $\delta\Phi\in W_{01}^{1,2}(G)\cap C^2(G)$, and $\delta U\in W_{02}^{1,2}(A)\cap C^2(A)$, integrate over domains G and A, and apply the Green theorems

$$\begin{aligned}\int\limits_G \boldsymbol{f}\cdot\nabla^2\boldsymbol{g}\,dV &= -\int\limits_G \operatorname{grad}\boldsymbol{f}:(\operatorname{grad}\boldsymbol{g})^T\,dV+\int\limits_{\partial G_1\cup\partial G_2}\boldsymbol{f}\cdot\operatorname{grad}\boldsymbol{g}\cdot\boldsymbol{n}\,dS-\\ &\quad-\int\limits_{\partial G_1\cup\partial G_2}\boldsymbol{f}\cdot\boldsymbol{n}\times\operatorname{curl}\boldsymbol{g}\,dS \qquad (3.33)\\ \int\limits_G(\operatorname{div}\boldsymbol{f})\;h\,dV &= -\int\limits_G\boldsymbol{f}\cdot\operatorname{grad}h\,dV+\int\limits_{\partial G_1\cup\partial G_2}(\boldsymbol{n}\cdot\boldsymbol{f})\;h\,dS, \qquad (3.34)\\ \int\limits_A f\,\nabla^2 g\,dV &= -\int\limits_A\operatorname{grad}f\cdot\operatorname{grad}g\,dV+\int\limits_{\partial A_1\cup\partial A_2}f\,\boldsymbol{n}\cdot\operatorname{grad}g\,dS. \qquad (3.35)\end{aligned}$$

Integrals over the boundaries ∂G_1 and ∂A_2 are zero because the homogeneous Dirichlet boundary conditions are imposed on the test functions there, and we obtain

$$\begin{aligned}\int\limits_G\left[\operatorname{grad}\delta\boldsymbol{A}:(\operatorname{grad}\boldsymbol{A})^T+\mu_0\,\sigma\,\delta\boldsymbol{A}\cdot\frac{\partial}{\partial t}\left(\boldsymbol{A}+\operatorname{grad}\Phi\right)\right]dV &-\\ -\int\limits_{\partial G_2}\delta\boldsymbol{A}\cdot\operatorname{grad}\boldsymbol{A}\cdot\boldsymbol{n}\,dS+\int\limits_{\partial G_2}\delta\boldsymbol{A}\cdot\boldsymbol{n}\times\operatorname{curl}\boldsymbol{A}\,dS &= 0, \qquad (3.36)\\ \int\limits_G\mu_0\,\sigma\operatorname{grad}\delta\Phi\cdot\frac{\partial}{\partial t}\left(\boldsymbol{A}+\operatorname{grad}\Phi\right)dV-\int\limits_{\partial G_2}\mu_0\,\sigma\,\delta\Phi\,\boldsymbol{n}\cdot\frac{\partial}{\partial t}\left(\boldsymbol{A}+\operatorname{grad}\Phi\right)dS &= 0, \qquad (3.37)\\ -\int\limits_A\operatorname{grad}\delta U\cdot\operatorname{grad}U\;dV+\int\limits_{\partial A_1}\delta U\,\boldsymbol{n}\cdot\operatorname{grad}U\,dS &= 0. \qquad (3.38)\end{aligned}$$

The first surface integral in equation (3.36) and the surface integral in equation (3.37) are zero due to (3.30) and (3.31), respectively. The boundary condition (3.29) is realized by interchanging $\operatorname{curl}\boldsymbol{A}$ and $-\operatorname{grad}U$ in the remaining surface integrals in (3.36) and (3.38). These surface integrals couple the solution in the conductive mantle G to the solution in the insulating layer A (Biro & Preis, 1989, 1990; Everett & Schultz, 1996). By releasing the smoothness constraint on the potentials and test functions, we come to the weak form of the $\boldsymbol{A}-\Phi,U$ formulation:

Let $\mu_0 > 0$ and $\sigma(\boldsymbol{r}) \in L^+_\infty(G)$. Let $\hat{U}(\boldsymbol{r};t)$ be such a function from $W^{1,2}(A) \times C^1(\langle 0,\infty))$ that $\hat{U}(a_O,\Omega;t) = U^{(e)}(\Omega;t)$ on ∂A_2. Let ${}^0\boldsymbol{A}(\boldsymbol{r}) \in W^{1,2}_{01}(G)^3$, ${}^0\Phi(\boldsymbol{r}) \in W^{1,2}_{01}(G)$, and ${}^0U(\boldsymbol{r}) \in W^{1,2}(A)$ be the initial values. Find $\boldsymbol{A}(\boldsymbol{r};t) \in W^{1,2}_{01}(G)^3 \times C^1(\langle 0,\infty))^3$, $\Phi(\boldsymbol{r};t) \in W^{1,2}_{01}(G) \times C^1(\langle 0,\infty))$, and $U(\boldsymbol{r};t) \in W^{1,2}(A) \times C^1(\langle 0,\infty))$, such that $U - \hat{U} \in W^{1,2}_{02}(A)$ and

$$\int_G \left[\operatorname{grad} \delta\boldsymbol{A} : (\operatorname{grad} \boldsymbol{A})^T + \mu_0 \sigma\, \delta\boldsymbol{A} \cdot \frac{\partial}{\partial t} (\boldsymbol{A} + \operatorname{grad}\Phi) \right] dV -$$

$$- \int_{\partial G_2} \delta\boldsymbol{A} \cdot \boldsymbol{n} \times \operatorname{grad} U \; dS \;\; = 0 \quad \forall\, \delta\boldsymbol{A} \in W^{1,2}_{01}(G)^3, \quad (3.39)$$

$$\int_G \mu_0 \sigma \operatorname{grad} \delta\Phi \cdot \frac{\partial}{\partial t} (\boldsymbol{A} + \operatorname{grad}\Phi)\; dV \;\; = 0 \quad \forall\, \delta\Phi \in W^{1,2}_{01}(G), \quad (3.40)$$

$$- \int_A \operatorname{grad} \delta U \cdot \operatorname{grad} U \; dV - \int_{\partial A_1} \delta U \boldsymbol{n} \cdot \operatorname{curl} \boldsymbol{A}\, dS \;\; = 0 \quad \forall\, \delta U \in W^{1,2}_{02}(A). \quad (3.41)$$

3.1.3 Time integration scheme

As we will show in the next section, the use of the 3-D nodal finite elements in the Galerkin discretization of the integral problem (3.39–3.41) leads to a system of linear equations which is much sparser than in the case of the spectral-finite element method introduced in Chapter 2. The reason is that the finite element base functions have local support and introduce less coupling in the Galerkin matrix, than the spherical harmonic functions. Therefore, the application of an implicit time integration method becomes feasible. We use the Crank-Nicolson scheme (Press et al., 1992) which is unconditionally stable and second order accurate in time.

Let us denote ${}^i\boldsymbol{A}$, ${}^i\Phi$, ${}^iU$ the solution of (3.39–3.41) at $t = t_i$. The substitution of time derivatives,

$$\frac{\partial \boldsymbol{A}}{\partial t} \approx \frac{{}^{i+1}\boldsymbol{A} - {}^i\boldsymbol{A}}{\Delta t}, \quad (3.42)$$

$$\frac{\partial \Phi}{\partial t} \approx \frac{{}^{i+1}\Phi - {}^i\Phi}{\Delta t}, \quad (3.43)$$

and of midpoint values,

$$\boldsymbol{A} \approx \frac{{}^{i+1}\boldsymbol{A} + {}^i\boldsymbol{A}}{2}, \quad (3.44)$$

$$\Phi \approx \frac{{}^{i+1}\Phi + {}^{i}\Phi}{2}, \tag{3.45}$$

$$U \approx \frac{{}^{i+1}U + {}^{i}U}{2}, \tag{3.46}$$

into (3.39–3.41) yields the integral formulation discretized in time:

Let ${}^{i+1}\hat{U}(\boldsymbol{r})$ be such a function from $W^{1,2}(A)$ that ${}^{i+1}\hat{U}(a_O,\Omega) = U^{(e)}(\Omega;t_{i+1})$ on ∂A_2. Find ${}^{i+1}\boldsymbol{A}(\boldsymbol{r}) \in W_{01}^{1,2}(G)^3$, ${}^{i+1}\Phi(\boldsymbol{r}) \in W_{01}^{1,2}(G)$, and ${}^{i+1}U(\boldsymbol{r}) \in W^{1,2}(A)\ \forall\, i = 1,2,\ldots$, such that ${}^{i+1}U - {}^{i+1}\hat{U} \in W_{02}^{1,2}(A)$, and

$$\int_G \left[\frac{1}{2}\operatorname{grad}\delta\boldsymbol{A} : (\operatorname{grad}{}^{i+1}\boldsymbol{A})^T + \frac{\mu_0\,\sigma}{\Delta t}\,\delta\boldsymbol{A}\cdot\left({}^{i+1}\boldsymbol{A} + \operatorname{grad}{}^{i+1}\Phi\right)\right] dV \quad -(3.47)$$

$$-\int_{\partial G_2}\frac{1}{2}\,\delta\boldsymbol{A}\cdot\boldsymbol{n}\times\operatorname{grad}{}^{i+1}U\,dS =$$

$$= \int_G \left[-\frac{1}{2}\operatorname{grad}\delta\boldsymbol{A} : (\operatorname{grad}{}^{i}\boldsymbol{A})^T + \frac{\mu_0\,\sigma}{\Delta t}\,\delta\boldsymbol{A}\cdot\left({}^{i}\boldsymbol{A} + \operatorname{grad}{}^{i}\Phi\right)\right] dV \quad +$$

$$+\int_{\partial G_2}\frac{1}{2}\,\delta\boldsymbol{A}\cdot\boldsymbol{n}\times\operatorname{grad}{}^{i}U\,dS \quad \forall\,\delta\boldsymbol{A}\in W_{01}^{1,2}(G)^3, \tag{3.48}$$

$$\int_G \frac{\mu_0\,\sigma}{\Delta t}\operatorname{grad}\delta\Phi\cdot\left({}^{i+1}\boldsymbol{A} + \operatorname{grad}{}^{i+1}\Phi\right) dV =$$

$$= \int_G \frac{\mu_0\,\sigma}{\Delta t}\operatorname{grad}\delta\Phi\cdot\left({}^{i}\boldsymbol{A} + \operatorname{grad}{}^{i}\Phi\right) dV \quad \forall\,\delta\Phi\in W_{01}^{1,2}(G), \tag{3.49}$$

$$-\int_A \frac{1}{2}\operatorname{grad}\delta U\cdot\operatorname{grad}{}^{i+1}U\,dV - \int_{\partial A_1}\frac{1}{2}\,\delta U\,\boldsymbol{n}\cdot\operatorname{curl}{}^{i+1}\boldsymbol{A}\,dS =$$

$$= \int_A \frac{1}{2}\operatorname{grad}\delta U\cdot\operatorname{grad}{}^{i}U\,dV + \int_{\partial A_1}\frac{1}{2}\,\delta U\,\boldsymbol{n}\cdot\operatorname{curl}{}^{i}\boldsymbol{A}\,dS \quad \forall\,\delta U\in W_{02}^{1,2}(A). \tag{3.50}$$

The existence and uniqueness of the 3-D finite element solution can be proved analogously to the spectral-finite element method, as discussed in Appendix B (see also Křížek & Neittaanmäki, 1990; Martinec, 1997). Note that the solution does not depend on a particular choice of ${}^{i+1}\hat{U}$.

3.1.4 Discretization using 3-D nodal finite elements

Now we will introduce the discrete form of (3.48–3.50) using 3-D piecewise linear nodal finite elements defined on a tetrahedral mesh. A reader not familiar with this technique is advised to read Appendix C that introduces a particular method of tetrahedral mesh generation in a spherical shell, and Appendix D where the 3-D piecewise linear nodal finite elements are defined, before proceeding.

Let us assume that the spherical shells G and A are approximated by concave polyhedra composed respectively of N_t^i and N_t^e non-overlapping, conforming tetrahedra. The mesh nodes are arranged in such a way that the first N_n^c nodes are on the innermost boundary ∂G_1, next $N_n^i - N_n^c - N_n^s$ nodes are interior nodes of G, followed by N_n^s nodes on the interface $\partial G_2 = \partial A_1$, $N_n^e - N_n^s - N_n^o$ interior nodes of A, and N_n^o nodes on the outermost boundary ∂A_2. The total number of nodes is then $N_n^i + N_n^e - N_n^s$, since the N_n^s interface nodes are included both in N_n^i and N_n^e.

Using the piecewise linear nodal base functions Ψ_q (see Appendix D), we define the finite dimensional approximations of functional spaces $W_{01}^{1,2}(G)^3$, $W_{01}^{1,2}(G)$, $W_{02}^{1,2}(A)$, and $W^{1,2}(A)$,

$$W_{01}^{1,2,h}(G)^3 = \left\{ \boldsymbol{f}(\boldsymbol{r}) \,\middle|\, \boldsymbol{f}(\boldsymbol{r}) = \sum_{q=N_n^c+1}^{N_n^i} \left(f_{x,q}\,\boldsymbol{e}_x + f_{y,q}\,\boldsymbol{e}_y + f_{z,q}\,\boldsymbol{e}_z\right) \Psi_q(\boldsymbol{r}) \right\}, \quad (3.51)$$

$$W_{01}^{1,2,h}(G) = \left\{ f(\boldsymbol{r}) \,\middle|\, f(\boldsymbol{r}) = \sum_{q=N_n^c+1}^{N_n^i} f_q\,\Psi_q(\boldsymbol{r}) \right\}, \quad (3.52)$$

$$W_{02}^{1,2,h}(A) = \left\{ f(\boldsymbol{r}) \,\middle|\, f(\boldsymbol{r}) = \sum_{q=N_n^i-N_n^s+1}^{N_n^i+N_n^e-N_n^s-N_n^o} f_q\,\Psi_q(\boldsymbol{r}) \right\}, \quad (3.53)$$

$$W^{1,2,h}(A) = \left\{ f(\boldsymbol{r}) \,\middle|\, f(\boldsymbol{r}) = \sum_{q=N_n^i-N_n^s+1}^{N_n^i+N_n^e-N_n^s} f_q\,\Psi_q(\boldsymbol{r}) \right\}, \quad (3.54)$$

and expand the potentials ${}^i\boldsymbol{A}$, ${}^i\Phi$, ${}^iU$, and the boundary condition ${}^i\hat{U}$ at the i-th time step into series,

$${}^i\boldsymbol{A}(\boldsymbol{r}) = \sum_{q=N_n^c+1}^{N_n^i} \left({}^iA_{x,q}\,\boldsymbol{e}_x + {}^iA_{y,q}\,\boldsymbol{e}_y + {}^iA_{z,q}\,\boldsymbol{e}_z\right) \Psi_q(\boldsymbol{r}), \quad (3.55)$$

$${}^i\Phi(\boldsymbol{r}) = \sum_{q=N_n^c+1}^{N_n^i} {}^i\Phi_q\,\Psi_q(\boldsymbol{r}), \quad (3.56)$$

$$ {}^{i}U(\boldsymbol{r}) - {}^{i}\hat{U}(\boldsymbol{r}) = \sum_{q=N_n^i-N_n^s+1}^{N_n^i+N_n^e-N_n^s-N_n^o} {}^{i}U_q \, \Psi_q(\boldsymbol{r}), \tag{3.57} $$

$$ {}^{i}\hat{U}(\boldsymbol{r}) = \sum_{q=N_n^i+N_n^e-N_n^s-N_n^o+1}^{N_n^i+N_n^e-N_n^s} {}^{i}\hat{U}_q \, \Psi_q(\boldsymbol{r}). \tag{3.58} $$

Note that the base functions corresponding to nodes placed on boundaries ∂G_1 and ∂A_2 are left out from definitions of spaces $W_{01}^{1,2,h}(G)^k$ and $W_{02}^{1,2}(A)$, respectively.

We arrange the coefficients of electromagnetic potentials at the i-th time step, ${}^{i}A_{x,q}$, ${}^{i}A_{y,q}$, ${}^{i}A_{z,q}$, ${}^{i}\Phi_q$, and ${}^{i}U_q$, into vector

$$ {}^{i}\boldsymbol{x} = \left[\left({}^{i}A_{x,q}, {}^{i}A_{y,q}, {}^{i}A_{z,q}, {}^{i}\Phi_q \right)_{q=N_n^c+1}^{N_n^i} , \left({}^{i}U_q \right)_{q=N_n^i-N_n^s+1}^{N_n^i+N_n^e-N_n^s-N_n^o} \right], \tag{3.59} $$

with dimension $d_x = 4\,(N_n^i - N_n^c) + N_n^e - N_n^o$, and the coefficients of the scalar magnetic potential prescribed at the outer boundary, ${}^{i}\hat{U}_q$, into vector

$$ {}^{i}\boldsymbol{y} = \left({}^{i}\hat{U}_q \right)_{q=N_n^i+N_n^e-N_n^s-N_n^o+1}^{N_n^i+N_n^e-N_n^s} , \tag{3.60} $$

with dimension $d_y = N_n^o$. By substituting (3.55–3.58) into the integral equations (3.48–3.50), and taking successively the base functions $\boldsymbol{e}_x\Psi_p$, $\boldsymbol{e}_y\Psi_p$, $\boldsymbol{e}_z\Psi_p$, Ψ_p for $p = N_n^c + 1, \ldots, N_n^i$ in place of $\delta\boldsymbol{A}$, $\delta\Phi$, and Ψ_p for $p = N_n^i - N_n^s + 1, \ldots, N_n^i + N_n^e - N_n^s - N_n^o$ in place of δU, we obtain a linear system

$$ \mathcal{A} \cdot {}^{i+1}\boldsymbol{x} = \mathcal{B} \cdot {}^{i}\boldsymbol{x} + \mathcal{C} \cdot ({}^{i}\boldsymbol{y} + {}^{i+1}\boldsymbol{y}). \tag{3.61} $$

Matrices $\mathcal{A}$, $\mathcal{B}$, and $\mathcal{C}$ have dimensions $d_x \times d_x$, $d_x \times d_x$, and $d_x \times d_y$, respectively. Křížek & Neittaanmäki (1990) introduce two technique which can be used to construct the finite element matrices, "node by node" and "element by element." We employ the later one where the matrices $\mathcal{A}$, $\mathcal{B}$, and $\mathcal{C}$ are assembled from the submatrices associated to individual tetrahedra.

Let T_κ be the tetrahedra of the interior ($\kappa = 1, \ldots, N_t^i$) and exterior ($\kappa = N_t^i + 1, \ldots, N_t^i + N_t^e$) mesh. The mantle-atmosphere interface ∂G_2 is approximated by triangular facets F_η, $\eta = 1, \ldots, N_t^s$ with outer normals $\boldsymbol{n}_\eta$ oriented outward from the Earth's centre. Let the conductivity σ be a piecewise constant function,

$$ \sigma(\boldsymbol{r}) = \sigma_\kappa = \text{const} \quad \text{in } T_\kappa,\ \kappa = 1, \ldots, N_t^i. \tag{3.62} $$

Then we construct the matrices $\mathcal{A}$, $\mathcal{B}$, $\mathcal{C}$ as sums of contributions of individual interior tetrahedra, surface facets, and exterior tetrahedra,

$$ \mathcal{A} = \sum_{\kappa=1}^{N_t^i} (\mathcal{P}_\kappa + \mathcal{Q}_\kappa) + \sum_{\eta=1}^{N_t^s} \mathcal{R}_\eta + \sum_{\kappa=N_t^i+1}^{N_t^i+N_t^e} \mathcal{S}_\kappa, \tag{3.63} $$

$$\mathcal{B} = \sum_{\kappa=1}^{N_t^i}(\mathcal{P}_\kappa - \mathcal{Q}_\kappa) - \sum_{\eta=1}^{N_t^s}\mathcal{R}_\eta - \sum_{\kappa=N_t^i+1}^{N_t^i+N_t^e}\mathcal{S}_\kappa, \tag{3.64}$$

$$\mathcal{C} = \sum_{\kappa=N_t^i+1}^{N_t^i+N_t^e}\mathcal{T}_\kappa. \tag{3.65}$$

Matrices $\mathcal{P}_\kappa$ and $\mathcal{Q}_\kappa$ corresponding to the volume integrals in equations (3.48–3.49) consist respectively of 4×4 and 3×3 blocks,

$$\frac{\mu_0\,\sigma_\kappa}{\Delta t}\begin{array}{c} \begin{matrix} {\scriptstyle 4\,(q-N_n^c)-3} & \cdots & \cdots & {\scriptstyle 4\,(q-N_n^c)} \end{matrix} \\ \begin{pmatrix} I_\kappa^{pq} & 0 & 0 & \boldsymbol{e}_x\cdot\boldsymbol{J}_\kappa^{pq} \\ 0 & I_\kappa^{pq} & 0 & \boldsymbol{e}_y\cdot\boldsymbol{J}_\kappa^{pq} \\ 0 & 0 & I_\kappa^{pq} & \boldsymbol{e}_z\cdot\boldsymbol{J}_\kappa^{pq} \\ \boldsymbol{e}_x\cdot\boldsymbol{J}_\kappa^{qp} & \boldsymbol{e}_y\cdot\boldsymbol{J}_\kappa^{qp} & \boldsymbol{e}_z\cdot\boldsymbol{J}_\kappa^{qp} & K_\kappa^{pq} \end{pmatrix} \end{array} \begin{array}{c} {\scriptstyle 4\,(p-N_n^c)-3} \\ \vdots \\ \vdots \\ {\scriptstyle 4\,(p-N_n^c)} \end{array}, \tag{3.66}$$

$$\frac{1}{2}\begin{array}{c} \begin{matrix} {\scriptstyle 4\,(q-N_n^c)-3} & \cdots & {\scriptstyle 4\,(q-N_n^c)-1} \end{matrix} \\ \begin{pmatrix} K_\kappa^{pq} & 0 & 0 \\ 0 & K_\kappa^{pq} & 0 \\ 0 & 0 & K_\kappa^{pq} \end{pmatrix} \end{array} \begin{array}{c} {\scriptstyle 4\,(p-N_n^c)-3} \\ \vdots \\ {\scriptstyle 4\,(p-N_n^c)-1} \end{array}, \tag{3.67}$$

for interior nodes $N_n^c < p,q \le N_n^i$, $\boldsymbol{r}_p, \boldsymbol{r}_q \in T_\kappa$. Volume integrals I_κ^{pq}, $\boldsymbol{J}_\kappa^{pq}$, and K_κ^{pq} are defined in Appendix D.

Matrices $\mathcal{R}_\eta$ represent the contribution of the surface integrals over the mantle-atmosphere interface. They include 3×1 and 1×3 blocks,

$$-\frac{1}{2}\begin{array}{c} \begin{matrix} {\scriptstyle 4\,(N_n^i-N_n^c)+q-(N_n^i-N_n^s)} \end{matrix} \\ \begin{pmatrix} \boldsymbol{e}_x\cdot\boldsymbol{L}_\eta^{pq} \\ \boldsymbol{e}_y\cdot\boldsymbol{L}_\eta^{pq} \\ \boldsymbol{e}_z\cdot\boldsymbol{L}_\eta^{pq} \end{pmatrix} \end{array} \begin{array}{c} {\scriptstyle 4\,(p-N_n^c)-3} \\ \vdots \\ {\scriptstyle 4\,(p-N_n^c)-1} \end{array}, \tag{3.68}$$

$$\frac{1}{2}\begin{array}{c} \begin{matrix} {\scriptstyle 4\,(q-N_n^c)-3} & \cdots & {\scriptstyle 4\,(q-N_n^c)-1} \end{matrix} \\ \begin{pmatrix} \boldsymbol{e}_x\cdot\boldsymbol{L}_\eta^{pq} & \boldsymbol{e}_y\cdot\boldsymbol{L}_\eta^{pq} & \boldsymbol{e}_z\cdot\boldsymbol{L}_\eta^{pq} \end{pmatrix} \end{array} \quad {\scriptstyle 4\,(N_n^i-N_n^c)+p-(N_n^i-N_n^s)}\ , \tag{3.69}$$

for surface nodes $N_n^i - N_n^s < p,q \le N_n^i$, and $\boldsymbol{r}_p, \boldsymbol{r}_q \in F_\eta$. See Appendix D for definition of surface integrals $\boldsymbol{L}_\eta^{pq}$. Note the opposite signs due to the orientation of outer normals on ∂G_2 and ∂A_1.

Matrices $\mathcal{S}_\kappa$ include the terms corresponding to the volume integral (3.50),

$$\begin{matrix} {\scriptstyle 4\,(N_n^i-N_n^c)+q-(N_n^i-N_n^s)} \\ \left(-\frac{1}{2}\,K_\kappa^{pq}\right) \end{matrix} \qquad {\scriptstyle 4\,(N_n^i-N_n^c)+p-(N_n^i-N_n^s),} \tag{3.70}$$

for exterior mesh nodes $N_n^i - N_n^s < p, q \leq N_n^i + N_n^e - N_n^s - N_n^o$, and $\boldsymbol{r}_p, \boldsymbol{r}_q \in T_\kappa$.

Similarly, matrices $\mathcal{T}_\kappa$ representing the Dirichlet boundary value consist of terms,

$$\begin{matrix} {\scriptstyle q-(N_n^i+N_n^e-N_n^s-N_n^o)} \\ \left(-\frac{1}{2}\,K_\kappa^{pq}\right) \end{matrix} \qquad {\scriptstyle 4\,(N_n^i-N_n^c)+p-(N_n^i-N_n^s),} \tag{3.71}$$

for $N_n^i - N_n^s < p \leq N_n^i + N_n^e - N_n^s - N_n^o$, $N_n^i + N_n^e - N_n^s - N_n^o < q \leq N_n^i + N_n^e - N_n^s$, and $\boldsymbol{r}_p, \boldsymbol{r}_q \in T_\kappa$.

Since $\mathcal{P}_\kappa$, $\mathcal{Q}_\kappa$, $\mathcal{S}_\kappa$ are symmetric matrices, and since $\sum_{\eta=1}^{N_t^s} \mathcal{R}_\eta$ is symmetric due to equation (D 14), the resulting Galerkin matrices $\mathcal{A}$ and $\mathcal{B}$ are also symmetric. Their lower triangular parts can be stored effectively using a sparse storage scheme (Press et al., 1996). Matrix $\mathcal{A}$ is indefinite. While the first $4\,(N_n^i - N_n^c)$ diagonal terms corresponding to the interior mesh nodes are positive, the next $N_n^e - N_n^o$ diagonal terms corresponding to the exterior mesh nodes are negative.

Various numerical methods can be applied to solve the linear system (3.61). Using the complete LU decomposition of $\mathcal{A}$ (IMSL, 1994) is the fastest way to solve (3.61) repeatedly. However, the memory and computational requirements of the initial factorization of $\mathcal{A}$ limit its use only to problems with small spatial resolution.

One of the methods designed for solution of large sparse symmetric linear systems is the preconditioned conjugate gradient (PCG) method (Press et al., 1992). Although the convergence is assured only for positive definite matrices, it can be used as a general iterative procedure even for indefinite symmetric systems. The incomplete LU decomposition,

$$\mathcal{A} \approx \mathcal{L} \cdot \mathcal{U} \tag{3.72}$$

which neglects additional fill-ins during the factorization of $\mathcal{A}$ is computed initially and is used as a preconditioner for the iterative process.

At each time level t_{i+1}, the iterations are started from the solution obtained in the previous time step, ${}^i\boldsymbol{x}$, and the right-hand side $\boldsymbol{b}$ of (3.61) is constructed,

$${}^{i+1}\boldsymbol{x}_0 = {}^i\boldsymbol{x}, \tag{3.73}$$

$$\boldsymbol{b} = \mathcal{B} \cdot {}^i\boldsymbol{x} + \mathcal{C} \cdot ({}^i\boldsymbol{y} + {}^{i+1}\boldsymbol{y}). \tag{3.74}$$

Although the actual difference between ${}^{i+1}\boldsymbol{x}$ and ${}^i\boldsymbol{x}$ depends on the length of time step, and on the corresponding change of the boundary condition, the initial guess (3.73) reduces the number of PCG iterations compared with the usual zero starting value.

Then, using the auxiliary vectors $\boldsymbol{r}^k$, $\boldsymbol{p}^k$, $\boldsymbol{z}^k$, and coefficients α, β with initial values,

$$\begin{aligned} \boldsymbol{r}_0 &= \boldsymbol{b} - \mathcal{A} \cdot {}^{i+1}\boldsymbol{x}_0, && (3.75)\\ \mathcal{L} \cdot \mathcal{U} \cdot \boldsymbol{z}_0 &= \boldsymbol{r}_0, && (3.76)\\ \boldsymbol{p}_0 &= \boldsymbol{z}_0, && (3.77) \end{aligned}$$

we repeatedly compute for $k = 1, 2, \ldots$,

$$\begin{aligned} \alpha^k &= \frac{\boldsymbol{z}^{k-1} \cdot \boldsymbol{r}^{k-1}}{\boldsymbol{p}^{k-1} \cdot \mathcal{A} \cdot \boldsymbol{p}^{k-1}}, && (3.78)\\ {}^{i+1}\boldsymbol{x}^k &= {}^{i+1}\boldsymbol{x}^{k-1} + \alpha^k \, \mathcal{A} \cdot \boldsymbol{p}^{k-1}, && (3.79)\\ \boldsymbol{r}^k &= \boldsymbol{r}^{k-1} - \alpha^k \, \mathcal{A} \cdot \boldsymbol{p}^{k-1}, && (3.80)\\ \mathcal{L} \cdot \mathcal{U} \cdot \boldsymbol{z}^k &= \boldsymbol{r}^k, && (3.81)\\ \beta^k &= \frac{\boldsymbol{z}^k \cdot \boldsymbol{r}^k}{\boldsymbol{z}^{k-1} \cdot \boldsymbol{r}^{k-1}}, && (3.82)\\ \boldsymbol{p}^k &= \boldsymbol{z}^k + \beta^k \, \boldsymbol{p}^{k-1}, && (3.83) \end{aligned}$$

until the norm of the residuum vector $\boldsymbol{r}^k$, scaled by the norm of the right-hand side,

$$\varepsilon = \left(\frac{\boldsymbol{r}^k \cdot \boldsymbol{r}^k}{\boldsymbol{b} \cdot \boldsymbol{b}} \right)^{\frac{1}{2}}, \qquad (3.84)$$

is smaller than a given tolerance ε_0. We use the value $\varepsilon_0 = 10^{-6}$ in following computations.

During each iteration step we compute one matrix multiplication $\mathcal{A} \cdot \boldsymbol{p}^{k-1}$, and solve the factorized linear system (3.81) by backsubstitution. The number of iterations is variable, and generally increases for complicated 3-D conductivity models. We have also employed another preconditioned iterative method used by Everett & Schultz (1996). However it required about twice more iterations than the PCG method during test runs with various conductivity models.

3.2 Validation

3.2.1 Axially symmetric conductivity model

Firstly we validate the 3-D finite element method against the 2-D time-domain spectral-finite element approach by Martinec et al. (2002) which computes the response of axially symmetric conductivity models to axially symmetric transient external excitation signals. The 2-D solution does not represent an exhaustive test of 3-D methods, since it does not include the galvanic term $\mu_0 \sigma \mathrm{grad} \frac{\partial \Phi}{\partial t}$ in the equation of EM induction (3.21),

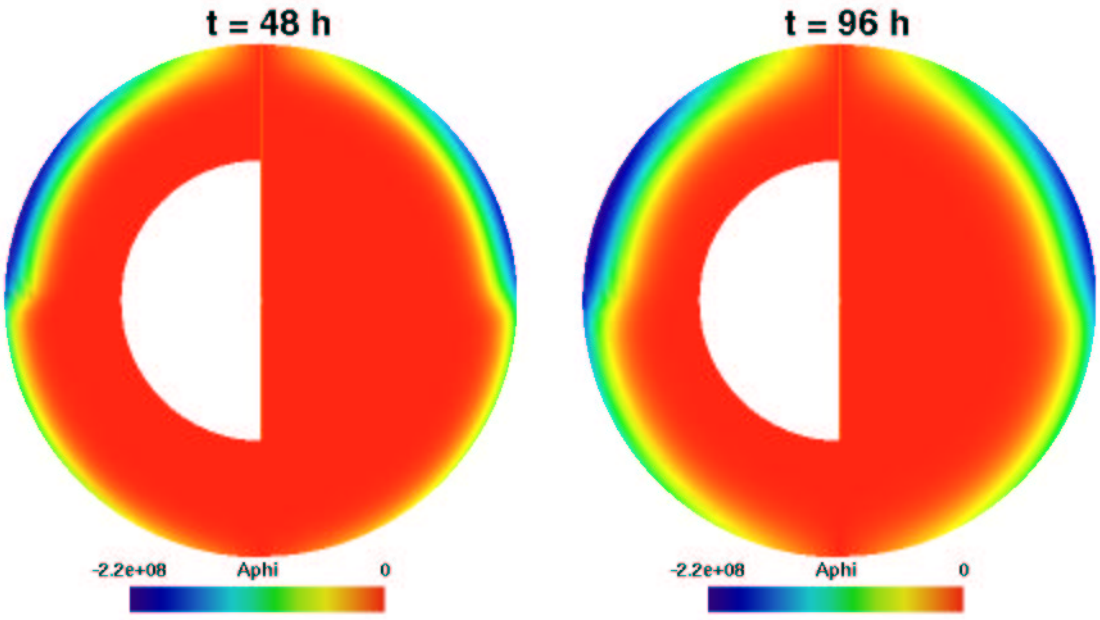

Figure 3.2: The longitudinal component of magnetic vector potential, A_φ, in nA for the axially symmetric model excited by Load 2 shown for two time levels. Results obtained by the 3-D finite element computation are plotted on the left hemisphere. The right hemisphere corresponds to the 2-D spectral-finite element time-domain approach, with highly conductive core ($\sigma = 10^{14}\,\mathrm{S/m}$).

and can be expressed using only the longitudinal (toroidal) component of the vector magnetic potential A_φ (Everett & Schultz, 1996; Martinec et al., 2002). On the other hand, the potentials A_φ obtained by both methods are directly comparable, and subsequent numerical differentiation to compute $\boldsymbol{B}$ is not necessary to perform.

In the presented example we prescribe a homogeneous mantle with conductivity $1\,\mathrm{S/m}$. In the northern hemisphere we overlay the mantle by a 700 km thick layer with conductivity $0.1\,\mathrm{S/m}$. Since the 2-D spectral-finite element method does not assume an infinitely conductive core, we approximate it by a sphere with conductivity of $10^{14}\,\mathrm{S/m}$. The model is excited by the analytical model of a geomagnetic storm introduced as "Load 2" by equation (2.111) in Chapter 2, with amplitude $A = 0.003\,\mathrm{nT/s}$ and relaxation time $1/\alpha = 48\,\mathrm{h}$. The external excitation field is prescribed directly by the means of the dipolar spherical harmonic coefficient in the 2-D method. In the 3-D finite element method, the Dirichlet boundary condition prescribed at nodes $\boldsymbol{r}_q \in \partial A_2$ is constructed by the substitution of (2.111) into (2.11),

$$ {}^{i}\hat{U}_q = A\,t\,e^{-\alpha\,t}\,z_q. \tag{3.85}$$

Figure 3.2 compares two snapshots of A_φ obtained by both methods at two time levels. The 3-D finite element solution was computed on a regular tetrahedral mesh

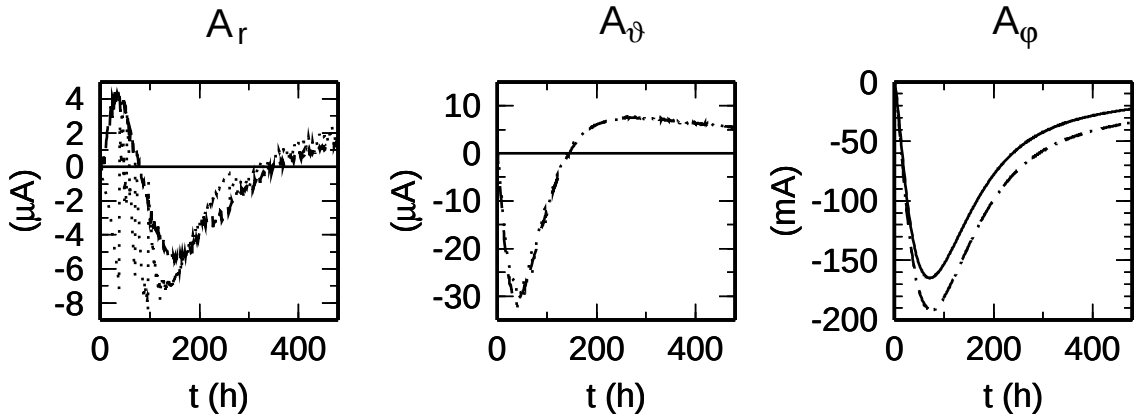

Figure 3.3: Time evolution of the spherical components of $\boldsymbol{A}$ at the surface point $(\vartheta, \varphi) = (45°, 0)$ is shown for the axially symmetric model excited by Load 2. Dashed, dotted, and solid lines correspond to the 3-D finite element solutions on meshes $M_{5,20}$, $M_{5,33}$, and to the 2-D spectral-finite element solution, respectively.

$M_{5,20}$ (see Table C.1). The 2-D spectral-finite element method used 100 finite elements in the radial direction, and the spherical harmonic expansion was truncated at $j_{max} = 40$. The integration time step in both methods was set to 1 h. The time-evolution of both solution at a particular point at the surface is plotted in Figure 3.3. Good agreement is obtained in both the spatial and temporal shape of A_φ. The finite triangulation of the Earth's surface causes that the axisymmetry of the 3-D finite element solution is disturbed which leads to small non-zero components A_r and A_ϑ. Moreover, Figure 3.3 shows also the 3-D finite element solution computed on a tetrahedral mesh $M_{5,33}$. While this mesh discretizes the spherical shell G in the same way as $M_{5,20}$, the outer boundary of A, ∂A_2 is positioned at $a_O = 10.245\, a$ in $M_{5,33}$, compared to $a_O = 4.068\, a$ in the case of $M_{5,20}$. Note that the increase of a_O is not reflected in A_φ. This validates the choice of $a_O \approx 4\, a$ used in the presented runs.

3.2.2 Nested-sphere conductivity model

The next example validates the 3-D finite element solver against the semi-analytical solution for a nested sphere conductivity model introduced in Section 2.2.1. The off-axis position of the spherical inclusion yields a fully 3-D solution including the galvanic effect.

The nested spheres conductivity Models A and B that were used in the validation examples in Chapter 2 contain a spherical inclusion of a comparable size to the Earth's core. Such inclusion is too large to fit into the spherical shell G that approximates the Earth's mantle in the 3-D finite element solver. Therefore we introduce another nested spheres configuration, Model C, with a smaller spherical inclusion positioned in

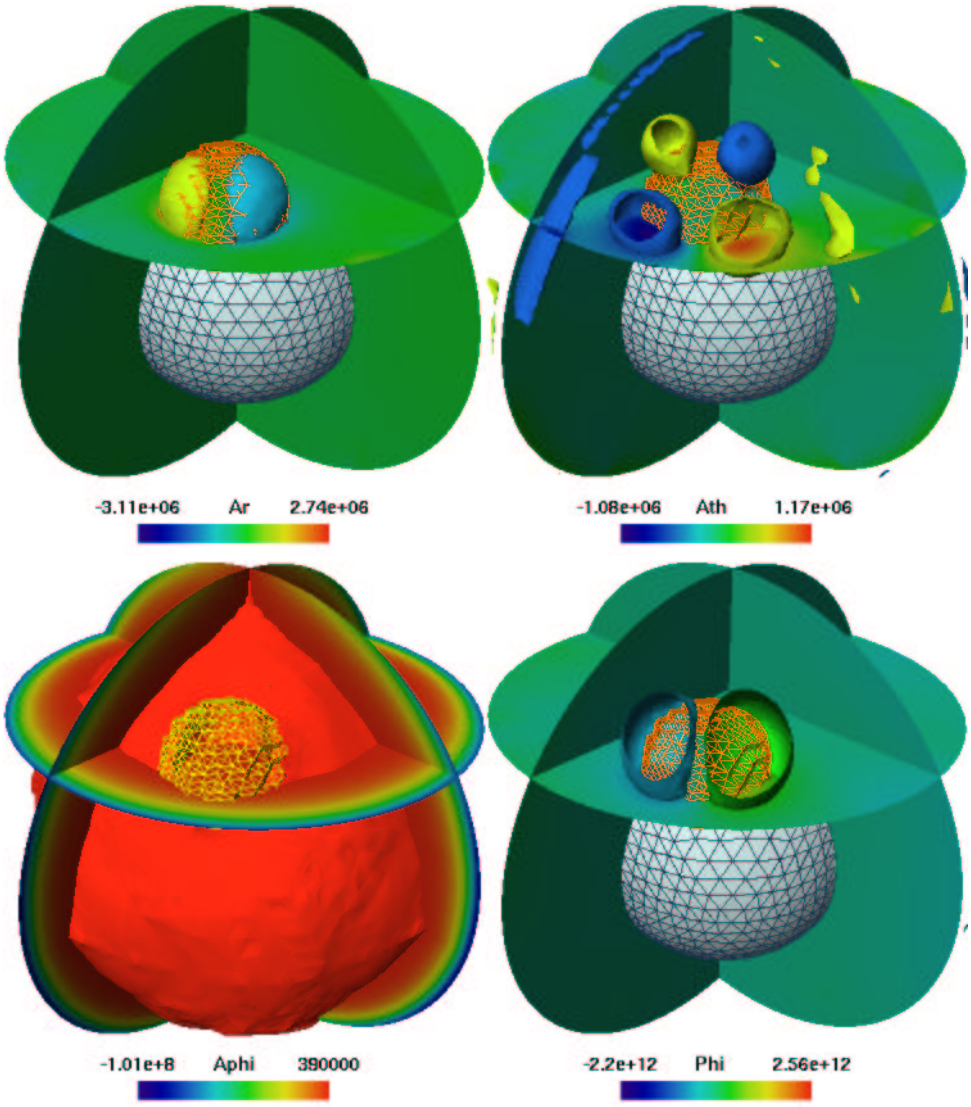

Figure 3.4: The high-resolution, 3-D finite element solution for nested spheres conductivity Model C excited by Load 2. Spherical components of vector magnetic potential $\boldsymbol{A}$ and scalar electrical potential Φ are shown at $t = 48\,\mathrm{h}$ after the onset of the storm model. The scales of $\boldsymbol{A}$ and Φ are in nA and $^{\mathrm{nV}}/_{\mathrm{s}}$, respectively. Boundaries of the core and spherical inclusion are outlined.

the mantle. The parameters of the model, as denoted in Figure 2.3, are $a = 6371\,\mathrm{km}$, $b = 1200\,\mathrm{km}$, $d = 5000\,\mathrm{km}$, $\vartheta_d = 40°$, $\varphi_d = 30°$, $\sigma_1 = 1\,^{\mathrm{S}}/_{\mathrm{m}}$, and $\sigma_2 = 10\,^{\mathrm{S}}/_{\mathrm{m}}$. The semi-analytical method does not allow to include another disjunctive sphere that would represent a highly conductive core. Nevertheless, the choice of highly conductive host sphere prevents the EM wave to penetrate down to the core and makes both methods

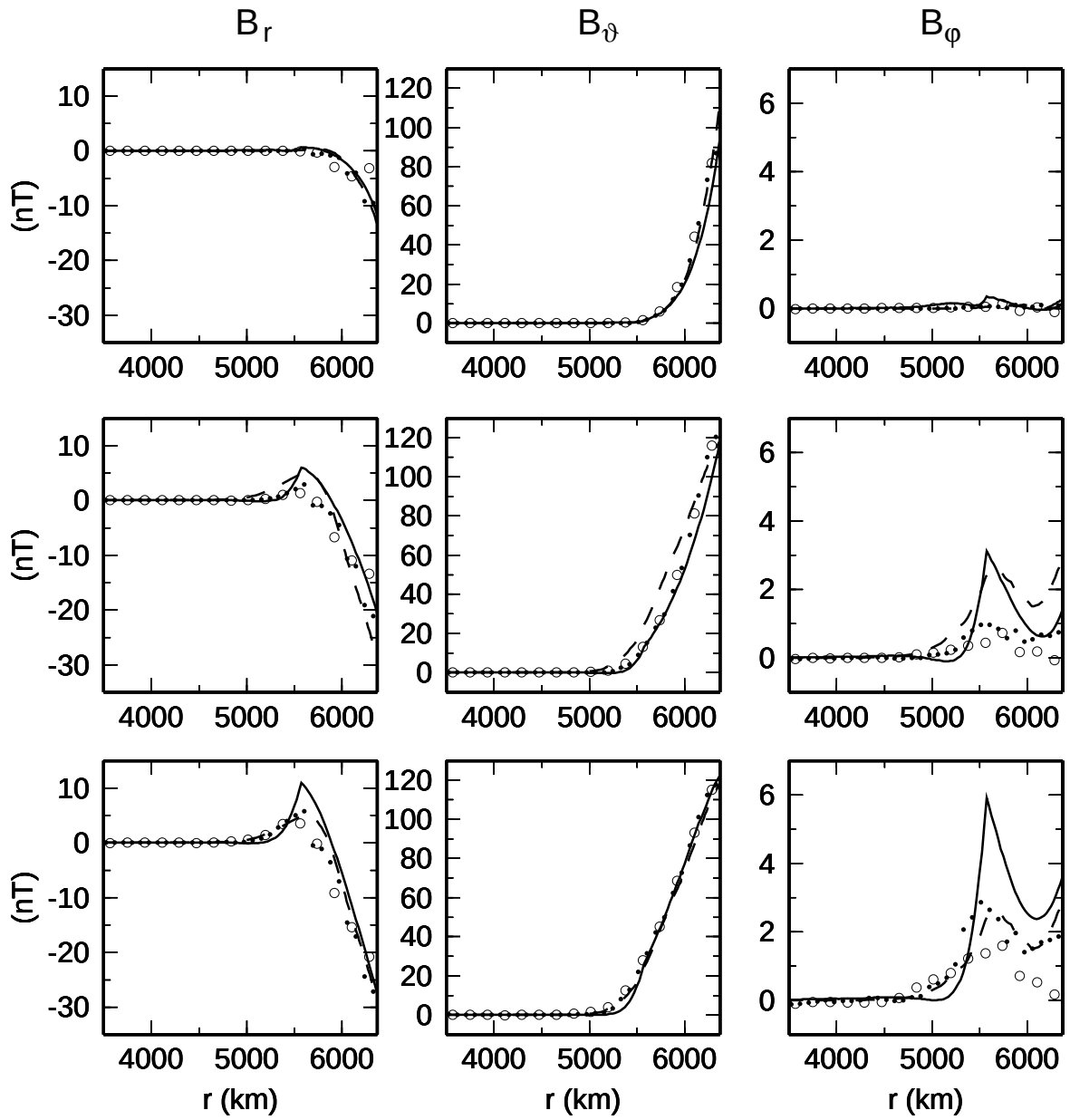

Figure 3.5: 3-D finite element solution for the nested spheres conductivity Model C excited by Load 2. The spherical components of $\boldsymbol{B}$ obtained by MLS fit are plotted along radius at fixed colatitude $\vartheta = 30°$ and longitude $\varphi = 45°$. Open circles and dots correspond to low-resolution mesh $M^r_{4,10}$ and high-resolution mesh $M^r_{5,20}$, respectively. For comparison, the semi-analytical solution and the solutions obtained by the spectral-finite element approach introduced in Chapter 2, are shown by solid and dashed lines, respectively. Top, middle, and bottom plates correspond to time levels 24, 48, and 72 h after the onset of the analytical storm model.

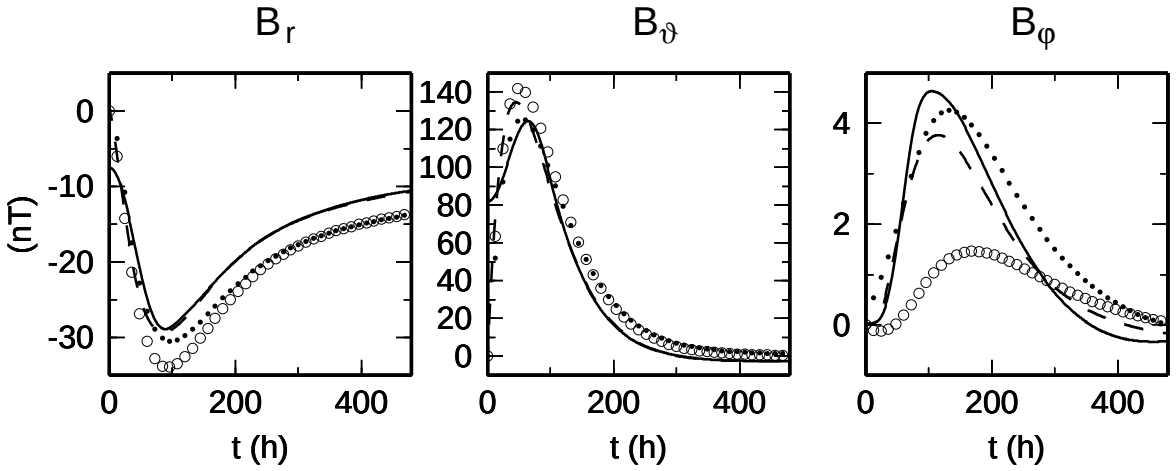

Figure 3.6: Same result as in Figure 3.5, but now we show the time evolution of $\boldsymbol{B}$ at the surface point $(\vartheta, \varphi) = (30°, 45°)$.

comparable.

The conductivity Model C is again excited by Load 2, the analytical approximation of a geomagnetic storm. The semi-analytical solution was computed for discrete frequencies from the interval 10^{-9}–10^{-4} rad/s, and transformed to the time-domain by the inverse Fourier transformation. The truncation degree of the spherical harmonic expansion varies

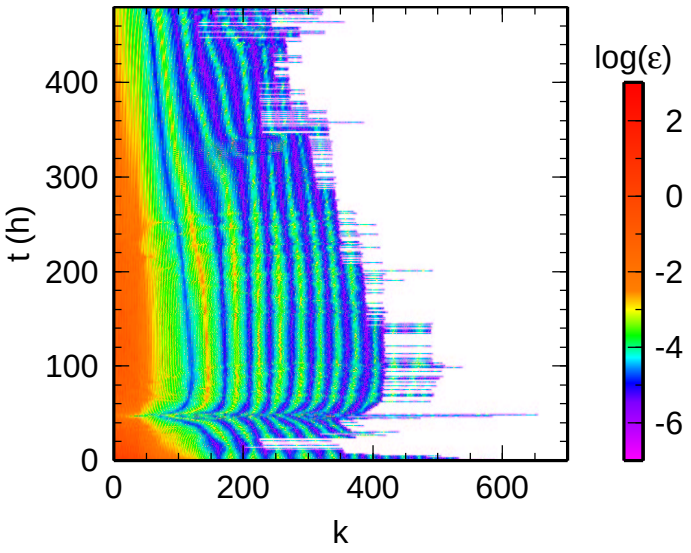

Figure 3.7: Rate of convergence of the preconditioned conjugate gradient solver for the high-resolution solution of the nested spheres model. Length of each horizontal line corresponds to the number of iterations of the method at given time level, while the residual norm ε is shown by colors.

from 12 to 24, according to the stability and accuracy criteria discussed in Section 2.2.1.

The 3-D finite element solution is found for two tetrahedral meshes, a low-resolution mesh $M^r_{4,10}$ and a high-resolution mesh $M^r_{5,20}$ (see Table C.1). Both meshes are locally refined inside the spherical inclusion and in its neighbourhood. The integration time step is 1 h. The magnetic induction vector $\boldsymbol{B}$ is obtained by a numerical differentiation of potential $\boldsymbol{A}$ using the Moving Least Squares (MLS) method described in Appendix E.

Figure 3.4 shows the snapshot of the solution at $t = 48$ h in terms of the potentials $\boldsymbol{A}$, Φ. The anomalies of A_r, A_ϑ, and Φ are observed near the spherical inclusion, and to a lesser extent near the Earth's surface, where the axial symmetry is also disturbed.

Figures 3.5 and 3.6 compare the spatial and temporal behaviour of the 3-D finite element solutions with the semi-analytical reference solution. We also display the response of Model C computed by the 3-D spectral-finite element method introduced in Chapter 2, at a high spatial resolution ($j_{max} = 40$, $P = 100$, $\Delta t = 1$ h). The results indicate that the low-resolution 3-D finite element solution is accurate in terms of B_r and B_ϑ components, but yields large discrepancies in the B_φ component. The accuracy of the high-resolution solution is comparable to that reached by the spectral-finite element approach.

Finally, Figure 3.7 shows the rate of convergence of the PCG method for the high-resolution 3-D finite element computation. As expected, the largest number of iterations per time step corresponds to the areas of steepest increase or descent of the inducing load.

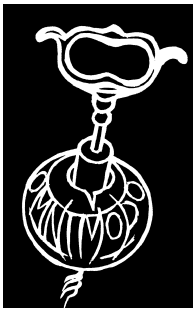

Chapter 4

The transient Dst induction signal at satellite altitudes

4.1 Introduction

In this chapter, we consider a realistic crust and upper-mantle conductivity model based on laboratory measurements and seismic tomography. This model is excited by a transient Dst signal taken from the period 1979–1980. Using the time-domain, spectral-finite element approach introduced in Chapter 2 we will study the sensitivity of the EM response observed at satellite altitudes to lateral conductivity variations in the upper mantle which are overlain by the near-surface conductivity inhomogeneities characterizing the ocean, continent and sea-shelf distribution.

4.2 Conductivity model

We construct a 3-D conductivity model based on three data sources. The contrasts between the highly conductive oceans water, resistive continents, and intermediate shelves and marine sediments are treated using the surface conductance map constructed by Everett et al. (2002). The conductance is converted to conductivity using a layer with constant thickness of 50 km (see Figure 4.1).

The conductivity in the upper and lower mantle is based on the 1-D conductivity model derived by Xu et al. (2000) from laboratory measurements, combined with the seismic tomography model SKS12WM13 by Liu & Dziewonski (1994). Although the shear-wave velocity and electrical conductivity have different sensitivity to various physical and chemical properties of the mantle, the positive correlation between the conductor depths and velocity perturbations obtained by Tarits (1994) supports the basic correspondence between the fast, cold, and resistive mantle contrasting to the slow, hot, and conductive areas.

Approximating the relation between electrical conductivity and shear-wave velocity variation δV by an exponential function, the conductivity σ at depth h, colatitude ϑ, and longitude φ is

$$\sigma(h,\vartheta,\varphi) = \sigma_0(h)\, f(h)^{-\frac{\delta V(h,\vartheta,\varphi)}{\delta V_M(h)-\delta V_m(h)}}, \tag{4.1}$$

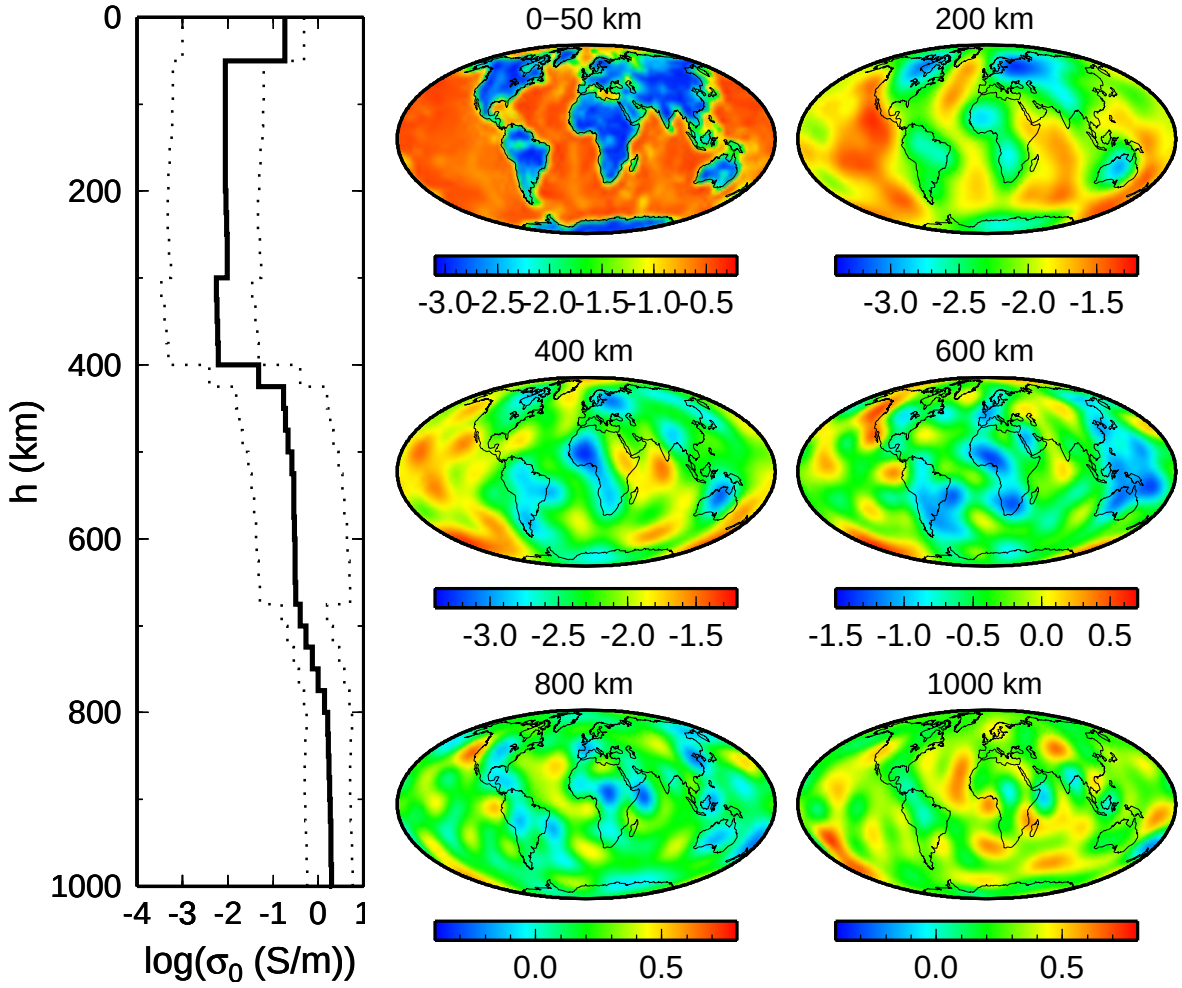

Figure 4.1: 3-D conductivity model in the crust, upper and mid-mantle. The solid line in the left panel shows the 1-D profile based on laboratory measurements (Xu et al., 2000). Lateral variations are confined to the interval shown by dotted lines. The first color map on the right shows the conductivity obtained from the surface conductance map for a uniform depth of 50 km. The following cross-sections sample the tomography-derived conductivity at depths of 200, 400, 600, 800, and 1000 km. All scale bars are in units of $\log(\sigma\ (^{\mathrm{S}}/_{\mathrm{m}}))$.

where $\delta V_M(h)$ and $\delta V_m(h)$ are respectively the maximum and minimum lateral seismic-velocity variations at depth h taken from SKS12WM13, and $\sigma_0(h)$ is the 1-D conductivity model by Xu et al. (2000). The base $f(h)$ which is the ratio of the maximum to minimum conductivity in each layer, is set to 100 in the upper mantle and to 10 in the lower mantle (Shankland et al., 1993). Finally, a homogeneous core with conductivity 10000 $^{\mathrm{S}}/_{\mathrm{m}}$ is assumed.

In order to evaluate the compatibility of the 3-D conductivity model with surface

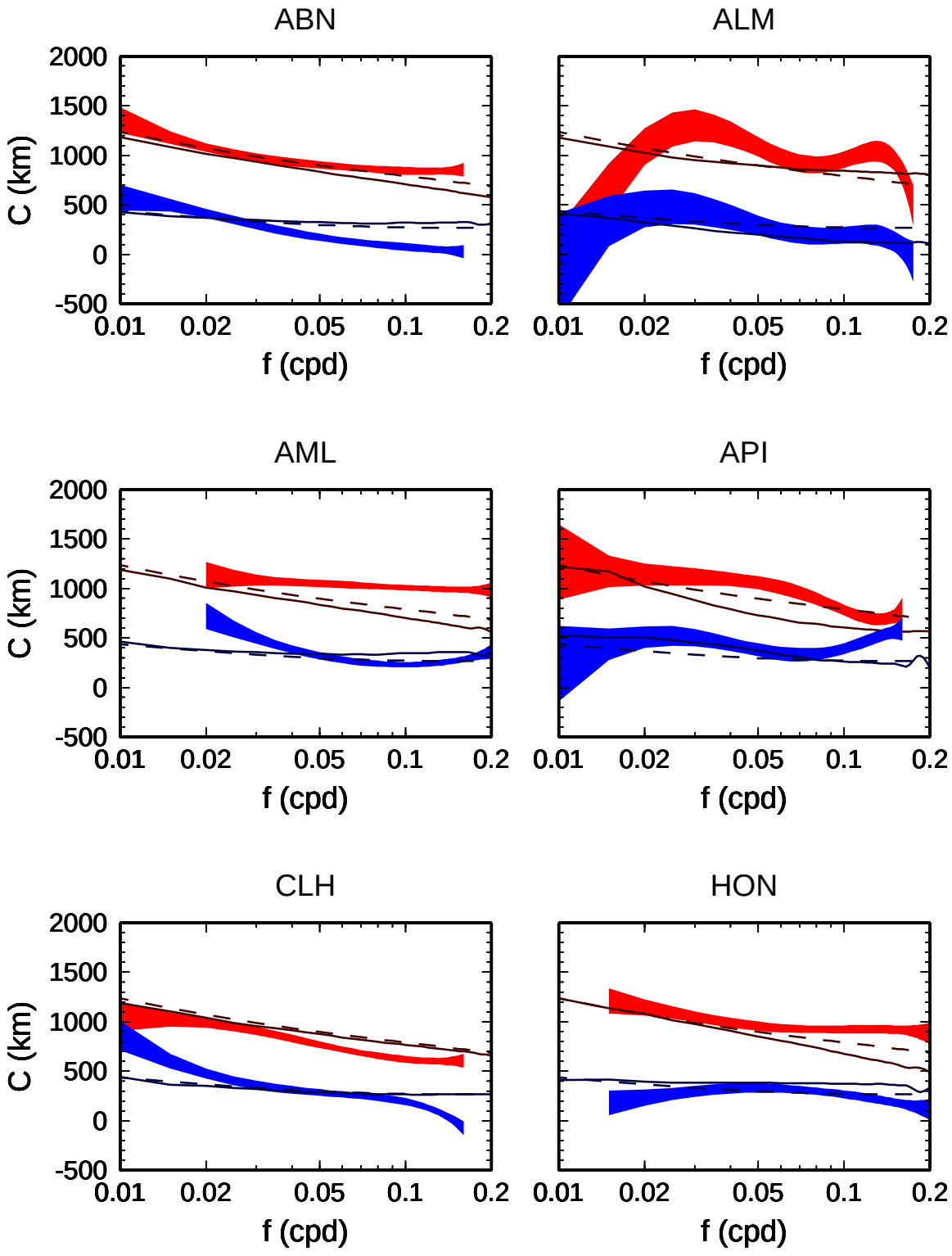
ABN
ALM
AML
API
CLH
HON
C (km)
f (cpd)
2000
1500
1000
500
0
-500
0.01
0.02
0.05
0.1
0.2

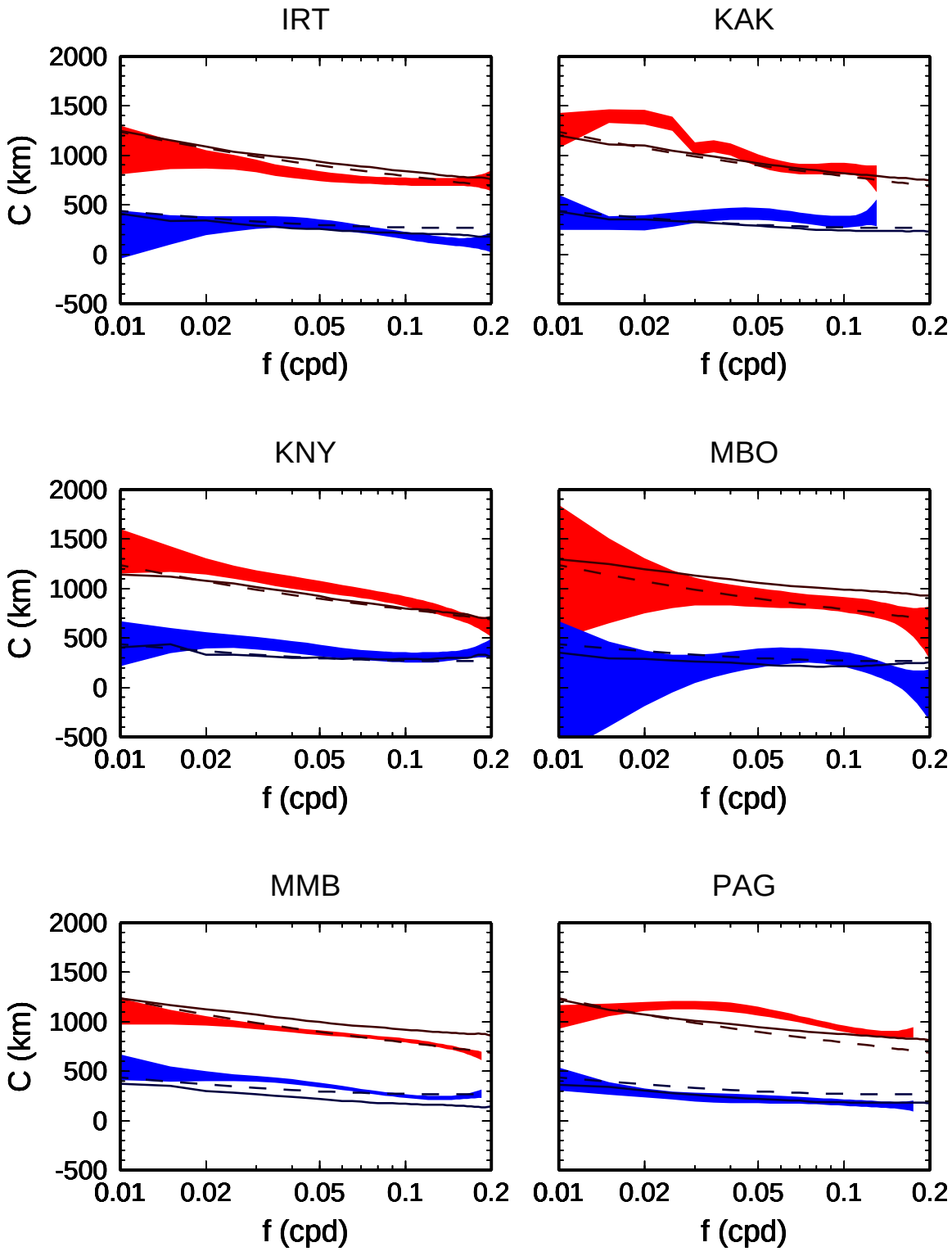
IRT
KAK
KNY
MBO
MMB
PAG
C (km)
2000
1500
1000
500
0
-500
0.01
0.02
0.05
0.1
0.2
f (cpd)

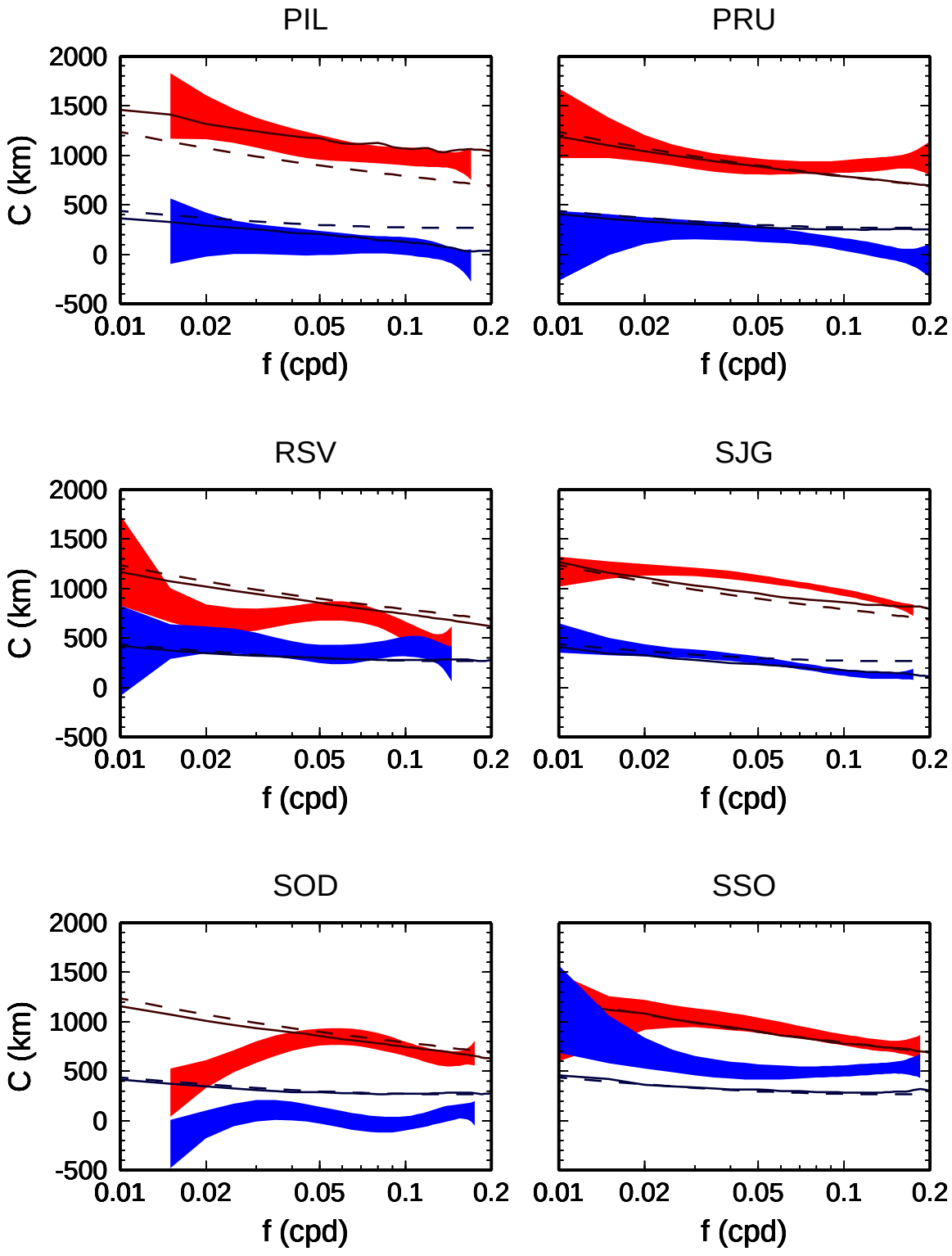
PIL
PRU
RSV
SJG
SOD
SSO
C (km)
f (cpd)
2000
1500
1000
500
0
-500
0.01
0.02
0.05
0.1
0.2

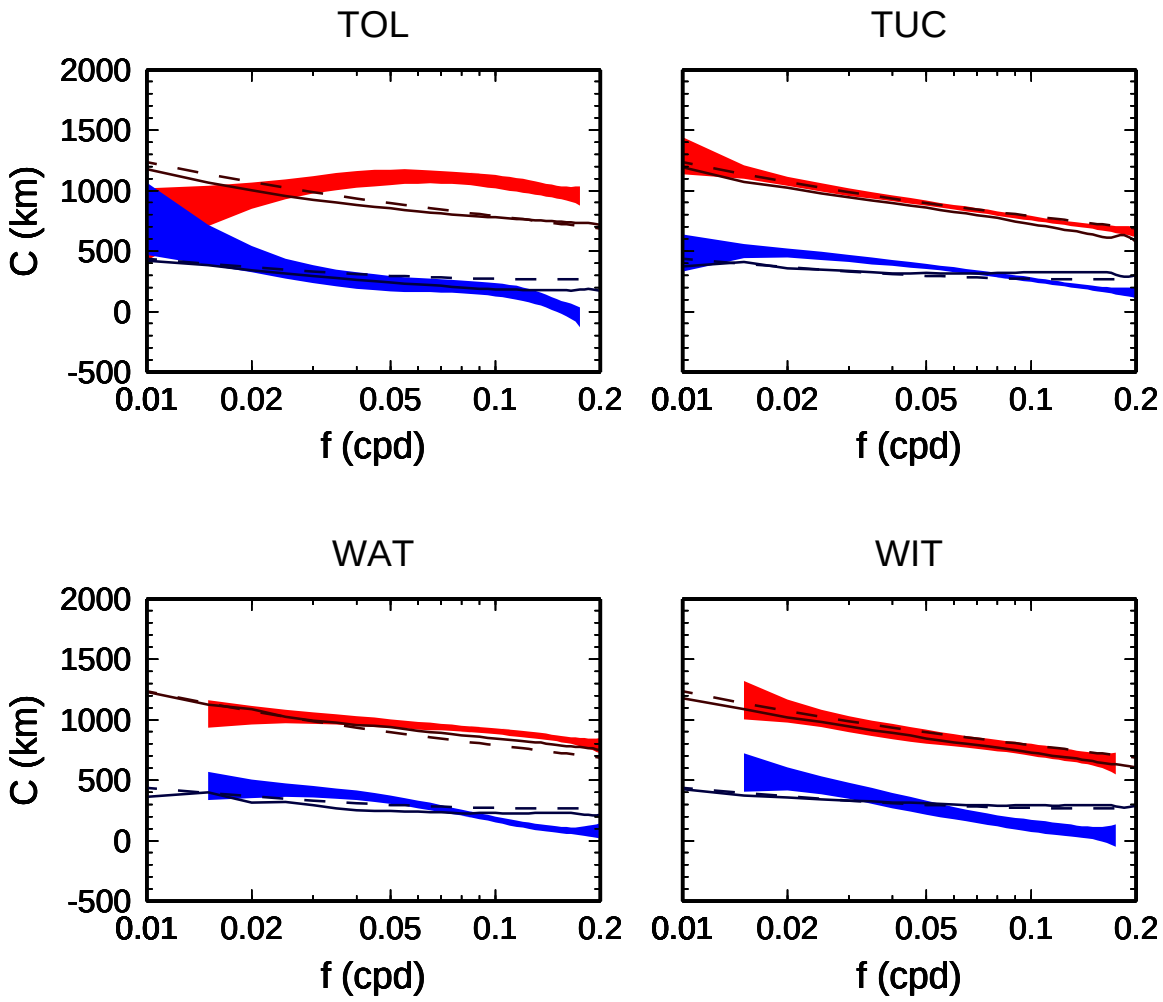

Figure 4.2: Comparison of the Schmucker C-responses generated by the 3-D conductivity model with realistic responses computed by Schultz & Larsen (1987) for 22 ground stations. Response of the 1-D conductivity model $\sigma_0(h)$ which is identical at all observatories is plotted by dashed lines, while the responses of the 3-D conductivity model are shown by solid lines. The observed observatory responses are confined within the one standard deviation error shown by color bands. Red, and blue colors correspond to Real(C) and $-$Imag(C), respectively.

geomagnetic data, the Schmucker C-responses,

$$C = \frac{a \, \tan\vartheta \, B_r}{2 \, B_\vartheta}, \tag{4.2}$$

are computed in the frequency range 0.01 to 0.2 cpd using the spectral-finite element code by Martinec (1999a). Figure 4.2 shows them compared with local 1-D responses from the

Station	Geomagnetic latitude	Geographic latitude	Geographic longitude	χ^2 misfit 1-D	χ^2 misfit 3-D
ABN	53.65	51.19	359.61	310.33	570.87
ALM	40.23	36.85	357.54	78.85	62.03
AML	−47.25	−43.15	172.72	696.78	1409.18
API	−15.69	−13.81	188.23	117.40	261.23
CLH	49.85	38.73	283.16	378.98	308.43
HON	21.41	21.32	201.94	150.09	520.40
IRT	41.30	52.46	104.04	97.22	99.59
KAK	26.44	36.23	140.19	102.96	102.52
KNY	20.93	31.42	130.88	71.40	55.42
MBO	20.80	14.39	343.04	17.92	67.60
MMB	34.44	43.91	144.19	77.27	830.06
PAG	40.60	42.52	24.18	385.67	112.98
PIL	−20.54	−31.67	296.12	131.51	19.03
PRU	49.61	49.99	14.55	136.75	120.08
RSV	55.56	55.84	12.46	88.64	62.69
SJG	29.54	18.38	293.88	434.86	153.28
SOD	63.62	67.37	26.65	223.28	200.20
SSO	23.45	33.58	135.94	191.18	167.04
TOL	43.48	39.88	355.95	336.32	315.25
TUC	40.47	32.25	249.17	151.94	345.32
WAT	−41.44	−30.32	115.88	404.71	193.02
WIT	53.82	52.81	6.67	111.01	132.07

Table 4.1: Misfit of the C-responses generated by the 1-D conductivity model $\sigma_0(h)$ (Xu et al., 2000), and by the 3-D conductivity model (4.1), respectively, with respect to the observatory values from the Schultz & Larsen (1987) dataset. Blue and red colors are respectively used where the introduction of lateral variations improves or deteriorates the fit of the data.

dataset by Schultz & Larsen (1987). The agreement between the synthetic and observed data at individual stations is highly variable with the χ^2 misfit ranging from 19.03 up to 1409.18 (see Table 4.1). Addition of the lateral conductivity variations according to (4.1) to the 1-D profile $\sigma_0(h)$ improved the fit to the observed C-responses at 13 stations. At the remaining 9 stations the misfit obtained for the 3-D model is larger than for the 1-D model. These results must be interpreted cautiously, since the 3-D conductivity model does not comply with the assumption of local 1-D structure used in the processing of local responses. Nevertheless, stacking over the computed and observed mid-latitude C-responses (see Figure 4.3), shows that the model has a degree of lateral heterogeneity appropriate to the observed responses, although the particular conductivity structures in

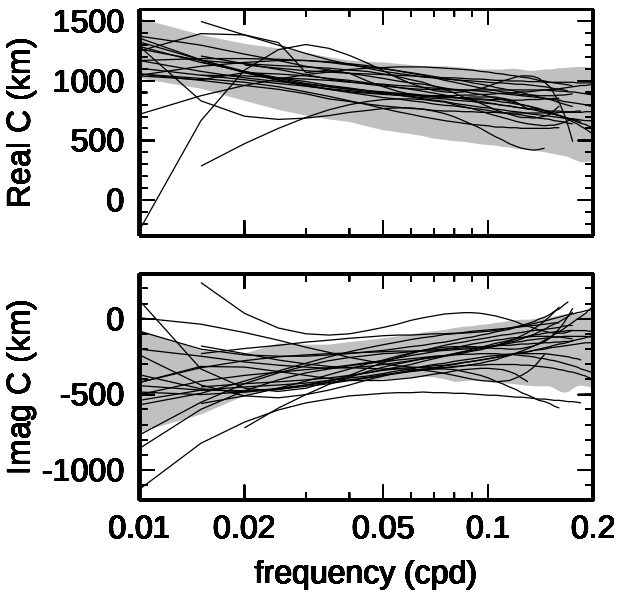

Figure 4.3: The Schmucker C-responses generated by the 3-D conductivity model. At middle geomagnetic latitudes, $25° \leq |\lambda_d| \leq 65°$, these are limited to the areas shown by grey shading. Local 1-D responses computed by Schultz & Larsen (1987) for 22 ground stations are stacked over using solid lines.

the model may differ from those required by the surface data.

4.3 Exciting field

We excite the conductivity model specified in the previous section by a transient, axisymmetric ring current. This is a first-order approximation of the spatial distribution of Dst

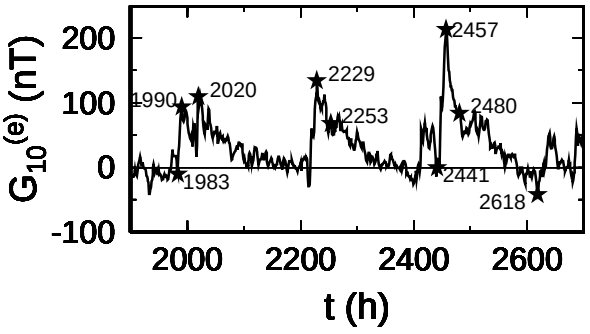

Figure 4.4: The coefficient $G_{10}^{(e)}$ of the external excitation field. Time $t = 0$ corresponds to Nov. 5, 1979, 0:00 UT, the displayed interval spans over three successive storms occurring between Jan. 24 and Feb. 27, 1980. Stars mark the epochs shown in Figures 4.5–4.7.

currents (Daglis & Kozyra, 2002). Assuming a P_{10} geometry for the exciting field in the geomagnetic coordinate system, the dipolar coefficient of the external magnetic potential $G_{10}^{(e)}$ can be derived from the Dst index (downloaded from the WDC-C2 Kyoto Dst index service, `http://swdcdb.kugi.kyoto-u.ac.jp/dstdir/`), by a simple scaling formula,

$$G_{10}^{(e)}(t) = -\sqrt{\frac{4\pi}{3}}\,\frac{Dst(t)}{1+Q_1}, \tag{4.3}$$

where $Q_1 = 0.27$ is the global estimate of the internal to external fields ratio (Langel & Estes, 1985).

Figure 4.4 shows the time evolution of $G_{10}^{(e)}$ during three successive magnetic storms in January and February, 1980. At this epoch the solution has already evolved for more than 1900 h to ensure that the presented results are not biased by the choice of initial value of the magnetic field, which is an inherent feature of the time-domain method.

4.4 Results

The time-domain response of the realistic 3-D conductivity model to the Dst excitation is computed using the spectral-finite element approach described in Chapter 2. The spherical harmonic expansion is truncated at $j_{max} = 40$, yielding an angular resolution of about 500 km at the Earth's surface. The radial discretization assumes layer thickness of 25 km throughout the mantle, and 200 km in the core, and the time-step is set to 1 h.

Figures (4.5–4.7) show the snapshots of the B_r, B_ϑ, and B_φ computed at 400 km altitude which is typical of low-orbit satellites. Note that the spherical components are related to the geomagnetic coordinate system. In the case of an azimuthally symmetric external excitation and a 1-D conductivity model, the longitudinal component B_φ vanishes. Therefore, B_φ shown in Figure (4.7) can be completely assigned to the effect of lateral conductivity variations. On the other hand, the B_r and B_ϑ components have predominantly dipolar shape with amplitudes reaching 50 nT, and 130 nT, respectively, at the peak of the most intense storm. About 50% of B_r, and 30% of B_ϑ at this altitude is of internal origin. In order to make the effect of lateral variations on B_r, and B_ϑ visible, both the internal, and external dipolar terms are subtracted from the solution in Figures 4.5 and 4.6.

The largest magnetic anomalies, up to 1.2 nT, 1.8 nT, and 2.1 nT in B_φ, and in non-dipolar parts of B_ϑ, B_r, respectively can be assigned to the resistive areas in the transition zone below South America, Africa, and the western Pacific. On the other hand, the signal due to the large positive anomaly at 200 km depth below the eastern Pacific is weaker. The induced field shows similar spatial structure for different storms with the largest amplitude corresponding to the most severe storm. This is not surprising, since the imposed inducing field has the same dipolar spatial structure all the time. Note

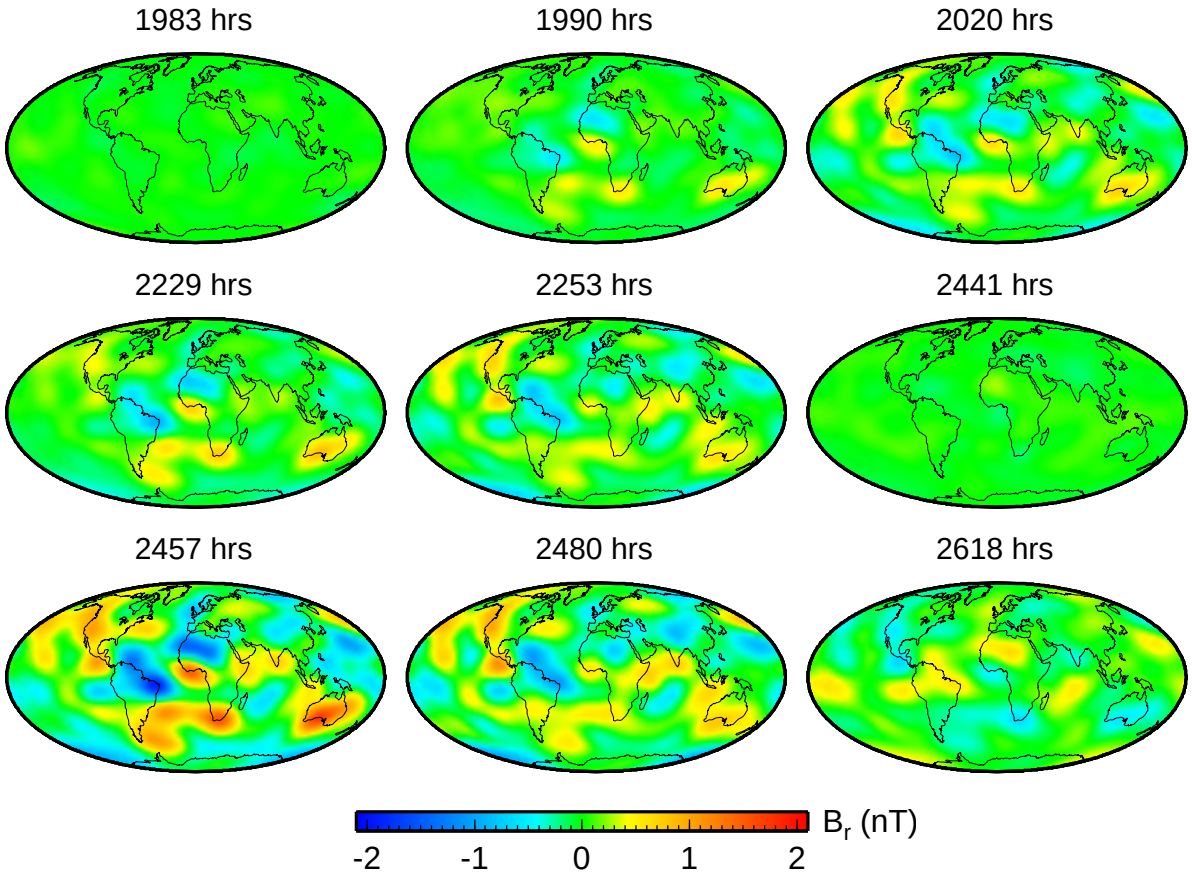

Figure 4.5: The computed B_r anomalies of the induced field at satellite altitude 400 km. Only non-dipolar part of the field is shown, the terms corresponding to the external excitation, and to the induced P_{10} field are not included. Snapshots at t = 1983, and 2441 h correspond to the onsets of the magnetic storms. At t = 1990, 2020, 2229, 2457 h the storms culminate, and t = 2253, 2480, and 2618 h sample the recovery phases. The time snapshots are marked in 4.4.

that in the last snapshots in Figures (4.5–4.7), the small positive Dst index (i.e., negative $G_{10}^{(e)}$) yields change of the sign also in the induced anomalous field.

4.5 Discussion

Our simulation shows that the EM response of the realistic conductivity model to intense transient changes in the ring-current system is detectable by a low-orbit satellite magnetometer. The magnitude of the signal induced by the highly heterogeneous oceanic/continental layer is less than 10% smaller than that of the mid-mantle conductivity heterogeneities. This is in agreement with the results of previous synthetic studies

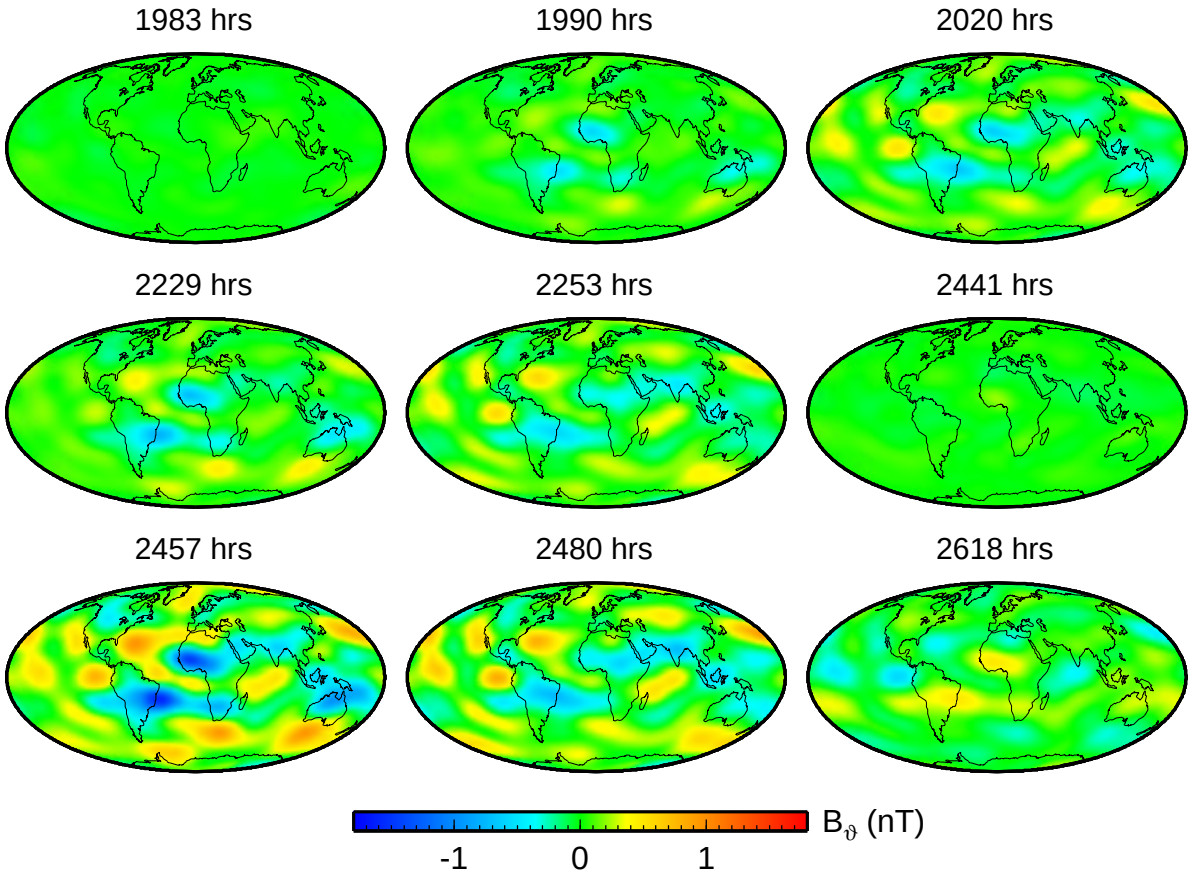

Figure 4.6: The computed B_ϑ anomalies of the induced field at satellite altitude 400 km. See also Figure 4.5 caption.

carried out in the frequency domain using surface observations (Weiss & Everett, 1998).

Since the period we covered coincides with the MAGSAT mission, direct comparison of the results is advisable. Constable et al. (manuscript, `http://mahi.ucsd.edu/Steve/MDAT/`, 2001) isolated the Dst signal from MAGSAT data, and showed that after fitting the P_{10} model for individual satellite passes, the RMS residuals are 5 to 6 nT for B_r, and B_ϑ components, and up to 11 nT in the B_φ component for the ascending passes of the spacecraft. These residuals represent, beside possible remnants of non-Dst signals, a combined effect of non-P_{10} external sources, and lateral conductivity variations. In order to distinguish between these two components and to interpret satellite magnetic data in terms of laterally varying conductivity models, a more accurate model of the temporal *and* spatial variations of the external excitation field will be necessary. The combination of satellite data from several satellites and land-based measurements should allow to go beyond the simple P_{10} excitation model. The time resolution needed to resolve rapid

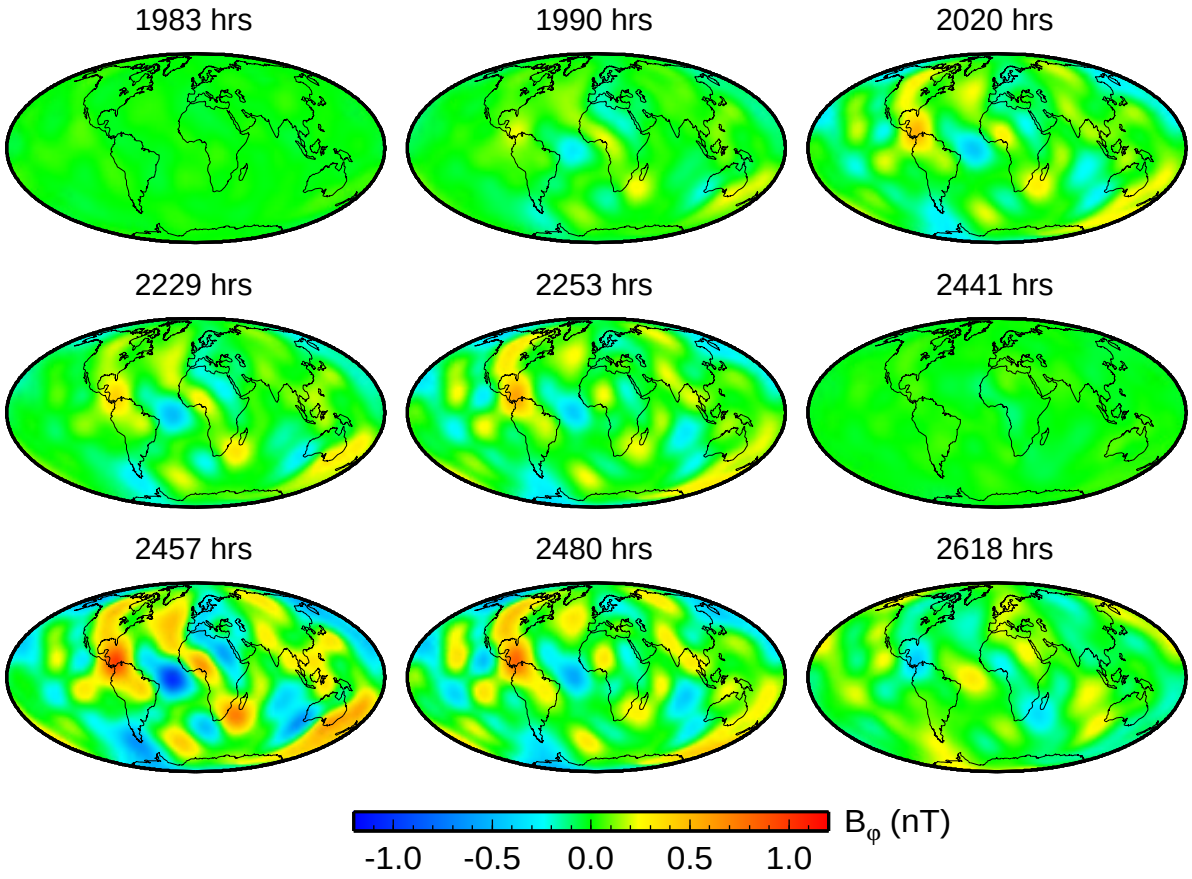

Figure 4.7: The computed B_φ anomalies of the induced field at satellite altitude 400 km. See also Figure 4.5 caption.

changes of the external field is of the order of a typical orbital period of a satellite ($\sim$ 1 h).

Chapter 5

Conclusions

The time-domain approaches to the problem of electromagnetic induction in the heterogeneous Earth's mantle presented in Chapters 2 and 3 represent alternative methods to the traditional frequency-domain techniques. Both approaches are able to compute the response of 3-D conductivity models to external excitation with complicated spatio-temporal characteristics. The methods have been numerically validated against semi-analytical solutions for nested spheres conductivity models and numerical 2-D axially symmetric solutions.

The spectral-finite element method described in Chapter 2 offers an efficient treatment of the boundary conditions at the Earth's surface based on the analytical expression for the magnetic potential in the atmosphere. Using equations (2.13–2.15), the magnetic field computed at the Earth's surface can be easily continued upwards to be compared with data recorded by satellite born magnetometers. Implicit treatment of the effect of 1-D spherically symmetric conductivity stabilizes the time-integration scheme, while the computationally demanding coupling due to the lateral conductivity variations is efficiently evaluated on the angular grid using the solution from the previous time step. The spectral-finite element spatial parameterization allows one to increase the radial resolution where necessary, e.g., in the lithosphere, or throughout the transition zone in the mantle. On the other hand, the angular resolution given by the truncation degree of the spherical harmonic expansion can be increased only globally. The time step has to be chosen cautiously with respect to the vigour of the time-variations of the inducing magnetospheric currents.

The 3-D finite element method introduced in Chapter 3 addresses the problem of non-uniform spatial distribution of ground geomagnetic observatories. Its main advantage over the spectral-finite element method is the versatility of the spatial discretization. Using the local refinement technique, the mesh can be adapted to yield high-resolution results for regions with good data coverage. On the other hand, the 3-D finite element formulation with a prescribed model of external inducing currents requires to compute the numerical solution of the Laplace equation in the insulating atmosphere, introducing an additional computational burden.

The speed of the 3-D finite element method depends on the rate of convergence of the PCG algorithm can be fasten up using a better preconditioner. This can be exploited in the inverse problem, where a complete LU decomposition can be computed for a reference

3-D conductivity model and used as a preconditioner for a set of forward problem runs.

The presented approaches to the problem of EM induction in the Earth's mantle are designed to be used as forward solvers in the global inversion of the satellite, or combined satellite and ground based data in the time-domain, to reveal the lateral conductivity heterogeneities in the mid-mantle. As a preliminary step, the spectral-finite element method was applied to compute the satellite altitude response of a realistic mantle conductivity model to a Dst transient signal (see Chapter 4). The results suggest that the signal due to the mid-mantle lateral conductivity variations induced by intense geomagnetic storms should be detectable at satellite altitudes.

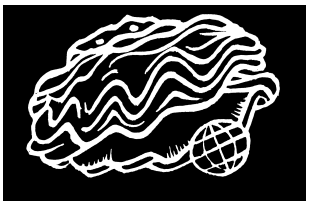

References

Anderson, E., Z. Bai, C. Bischof, S. Blackford, J. Dongara, J. Du Croz, A. Greenbaum, S. Hammarling, A. McKenney, & D. Sorensen, 1999. LAPACK User's Guide, Third edition, SIAM, Philadelphia, Pennsylvania.

Banks, R.J., 1969. Geomagnetic variations and the electrical conductivity of the upper mantle, *Geophys. J. R. astr. Soc., 17,* 457–418;2 87.

Biro, O. & K. Preis, 1989. On the use of the magnetic vector potential in the finite element analysis of three-dimensional eddy currents, *IEEE Trans. Magn., 25* 3145–3159.

Biro, O. & K. Preis, 1990. Finite element analysis of 3-D eddy currents, *IEEE Trans. Magn., 26* 418–423.

Daglis, I.A. & J.U. Kozyra, 2002. Outstanding issues of ring current dynamics, *Journal of Atmospheric and Solar-Terestrial Physics, 64,* 253–264.

Duffy, T.S. & R.J. Hemley, 1995. Some like it hot: The temperature structure of the Earth, *Rev. Geophys. Vol. 33 Suppl.,* American Geophysical Union.

Everett, M.E. & A. Schultz, 1995. Geomagnetic induction in eccentrically nested spheres, *Phys. Earth planet. Inter., 92,* 189–198.

Everett, M.E. & A. Schultz, 1996. Geomagnetic induction in a heterogeneous sphere: Azimuthally symmetric test computations and the response of an undulating 660-km discontinuity, *J. geophys. Res., 101, B2,* 2765–2783.

Everett, M.E., 1997. A three-dimensional spherical mesh generator, *Geophys. J. Int., 130,* 193–200.

Everett, M.E., S. Constable, & C.G. Constable. Effect of near-surface conductance on global satellite induction responses, *submitted to Geophys. J. Int.*

Fainberg, E.B., A.V. Kuvshinov, & B.Sh. Singer, 1990. Electromagnetic induction in a spherical earth with non-uniform oceans and continents in electric contact with the underlying medium — I. Theory, method and example, *Geophys. J. Int., 102,* 273–281.

Gossier, A., 2001. Moving least-squares: A numerical differentiation method for irregularly spaced calculation points, *Sandia report SAND2001-1669,* Albuquerque, New Mexico and Livermore, California.

Hamano, Y., 2002. A new time-domain approach for the electromagnetic induction problem in a three-dimensional heterogeneous earth, *Geophys. J. Int., 150,* 753–769.

IMSL Fortran subroutines for mathematical applications, 1994. Math library, Volumes 1 & 2, version 3.0, Visual Numerics, Inc., Houston, Texas.

Křížek, M. & P. Neittaanmäki, 1990. Finite Element Approximation of Variational Problems and Applications, Longman Scientific and Technical, Harlow, UK and Wiley, New York.

Kuvshinov, A.V. & O.V. Pankratov, 1994. Electromagnetic induction in a spherical Earth with inhomogeneous conducting mantle: thin sheet forward problem, in: *Proc. 12th workshop on electromagnetic induction in the Earth,* p. 53, Université de Bretagne Occidentale, Brest, France.

Lahiri, B. & A. Price, 1939. Electromagnetic induction in non-uniform conductors, and the determination of the conductivity of the Earth from terrestrial magnetic variations, *Phil. Trans. R. Soc. London, 237,* 509–540.

Langel, R.A. & R.H. Estes, 1985. Large-scale, near-field magnetic fields from external sources and the corresponding induced internal field, *Geophys. J. Int., 90,* 2487–2494.

Langel, R.A., 1987. The main field, in: *Geomagnetism, Volume 1,* ed. Jacobs J.A., Academic Press, London.

Langel, R.A., T.J. Sabaka, R.T. Baldwin, & J.A. Conrad, 1996. The near-Earth magnetic field from magnetospheric and quiet-day ionospheric sources and how it is modeled, *Phys. Earth planet. Inter., 98,* 235–267.

Liu, X.-F. & A.M. Dziewonski, 1994. Improved resolution of the lower-most mantle shear wave velocity structure obtained using SKS-S data, *EOS, Trans. Am. geophys. Un., 75, Spring Meet. Suppl.,* 232–234.

Liu, A. & B. Joe, 1996. Quality local refinement of tetrahedral meshes based on 8-subtetrahedron subdivision, *Math. Comp., 215* 1183-1200.

Martinec, Z., 1989. Program to calculate the spectral harmonic expansion coefficients of the two scalar fields product, *Computer Physics Communications, 54,* 177–182.

Martinec, Z., 1997. Spectral-finite element approach to two-dimensional electromagnetic induction in a spherical Earth, *Geophys. J. Int., 130,* 583–594.

Martinec, Z., 1998. Geomagnetic induction in multiple eccentrically nested spheres, *Geophys. J. Int., 132,* 96–110.

Martinec, Z., 1999. Spectral-finite element approach to three-dimensional electromagnetic induction in a spherical Earth, *Geophys. J. Int., 136,* 229–250.

Martinec, Z., 1999. Spectral, initial value approach for viscoelastic relaxation of a spherical earth with a three-dimensional viscosity — I. Theory, *Geophys. J. Int., 137,* 469–488.

Martinec, Z., M.E. Everett & J. Velímský, 2002. Time-domain, spectral-finite element approach to transient two-dimensional geomagnetic induction in a spherical heterogoeneous earth, *submitted to Geophys. J. Int.*

Nédelec, J.C., 1980. Mixed finite elements in $\mathbb{R}^3$, *Numer. Math. 35,* 315–341.

Olsen, N., 1998. The electrical conductivity of the mantle beneath Europe derived from C-responses from 3 to 720 hr, *Geophys. J. Int., 133,* 298–308.

Parkinson, W.D. & V.R.S. Hutton, 1989. The electrical conductivity of the Earth, in: *Geomagnetism, Volume 3,* ed. Jacobs J.A., Academic Press, London.

Petersons, H.F. & R.S. Anderssen, 1990. On the spherical symmetry of the electrical conductivity of the Earth's mantle, *J. Geomag. Geoelectr., 42,* 1309–1324.

Press, W.H., S.A. Teukolsky, W.T. Vetterling & B.P. Flannery, 1992. Numerical recipes in Fortran. The art of scientific computing, Cambridge University Press, Cambridge.

Press, W.H., S.A. Teukolsky, W.T. Vetterling & B.P. Flannery, 1996. Numerical recipes in Fortran 90. The art of parallel scientific computing, Cambridge University Press, Cambridge.

Price, A.T., 1930. Electromagnetic induction in a conducting sphere, *Proc. London Math. Soc., 51,* 217.

Rikitake, T., 1950. Electromagnetic induction within the Earth and its relation to the electrical state of the Earth's interior, *Bull. Earthq. Res. Inst., Tokyo Univ., 28,* 45–100.

Roberts, R.G., 1984. The long-period electromagnetic response of the Earth, *Geophys. J. R. astr. Soc., 78,* 547–572.

Schultz, A., 1990. On the vertical gradient and associated heterogeneity in mantle electrical conductivity. *Phys. Earth planet. Inter., 64,* 68–86.

Schultz, A. & J. Larsen, 1987. On the electrical conductivity of the mid mantle: I. Calculation of equivalent scalar magnetotelluric response functions, *Geophys. J. R. astr. Soc., 88,* 733–761.

Schultz, A. & J. Larsen, 1990. On the electrical conductivity of the mid mantle: II. Delineation of heterogeneity by application of extremal inverse solutions, *Geophys. J. Int., 101,* 565–580.

Semenov, V.Yu., 1998. Regional conductivity structures of the Earth's mantle, Publications of the Institute of Geophysics, Polish Academy of Sciences, Vol. C-65 (302), Warsaw.

Shankland T.J., J. Peyronneau, & J.P. Poirier, 1993. Electrical conductivity of the Earth's lower mantle, *Nature, 366,* 453–455.

Tarits, P., 1994. Electromagnetic studies of global geodynamic processes, *Surveys in Geophysics, 15,* 209–238.

Uyeshima, M. & A. Schultz, 2000. Geoelectromagnetic induction in a heterogeneous sphere: a new three-dimensional forward solver using a conservative staggered-grid finite difference method, *Geophys. J. Int., 140,* 636–650.

Varshalovich, D.A., A.N. Moskalev & V.K. Khersonskii, 1989. Quantum Theory of Angular Momentum, World Scientific, Singapore.

Velímský, J., M.E. Everett & Z. Marinec, 2003. The transient Dst electromagnetic induction signal at satellite altitudes for a realistic 3-D electrical conductivity in the crust and mantle, *Geophys. Res. Lett., in press.*

Weiss, C.J. & M.E. Everett, 1998. Geomagnetic induction in a heterogeneous sphere: Fully three-dimensional test computations and the response of a realistic distribution of oceans and continents, *Geophys. J. Int., 135,* 650–662.

Xu, Y., B.T. Poe, T.J. Shankland, & D.C. Rubie, 1998. Electrical conductivity of olivine, wadsleyite, and ringwoodite under upper-mantle conditions. *Science, 280,* 1415–1418.

Xu, Y., T.J. Shankland, & B.T. Poe, 2000. Laboratory-based electrical conductivity in the Earth's mantle. *J. geophys. Res., 105(B12),* 27,865–27,875.

Yoshimura, R. & N. Oshiman, 2002. Edge-based finite element approach to the simulation of geolectromagnetic induction in a 3-D sphere, *Geophys. Res. Lett., 29,* No. 3, 9-1–9-4.

Zhang, T.S. & A. Schultz, 1992. A 3-D perturbation solution for the EM induction problem in a spherical earth — the forward problem, *Geophys. J. Int., 111,* 319–334.

Appendix A

Spherical harmonic functions

This appendix summarizes the definitions of the scalar and vector spherical harmonic functions which are used in Chapter 2, including normalization, derivatives, and separation of radial and angular components.

We expand scalar functions into series of fully normalized scalar spherical harmonic functions Y_{jm} (Varshalovich et al., 1989),

$$Y_{jm}(\Omega) = \sqrt{\frac{2j+1}{4\pi}\,\frac{(j-m)!}{(j+m)!}}\,P_j^m(\cos\vartheta)\,e^{im\varphi} = P_{jm}(\cos\vartheta)\,e^{im\varphi}, \tag{A 1}$$

where $P_{jm}(\cos\vartheta)$ is the normalized form of associated Legendre polynomials $P_j^m(\cos\vartheta)$. The spherical harmonic functions are orthonormal on a unit sphere,

$$\int_\Omega \overline{Y}_{jm}(\Omega)\cdot Y_{j'm'}(\Omega)\,d\Omega \;=\; \delta_{jj'}\,\delta_{mm'},$$

and are eigenfunctions of the angular part of the the Laplace operator,

$$\left[\frac{1}{\sin\vartheta}\frac{\partial}{\partial\vartheta}\left(\sin\vartheta\,\frac{\partial}{\partial\vartheta}\right) + \frac{1}{\sin^2\vartheta}\frac{\partial^2}{\partial\varphi^2}\right] Y_{jm}(\Omega) = -j(j+1)Y_{jm}(\Omega). \tag{A 2}$$

Similarly, vector functions can be expanded into series of vector spherical harmonics. From several different sets of orthogonal vector spherical harmonic functions, we prefer the one used by Martinec (1999b),

$$\left\{\boldsymbol{S}_{jm}^{(\lambda)}(\Omega)\,|\,j=0,\ldots,\infty,\,m=-j,\ldots,j,\,\lambda=-1,0,1\right\}, \tag{A 3}$$

where

$$\boldsymbol{S}_{jm}^{(0)}(\Omega) \;=\; \boldsymbol{e}_r\times\operatorname{grad}_\Omega Y_{jm}(\Omega) = \left[\frac{\partial Y_{jm}(\Omega)}{\partial\vartheta}\,\boldsymbol{e}_\varphi - \frac{1}{\sin\vartheta}\,\frac{\partial Y_{jm}(\Omega)}{\partial\varphi}\,\boldsymbol{e}_\vartheta\right], \tag{A 4}$$

$$\boldsymbol{S}_{jm}^{(-1)}(\Omega) \;=\; Y_{jm}(\Omega)\,\boldsymbol{e}_r, \tag{A 5}$$

$$\boldsymbol{S}_{jm}^{(1)}(\Omega) \;=\; \operatorname{grad}_\Omega Y_{jm}(\Omega) = \left[\frac{\partial Y_{jm}(\Omega)}{\partial\vartheta}\,\boldsymbol{e}_\vartheta + \frac{1}{\sin\vartheta}\,\frac{\partial Y_{jm}(\Omega)}{\partial\varphi}\,\boldsymbol{e}_\varphi\right]. \tag{A 6}$$

The angular part of the gradient operator is

$$\mathrm{grad}_{\,\Omega} = \boldsymbol{e}_\vartheta \frac{\partial}{\partial \vartheta} + \boldsymbol{e}_\varphi \frac{1}{\sin\vartheta} \frac{\partial}{\partial \varphi}, \tag{A 7}$$

and $\boldsymbol{e}_r$, $\boldsymbol{e}_\vartheta$, and $\boldsymbol{e}_\varphi$ denote unit vectors corresponding to the radial coordinate r, colatitude ϑ, and longitude φ, respectively. Functions $\boldsymbol{S}^{(0)}_{jm}(\Omega)$ are toroidal, functions $\boldsymbol{S}^{(-1)}_{jm}(\Omega)$ and $\boldsymbol{S}^{(1)}_{jm}(\Omega)$ represent the radial and angular component of the spheroidal part of the expanded field, respectively. Although $\boldsymbol{S}^{(\lambda)}_{jm}(\Omega)$ are not eigenfunction of the Laplace operator, separation of the radial component generally simplifies the evaluation of coupling in problems with laterally varying parameters. Functions $\boldsymbol{S}^{(\lambda)}_{jm}(\Omega)$ are orthogonal on a unit sphere, i.e.,

$$\int_\Omega \overline{\boldsymbol{S}}^{(\lambda)}_{jm}(\Omega) \cdot \boldsymbol{S}^{(\lambda')}_{j'm'}(\Omega)\, d\Omega \;=\; N_{j\lambda}\delta_{jj'}\,\delta_{mm'}\,\delta_{\lambda\lambda'}, \tag{A 8}$$

with the norm

$$N_{j\lambda} = (1-\delta_{-1\,\lambda})\,\Pi_j + \delta_{-1\,\lambda}, \tag{A 9}$$

$$\Pi_j = j(j+1). \tag{A 10}$$

Since the Maxwell equations do not admit the existence of magnetic monopoles, the zeroth order spherical harmonic functions $Y_{00}(\Omega)$ and $\boldsymbol{S}^{(\lambda)}_{00}(\Omega)$ are excluded from the parameterizations of the scalar magnetic potential (2.10–2.12) and magnetic induction vector (2.19), respectively.

From definitions (A 4–A 6) the following relations can be easily derived,

$$\boldsymbol{S}^{(\lambda)}_{j\,-m}(\Omega) = (-1)^m\, \overline{\boldsymbol{S}}^{(\lambda)}_{jm}(\Omega), \tag{A 11}$$

$$\boldsymbol{e}_r \times \boldsymbol{S}^{(0)}_{jm}(\Omega) = -\boldsymbol{S}^{(1)}_{jm}(\Omega), \tag{A 12}$$

$$\boldsymbol{e}_r \times \boldsymbol{S}^{(-1)}_{jm}(\Omega) = 0, \tag{A 13}$$

$$\boldsymbol{e}_r \times \boldsymbol{S}^{(1)}_{jm}(\Omega) = \boldsymbol{S}^{(0)}_{jm}(\Omega), \tag{A 14}$$

$$\mathrm{grad}\,[f(r)\,Y_{jm}(\Omega)] = \frac{df(r)}{dr}\,\boldsymbol{S}^{(-1)}_{jm}(\Omega) + \frac{f(r)}{r}\,\boldsymbol{S}^{(1)}_{jm}(\Omega), \tag{A 15}$$

$$\mathrm{curl}\,\Big[f(r)\,\boldsymbol{S}^{(0)}_{jm}(\Omega)\Big] = -\Pi_j\,\frac{f(r)}{r}\,\boldsymbol{S}^{(-1)}_{jm}(\Omega) - \left(\frac{d}{dr}+\frac{1}{r}\right) f(r)\,\boldsymbol{S}^{(1)}_{jm}(\Omega), \tag{A 16}$$

$$\mathrm{curl}\,\Big[f(r)\,\boldsymbol{S}^{(-1)}_{jm}(\Omega)\Big] = -\frac{f(r)}{r}\,\boldsymbol{S}^{(0)}_{jm}(\Omega), \tag{A 17}$$

$$\mathrm{curl}\,\Big[f(r)\,\boldsymbol{S}^{(1)}_{jm}(\Omega)\Big] = \left(\frac{d}{dr}+\frac{1}{r}\right) f(r)\,\boldsymbol{S}^{(0)}_{jm}(\Omega), \tag{A 18}$$

$$\text{div}\left[f(r)\,\boldsymbol{S}_{jm}^{(0)}(\Omega)\right] = 0, \tag{A 19}$$

$$\text{div}\left[f(r)\,\boldsymbol{S}_{jm}^{(-1)}(\Omega)\right] = \left(\frac{d}{dr}+\frac{2}{r}\right) f(r)\,Y_{jm}(\Omega), \tag{A 20}$$

$$\text{div}\left[f(r)\,\boldsymbol{S}_{jm}^{(1)}(\Omega)\right] = -\Pi_j\,\frac{f(r)}{r}Y_{jm}(\Omega). \tag{A 21}$$

By $f(r)$ we mean an arbitrary continuous function of radius r.

Appendix B

Existence and uniqueness of the integral solution

Here we prove the existence and uniqueness of the time discretized, weak formulation of the electromagnetic induction problem (2.51–2.53). The boundary conditions imposed on the external part of the field at the surface are not common in the variational formulations of electromagnetic problems, since they cannot be expressed without the use of the spherical harmonic parameterization. Therefore first we reformulate the problem as a standard Dirichlet boundary value problem (DBVP) and then we show that it is equivalent to the formulation (2.51–2.53) which is more suitable for the realistic configuration of the Earth and its surroundings.

Find ${}^{i+1}\boldsymbol{b} \in H_{\mathrm{curl},0}\ \forall\, i = 0, 1, \ldots$, such that

$$\frac{\mu_0}{\Delta t}\left({}^{i+1}\boldsymbol{b}, \delta\boldsymbol{B}\right) + a_0({}^{i+1}\boldsymbol{b}, \delta\boldsymbol{B}) = \frac{\mu_0}{\Delta t}\left({}^{i}\boldsymbol{B} - {}^{i+1}\hat{\boldsymbol{B}}, \delta\boldsymbol{B}\right) - a_1({}^{i}\boldsymbol{B}, \delta\boldsymbol{B}) - a_0({}^{i+1}\hat{\boldsymbol{B}}, \delta\boldsymbol{B}) \quad \forall\, \delta\boldsymbol{B} \in H_{\mathrm{curl},0}, \tag{B 1}$$

where ${}^{i+1}\hat{\boldsymbol{B}}$ is an arbitrary function from H_{curl}, such that

$$\boldsymbol{e}_r \times {}^{i+1}\hat{\boldsymbol{B}} = -\boldsymbol{e}_r \times \operatorname{grad} U(t_{i+1}) \quad \text{on } \partial G. \tag{B 2}$$

Then ${}^{i+1}\boldsymbol{B} = {}^{i+1}\hat{\boldsymbol{B}} + {}^{i+1}\boldsymbol{b}$ is the solution of the time discretized DBVP.

Note that the solution ${}^{i+1}\boldsymbol{B}$ is separated in two parts, the function ${}^{i+1}\hat{\boldsymbol{B}}$ is constructed from the horizontal component of the total field at the surface and a homogeneous Dirichlet boundary condition is imposed on ${}^{i+1}\boldsymbol{b}$. Unlike in the formulation (2.51–2.53), the unknown function ${}^{i+1}\boldsymbol{b}$ and the test functions $\delta\boldsymbol{B}$ are from the same functional space $H_{\mathrm{curl},0}$ in DBVP.

It is elementary to prove that the DBVP satisfies the prerequisites of the Lax-Milgram theorem (Křížek & Neittaanmäki, 1990), i.e. that the form on the left hand side of (B 1) is sesquilinear, continuous, and H_{curl}-elliptic, and the right hand side is a linear functional with respect to $\delta\boldsymbol{B}$. Reminding the definitions of H_{curl}-scalar product $(\cdot,\cdot)_{H_{\mathrm{curl}}}$ and norm

$||\cdot||_{H_{\mathrm{curl}}}$ from F.2, we show the continuity,

$$\left|\frac{\mu_0}{\Delta t}\left({}^{i+1}\boldsymbol{b},\delta\boldsymbol{B}\right)+a_0({}^{i+1}\boldsymbol{b},\delta\boldsymbol{B})\right|\leq\alpha_1\left|\left({}^{i+1}\boldsymbol{b},\delta\boldsymbol{B}\right)_{H_{\mathrm{curl}}}\right|\leq\alpha_1\,||{}^{i+1}\boldsymbol{b}||_{H_{\mathrm{curl}}}\,||\delta\boldsymbol{B}||_{H_{\mathrm{curl}}},\quad\text{(B 3)}$$

and the H_{curl}-ellipticity of the left hand side.

$$\frac{\mu_0}{\Delta t}\left({}^{i+1}\boldsymbol{b},{}^{i+1}\boldsymbol{b}\right)+a_0({}^{i+1}\boldsymbol{b},{}^{i+1}\boldsymbol{b})\geq\alpha_2||{}^{i+1}\boldsymbol{b}||^2_{H_{\mathrm{curl}}},\quad\text{(B 4)}$$

Positive constants are denoted by α_k. Here we have to note that since ρ_0 is spherically symmetric, it is possible to prove the ellipticity of the form with respect to the norm of the Sobolev space $W^{1,2}(G)^3$. This is possible even in the case of azimuthally symmetric resistivity (Martinec, 1997), but not generally. Continuity of the functional on the right hand side of equation (B 1) is evident from the inequality

$$\begin{aligned}\left|\frac{\mu_0}{\Delta t}\left({}^{i}\boldsymbol{B}-{}^{i+1}\hat{\boldsymbol{B}},\delta\boldsymbol{B}\right)\right.&-a_1({}^{i}\boldsymbol{B},\delta\boldsymbol{B})-\\ \left.-a_0({}^{i+1}\hat{\boldsymbol{B}},\delta\boldsymbol{B})\right|&\leq\left(\alpha_3||{}^{i}\boldsymbol{B}||_{H_{\mathrm{curl}}}+\alpha_4||{}^{i+1}\hat{\boldsymbol{B}}||_{H_{\mathrm{curl}}}\right)||\delta\boldsymbol{B}||_{H_{\mathrm{curl}}}.\quad\text{(B 5)}\end{aligned}$$

Since the choice of ${}^{i+1}\hat{\boldsymbol{B}}$ is not unique, it remains to prove that the solution of (B 1) does not depend on ${}^{i+1}\hat{\boldsymbol{B}}$. Let ${}^{i+1}\hat{\boldsymbol{B}}_1$ and ${}^{i+1}\hat{\boldsymbol{B}}_2$ be two different functions from H_{curl}, satisfying the same boundary condition (B 2). Let ${}^{i+1}\boldsymbol{b}_1$ and ${}^{i+1}\boldsymbol{b}_2$ be the solutions of (B 1), corresponding to ${}^{i+1}\hat{\boldsymbol{B}}_1$ and ${}^{i+1}\hat{\boldsymbol{B}}_2$, respectively, and $\boldsymbol{B}_l={}^{i+1}\hat{\boldsymbol{B}}_l+{}^{i+1}\boldsymbol{b}_l$ be the solutions of DBVP for $l=1,2$. Then we can use a particular test function,

$$\delta\boldsymbol{B}={}^{i+1}\boldsymbol{B}_2-{}^{i+1}\boldsymbol{B}_1,\quad\delta\boldsymbol{B}\in H_{\mathrm{curl},0}.\quad\text{(B 6)}$$

Substituting (B 6) into (B 1) and subtracting the two equations (B 1) for $l=2,1$ yields,

$$\frac{\mu_0}{\Delta t}\left({}^{i+1}\boldsymbol{B}_2-{}^{i+1}\boldsymbol{B}_1,{}^{i+1}\boldsymbol{B}_2-{}^{i+1}\boldsymbol{B}_1\right)+a_0({}^{i+1}\boldsymbol{B}_2-{}^{i+1}\boldsymbol{B}_1,{}^{i+1}\boldsymbol{B}_2-{}^{i+1}\boldsymbol{B}_1)=0.\quad\text{(B 7)}$$

Because of the continuity of the form $\mu_0/\Delta t\,(\cdot,\cdot)+a_0\,(\cdot,\cdot)$ proved above, this can be satisfied if, and only if,

$$||{}^{i+1}\boldsymbol{B}_2-{}^{i+1}\boldsymbol{B}_1||_{H_{\mathrm{curl}}}=0\quad\text{(B 8)}$$

which implies,

$${}^{i+1}\boldsymbol{B}_1={}^{i+1}\boldsymbol{B}_2.\quad\text{(B 9)}$$

We have proved that for ${}^{i}\boldsymbol{B}$ known from the previous time-step and for the boundary condition $\boldsymbol{e}_r\times\mathrm{grad}\,U(t_{i+1})$ there exists a unique solution ${}^{i+1}\boldsymbol{B}$ of the DBVP (B 1).

The Dirichlet boundary condition (B 2) is represented in the spherical harmonic parameterization by equations (2.21) and (2.23) which prescribe the horizontal component

of $\boldsymbol{B}$ on ∂G. The vertical component of the magnetic induction vector on ∂G, as described by equation (2.22), is obtained as a part of the unique solution of the DBVP. The boundary conditions (2.24–2.25) have been introduced as a linear combination of (2.22–2.23). Therefore, the Galerkin system of linear equations (2.103) corresponding to problem (2.51–2.53) and the Galerkin system corresponding to the DBVP (B 1–B 2), and constructed by means of the spherical harmonic-finite element parameterization, are equivalent. One can be derived from the other by replacing particular rows by their linear combinations. The formulation (2.51–2.53) which prescribes the potential of the external field at the boundary, is equivalent to the Dirichlet formulation (B 1–B 2).

Appendix C

Tetrahedral mesh

The time-domain, 3-D finite-element EM induction solver that was introduced in Chapter 3 is to a certain extent independent on the choice of the discretization of the computational domain. Any conforming tetrahedral mesh which discretizes the Earth's mantle G and its insulating surroundings A can be employed, providing that it also approximates the three spherical surfaces, i.e., the core-mantle boundary, the mantle-atmosphere boundary, and the outer boundary, with sufficient accuracy. However, the quality of the mesh has great influence on the stability and convergence of the iterative matrix inversion schemes and on the accuracy of the solution. Everett (1997) suggested a high-quality tetrahedral mesh generator designed in particular for geophysical problems in spherical geometry. Here we briefly summarize his method and introduce two additional features that we employ in the presented validation of the FE EM induction solver. Firstly, the core is removed from the computational domain and the core-mantle boundary is created and suitably approximated. Secondly, local refinement which increases the resolution of the method in areas of particular interest is introduced.

Two different algorithms are used to generate the interior mesh that discretizes G, $a_{CMB} \leq r \leq a$ and the exterior mesh that discretizes A, $a \leq r \leq a_O$. The interior mesh generator is based on the algorithm of recursive subdivision of a tetrahedron $ABCD$ into eight subtetrahedra (Liu & Joe, 1996) which is shown in the left panel of Figure C 1. New vertices, E, F, G, H, I, and J are added in the midpoints of the edges AB, AC, AD, BC, BD, and CD, respectively. Four subtetrahedra, $AEFG$, $BEHI$, $CFHJ$, and $DGIJ$ are created at the corners. The remaining central octahedron $EFGHIJ$ is then divided into four subtetrahedra by addition of one edge. From the three possible choices, EJ, FI, and GH such edge is selected that yields the best quality of resulting subtetrahedra. The quality is measured by a coefficient Q (Liu & Joe, 1996), defined as

$$Q = \frac{12(3V)^{\frac{2}{3}}}{\sum\limits_{i \neq j} L_{ij}^2}, \tag{C 1}$$

where V is the volume of tetrahedron and L_{ij} are the lengths of its edges. Note that $0 < Q \leq 1$ and $Q = 1$ for a regular tetrahedron.

One additional modification is applied to this algorithm in the spherical geometry.

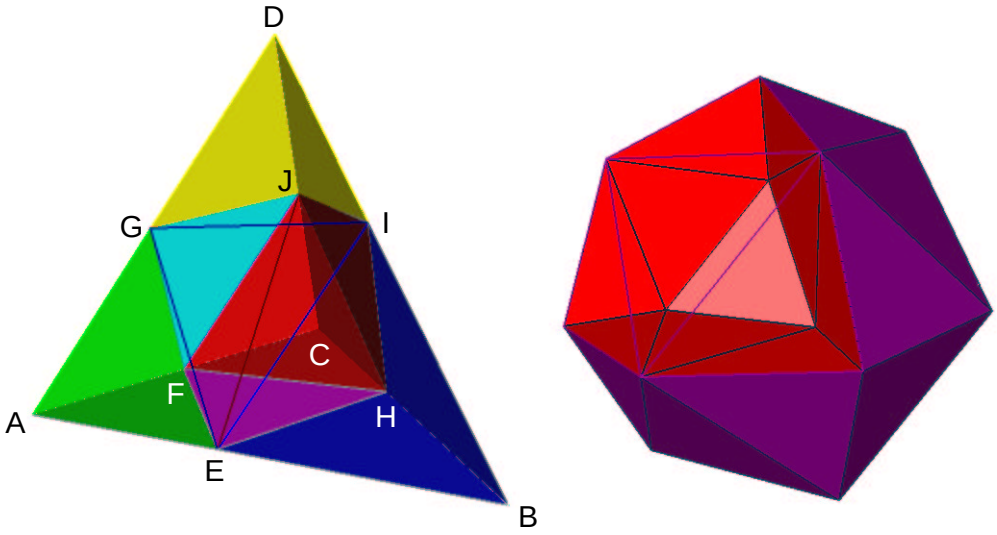

Figure C 1: Left: Subdivision of a tetrahedron into eight subtetrahedra used in the generation of the interior mesh. Right: Initial approximation of the Earth's mantle and application of the first level of subdivision. The innermost tetrahedra shown by pink color are removed from the discretized domain.

Instead of placing the new vertex, let us say E, exactly in the middle of edge AB,

$$\boldsymbol{r}_E = \frac{1}{2}(\boldsymbol{r}_A + \boldsymbol{r}_B), \tag{C 2}$$

we translate the new node along radius so that its radial distance is an average of radial distances of its parents. In other words, we replace equation (C 2) by

$$\boldsymbol{r}_E = \frac{1}{2}(|\boldsymbol{r}_A| + |\boldsymbol{r}_B|)\frac{(\boldsymbol{r}_A + \boldsymbol{r}_B)}{|\boldsymbol{r}_A + \boldsymbol{r}_B|}. \tag{C 3}$$

This assures that all nodes of the resulting interior mesh are placed on concentric spherical surfaces, and the inner and outer boundaries of the discretized spherical shell are well approximated.

The discretization of the Earth's mantle is started from eight tetrahedra. There are seven vertices in this initial state, one is placed in the centre, one at each pole, and four vertices are regularly distributed along the equator. When the first level of recursive subdivision is applied, as shown in the right panel of Figure C 1, eight innermost subtetrahedra representing the core are removed and the inner boundary is created. Since the radius of the Earth's core is only slightly greater than one half of the Earth's radius,

$$a_{CMB} \doteq 0.546\, a, \tag{C 4}$$

the vertices on the inner boundary can be placed at the radial distance a_{CMB} without impairing the mesh quality considerably. Then the subdivision algorithm is recursively

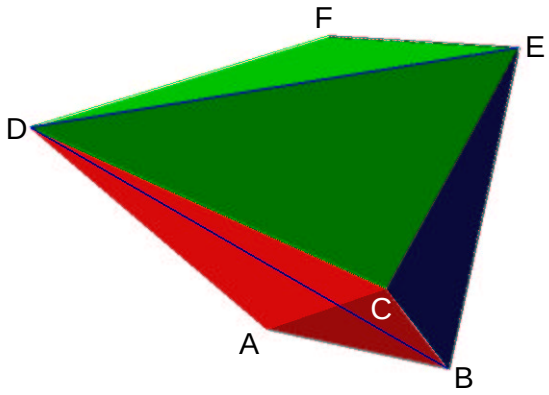

Figure C 2: Subdivision of a triangular prism into three subtetrahedra used in the generation of the exterior mesh.

applied, until required spatial resolution is reached. For the level of recursion l, there are N_n^i nodes and N_t^i tetrahedra of the interior mesh,

$$N_n^i = \frac{1}{6}\left(7\,8^l + 15\,4^l + 8\,2^l\right) + 2, \tag{C 5}$$

$$N_t^i = 7\,8^l, \tag{C 6}$$

of which N_n^c nodes are on the interior surface ∂G_1 and N_t^c tetrahedra have one triangular facet on ∂G_1,

$$N_n^c = 4^l + 2, \tag{C 7}$$

$$N_t^c = 2\,4^l. \tag{C 8}$$

The mantle-atmosphere boundary $\partial G_2 \equiv \partial A_1$ is approximated by N_n^s nodes and N_t^s triangles,

$$N_n^s = 4^{l+1} + 2, \tag{C 9}$$

$$N_t^s = 2\,4^{l+1}. \tag{C 10}$$

The exterior mesh consists of n concentric spherical shells with interfaces placed at $a = r_0 < r_1 < \ldots < r_n = a_O$. The discretization of each shell is based on the triangulation of its inner surface. The outer surface is created by projecting the vertices from the inner surface (A, B, and C in Figure C 2) along radius to the outer surface (D, E, and F),

$$\boldsymbol{r}_{\{D,E,F\}} = \frac{r_{k+1}}{r_k}\,\boldsymbol{r}_{\{A,B,C\}}. \tag{C 11}$$

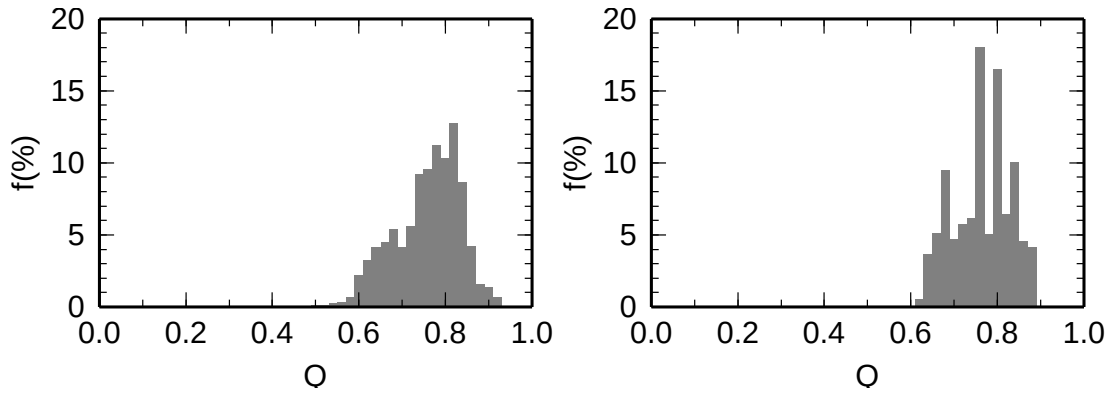

Figure C 3: Quality of the interior (left panel) and exterior (right panel) mesh. Histogram of Q defined by (C 1) is shown for regular mesh $M_{5,20}$ (see Table C.1).

Addition of edges in radial direction divides the shell into triangular prisms ($ABCDEF$). By creating an additional edge at each tetragonal facet of the prism, a subdivision into three tetrahedra is obtained. This algorithm is started from the triangulation of the innermost boundary at a which is taken from the discretization of the interior mesh introduced above.

Since the number of tetrahedra in each shell of the exterior mesh is the same, the thickness of the shell should increase with radius in order to keep good tetrahedra quality throughout the domain. We use a recursive formula

$$r_k - r_{k-1} = f\, r_{k-1}\, \frac{\pi}{2^{l+1}}. \tag{C 12}$$

It defines the thickness of the shell which is also the length of the edges in the radial direction, as an f-multiple of the length of the horizontal edge on the equator. Here l is the refinement level of the interior mesh.

One can immediately see that the exterior mesh comprises of N_n^e nodes and N_t^e tetrahedra,

$$N_n^e = (n+1)\, N_n^s, \tag{C 13}$$
$$N_t^e = 3n\, N_t^s, \tag{C 14}$$

including N_n^s nodes and N_t^s tetrahedra with a boundary facet on ∂A_1, and N_n^o nodes and N_t^o tetrahedra with a boundary facet on ∂A_2,

$$N_n^o = N_n^s, \tag{C 15}$$
$$N_t^o = N_t^s. \tag{C 16}$$

Figure C 3 shows the histograms of the quality parameter Q of the interior and exterior meshes for the highest resolution that is used in the examples presented in Chapter 3.

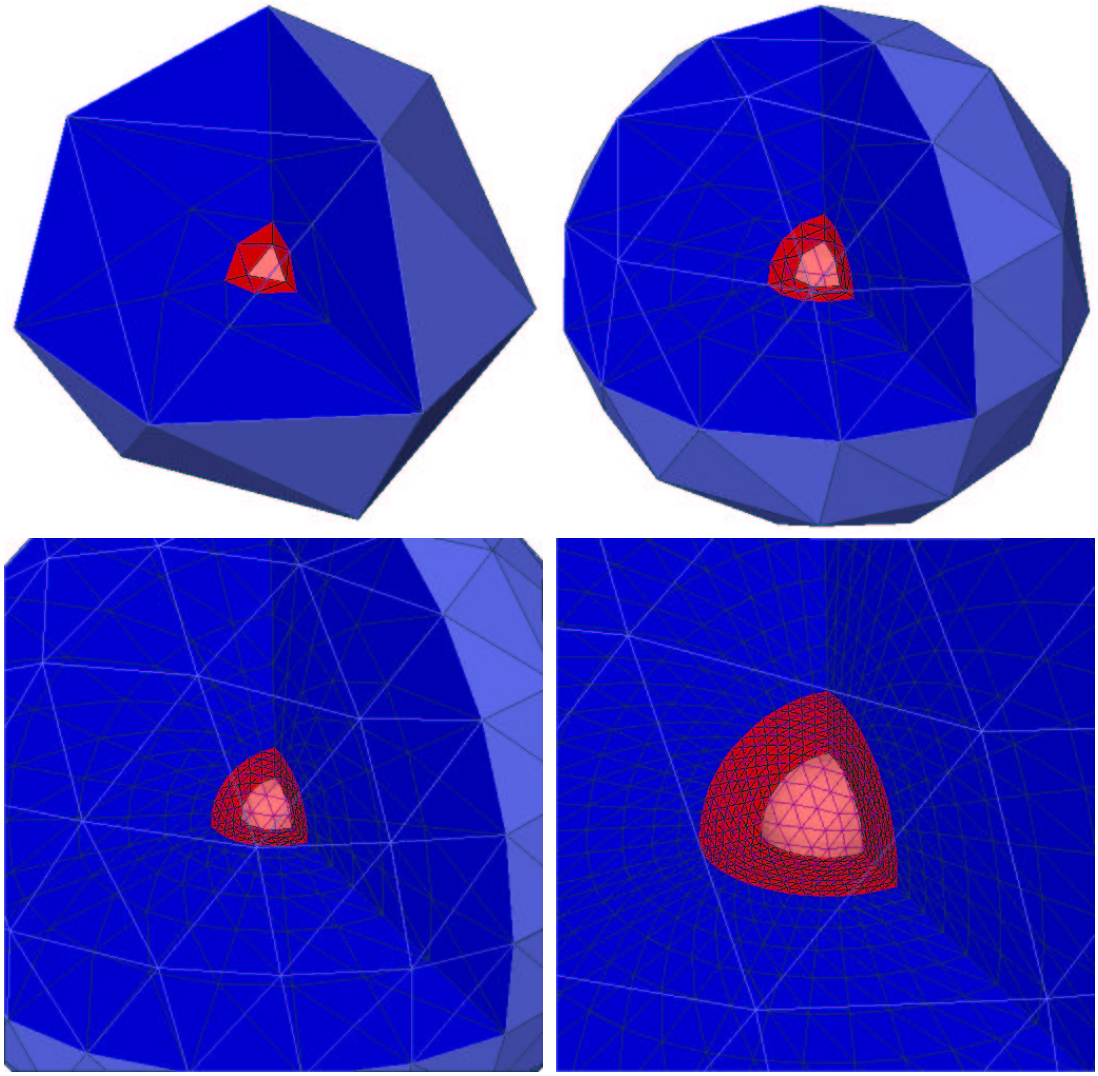

Figure C 4: Regular interior (red) and exterior (blue) meshes at various resolution. Upper left: $l = 1$, $n = 2$. Upper right: $l = 2$, $n = 3$. Bottom left: $l = 3$, $n = 6$. Bottom right: $l = 4$, $n = 10$.

The main advantage of the finite-element methods over spectral methods is the possibility of local refinement that increases the resolution in areas of particular interest. Our implementation is based on the same algorithm by Liu & Joe (1996) that is used in the generation of the interior mesh. Firstly, we select an area where increased resolution is required and for each node of the mesh we decide whether it is inside or outside the selected area. Tetrahedra with all four vertices located inside the refinement zone are divided into eight subtetrahedra (Figure C 1). In order to keep the mesh conforming, particular attention is required at the boundary of the refinement area. Tetrahedra with

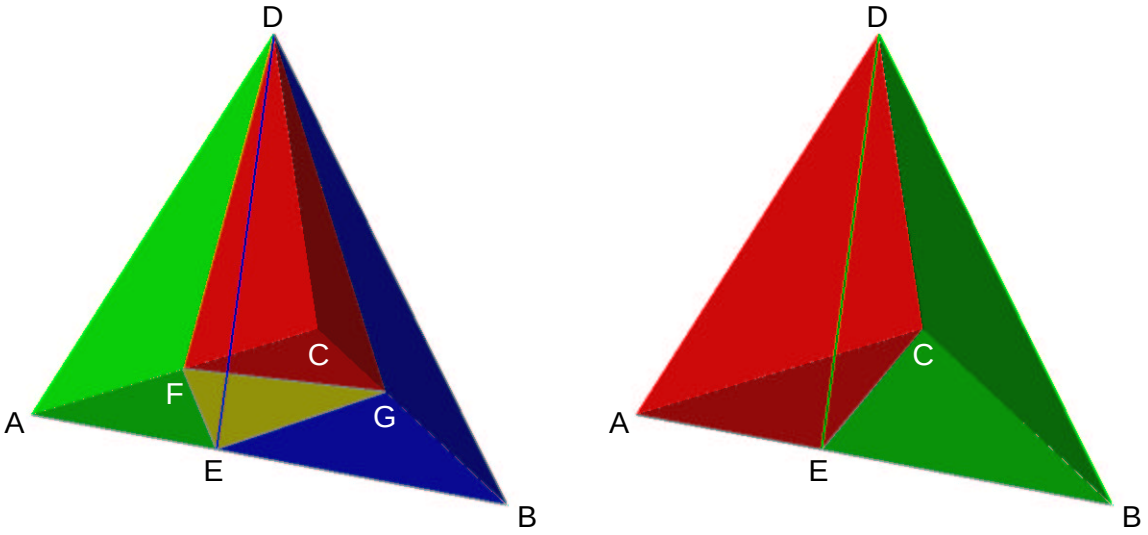

Figure C 5: Local refinement at the boundary of the refinement area. Left: Vertices A, B, C are inside, four new tetrahedra are created. Right: Only vertices A and B are inside, the original tetrahedron is split in two.

only three and two vertices in the refinement area are divided into four and two subtetrahedra, respectively, as is shown in Figure C 5. Tetrahedra with one, or zero vertices inside are not refined. Again, all new nodes added during the refinement procedure are created using the formula (C 3), rather than at the edges' midpoints (C 2).

Although the local refinement can be applied repeatedly, the quality of the tetrahedra at the boundary of the refinement zone necessarily deteriorates, as can be seen from comparison of Q histograms in Figures C 3 and C 6. This represents a trade-off between a well conditioned problem with large dimension and a low dimension problem, with an ill-conditioned matrix that can take long time, or even fail, to invert.

Mesh	l	n	f	a_O	**Local refinement**	d_x
$M_{5,20}$	5	20	1.5	$4.068\,a$	NO	241192
$M_{5,33}$	5	33	1.5	$10.245\,a$	NO	294466
$M^r_{4,10}$	4	10	1.5	$3.816\,a$	$(3500\,\mathrm{km} \le r \le 6871\,\mathrm{km}) \wedge$ $\wedge(10^\circ \le \vartheta \le 70^\circ) \wedge$ $\wedge(5^\circ \le \varphi \le 65^\circ)$	36300
$M^r_{5,20}$	5	20	1.5	$4.068\,a$	$(3500\,\mathrm{km} \le r \le 6871\,\mathrm{km}) \wedge$ $\wedge(10^\circ \le \vartheta \le 70^\circ) \wedge$ $\wedge(5^\circ \le \varphi \le 65^\circ)$	290398

Table C.1: Overview of meshes used in validation examples in Chapter 3. By l, n, f, a_0, and d_x we respectively denote the recursion level used in the generation of the interior mesh, number of layers of the exterior mesh, thickening factor of the exterior mesh, resulting radius of the outer boundary ∂A_2 (in multiples of the Earth's radius), and the resulting dimension of the FE matrix $\mathcal{A}$ (3.61). The intervals in the "Local refinement" column define the neighbourhood of the spherical inclusion, where one additional level of local refinement was applied. The refinement zone spans over parts of both the interior and exterior meshes.

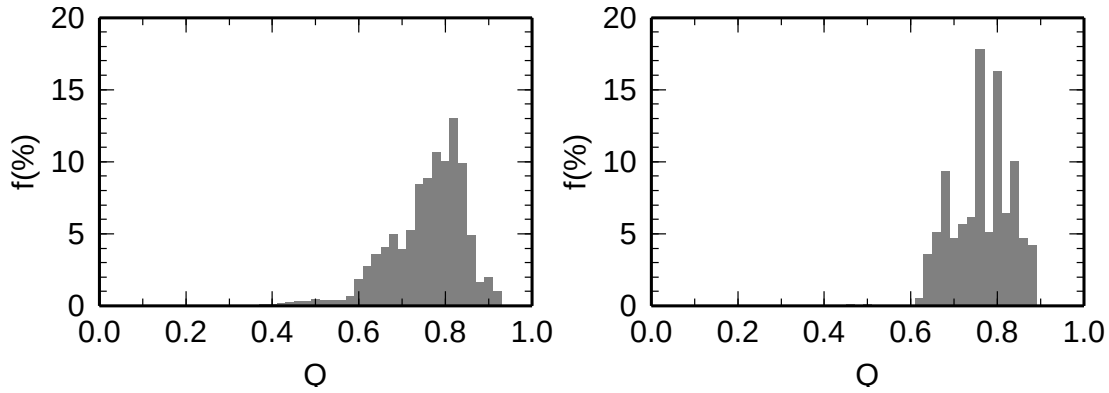

Figure C 6: Quality of the interior (left panel) and exterior (right panel) mesh. Histogram of Q defined by (C 1) is shown for a locally refined mesh $M^r_{5,20}$ (see Table C.1).

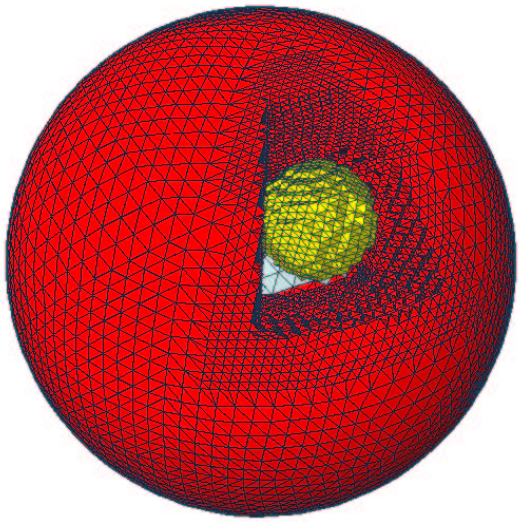

Figure C 7: Interior part of the mesh $M^r_{5,20}$. Note the local refinement applied in the vicinity of the nested spherical inclusion.

Appendix D

Nodal finite element functions

In this appendix we define the 3-D piecewise linear finite elements defined on a tetrahedral grid that are used in Chapter 3 to construct a finite-dimensional approximation of Sobolev spaces $W_{01}^{1,2,h}(G)^k$, $W_{02}^{1,2,h}(A)$, and $W^{1,2,h}(A)$ (see Table F.2). We also introduce particular formulae for volume and surface integrals of finite element products.

We start with the definition of nodal finite element functions. Let $\boldsymbol{r}_q = (x_q, y_q, z_q)$ be the q-th node of a tetrahedral mesh. We assign it a finite element Ψ_q defined in each tetrahedron as a linear function of x, y, and z that satisfies

$$\Psi_q(x_p, y_p, z_p) = \delta_{pq}. \tag{D 1}$$

One can immediately see that Ψ_q is non-zero only in those tetrahedra that include the q-th vertex, and that in each tetrahedron there are only four non-zero finite elements, each assigned to one of its vertices.

In order to obtain particular forms of finite element functions and their first derivatives, it is useful to introduce the reference tetrahedron (Křížek & Neittaanmäki, 1990). Let $\boldsymbol{r}' = (\eta, \xi, \zeta)$ be the position vector in a local Cartesian coordinate system. In this coordinate system we define the reference tetrahedron $KLMN$ by positioning its vertices at

$$\begin{aligned} \boldsymbol{r}'_k &= (0,0,0), \\ \boldsymbol{r}'_l &= (1,0,0), \\ \boldsymbol{r}'_m &= (0,1,0), \\ \boldsymbol{r}'_n &= (0,0,1), \end{aligned} \tag{D 2}$$

as is shown in Figure D 1. For each tetrahedron T_κ, given by vertices $\boldsymbol{r}_k$, $\boldsymbol{r}_l$, $\boldsymbol{r}_m$, and $\boldsymbol{r}_n$ ($k \neq l \neq m \neq n$), we can define an affine mapping from the local coordinates to the global ones,

$$\boldsymbol{r} = \boldsymbol{r}_k + R_\kappa \cdot \boldsymbol{r}', \tag{D 3}$$

where the matrix R_κ is given by

$$R_\kappa = (\boldsymbol{r}_l - \boldsymbol{r}_k, \boldsymbol{r}_m - \boldsymbol{r}_k, \boldsymbol{r}_n - \boldsymbol{r}_k)\,. \tag{D 4}$$

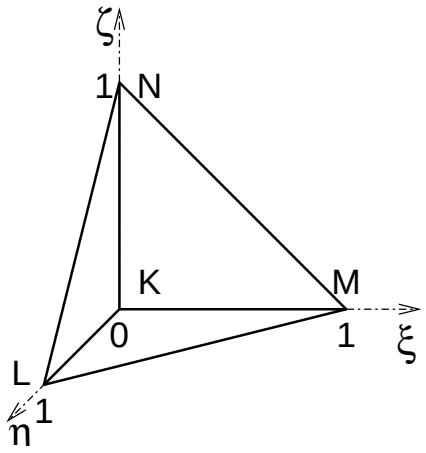

Figure D 1: Reference tetrahedron in local coordinates (η, ξ, ζ).

To each vertex of the reference tetrahedron we assign a finite element function according to D 1,

$$\begin{aligned} \Psi'_k(\boldsymbol{r}') &= 1 - \eta - \xi - \zeta, \\ \Psi'_l(\boldsymbol{r}') &= \eta, \\ \Psi'_m(\boldsymbol{r}') &= \xi, \\ \Psi'_n(\boldsymbol{r}') &= \zeta. \end{aligned} \tag{D 5}$$

The first order derivatives of the reference finite elements expressed in the local coordinate system are,

$$\begin{aligned} \mathrm{grad}\,'\Psi'_k(\boldsymbol{r}') &= (-1, -1, -1), \\ \mathrm{grad}\,'\Psi'_l(\boldsymbol{r}') &= (1, 0, 0), \\ \mathrm{grad}\,'\Psi'_m(\boldsymbol{r}') &= (0, 1, 0), \\ \mathrm{grad}\,'\Psi'_n(\boldsymbol{r}') &= (0, 0, 1). \end{aligned} \tag{D 6}$$

Since the transformation (D 3) is linear, we can write

$$\Psi_q(\boldsymbol{r}) = \Psi'_q(\boldsymbol{r}'), \tag{D 7}$$

$$\mathrm{grad}\,\Psi_q(\boldsymbol{r}) = R_\kappa^{-T} \cdot \mathrm{grad}\,'\Psi'_q(\boldsymbol{r}'), \tag{D 8}$$

where $q \in \{k, l, m, n\}$ and R_κ^{-T} denotes the inverse transpose matrix to R_κ.

Now we can easily express the products of the finite elements and their derivatives, integrated over the tetrahedron. Namely, for each tetrahedron T_κ and for each pair of

finite elements Ψ_p, Ψ_q that are non-zero on T_κ, we define

$$\begin{aligned} I_\kappa^{pq} &= \int\limits_{T_\kappa} \Psi_p \, \Psi_q \, dV = |\det R_\kappa| \int\limits_{T'_\kappa} \Psi'_p \, \Psi'_q \, dV' = \\ &= \frac{1}{120} \, |\det R_\kappa| \, (1 + \delta_{pq}) \quad \text{for } \boldsymbol{r}_p, \boldsymbol{r}_q \in T_\kappa, \qquad \text{(D 9)} \\ \boldsymbol{J}_\kappa^{pq} &= \int\limits_{T_\kappa} \Psi_p \operatorname{grad} \Psi_q \, dV = |\det R_\kappa| \, R_\kappa^{-T} \cdot \operatorname{grad}' \Psi'_q \int\limits_{T'_\kappa} \Psi'_p \, dV' = \\ &= \frac{1}{24} \, |\det R_\kappa| \, R_\kappa^{-T} \cdot \operatorname{grad}' \Psi'_q \quad \text{for } \boldsymbol{r}_p, \boldsymbol{r}_q \in T_\kappa, \qquad \text{(D 10)} \\ K_\kappa^{pq} &= \int\limits_{T_\kappa} \operatorname{grad} \Psi_p \cdot \operatorname{grad} \Psi_q \, dV = \\ &= |\det R_\kappa| \, (R_\kappa^{-T} \cdot \operatorname{grad}' \Psi'_p) \cdot (R_\kappa^{-T} \cdot \operatorname{grad}' \Psi'_q) \int\limits_{T'_\kappa} dV' = \\ &= \frac{1}{6} \, |\det R_\kappa| \, (R_\kappa^{-T} \cdot \operatorname{grad}' \Psi'_p) \cdot (R_\kappa^{-T} \cdot \operatorname{grad}' \Psi'_q) \quad \text{for } \boldsymbol{r}_p, \boldsymbol{r}_q \in T_\kappa. \qquad \text{(D 11)} \end{aligned}$$

We will also express the surface integrals of finite elements over the mantle-atmosphere interface $\partial G_2 \equiv \partial A_1$. The interface is approximated by triangular facets $F_\eta \subset T_\kappa$. For each facet F_η we define the unit normal $\boldsymbol{n}_\eta$ pointing approximately in the radial direction, $\boldsymbol{n}_\eta \approx \boldsymbol{e}_r$ on F_η (note that $\boldsymbol{e}_r$ is not constant on F_η). Thus we approximate the outer normals $\boldsymbol{n} \approx \boldsymbol{n}_\eta$ on ∂G_2 and $\boldsymbol{n} \approx -\boldsymbol{n}_\eta$ on ∂A_1. Then we can introduce integrals

$$\begin{aligned} \boldsymbol{L}_\eta^{pq} &= \int\limits_{F_\eta} \Psi_p \, \boldsymbol{n}_\eta \times \operatorname{grad} \Psi_q \, dS = \\ &= \frac{1}{3} \, |F_\eta| \, \boldsymbol{n}_\eta \times \left(R_\kappa^{-T} \cdot \operatorname{grad}' \Psi'_q \right) \quad \text{for } \boldsymbol{r}_p, \boldsymbol{r}_q \in F_\eta, \qquad \text{(D 12)} \end{aligned}$$

where $|F_\eta|$ is the surface of facet F_η. Although $\operatorname{grad} \Psi_q$ is non-zero on F_η also for the finite element corresponding to node $\boldsymbol{r}_q \in T_\kappa \setminus F_\eta$, it is parallel to $\boldsymbol{n}_\eta$ since $\Psi_q = 0$ on F_η. Note that

$$\boldsymbol{e}_x \cdot \boldsymbol{L}_\eta^{pq} = \int\limits_{F_\eta} \Psi_p \, \boldsymbol{n}_\eta \cdot \operatorname{curl} (\Psi_q \, \boldsymbol{e}_x) \, dS, \qquad \text{(D 13)}$$

and similarly for $\boldsymbol{e}_y \cdot \boldsymbol{L}_\eta^{pq}$ and $\boldsymbol{e}_z \cdot \boldsymbol{L}_\eta^{pq}$. This allows to express the surface integrals in both equations (3.48) and (3.50) by means of $\boldsymbol{L}_\eta^{pq}$.

Finally, it is possible to show that

$$\boldsymbol{L}_{\eta_1}^{pq} + \boldsymbol{L}_{\eta_1}^{qp} = - \left(\boldsymbol{L}_{\eta_2}^{pq} + \boldsymbol{L}_{\eta_2}^{qp} \right), \qquad \text{(D 14)}$$

for any neighbouring facets F_{η_1}, F_{η_2} with common vertices $\boldsymbol{r}_p, \boldsymbol{r}_q \in F_{\eta_1} \cap F_{\eta_2}$, $p \neq q$, since both expression depend only on $\boldsymbol{r}_q - \boldsymbol{r}_p$. Due to this relation the surface integrals do not violate symmetry of matrices $\mathcal{A}$, $\mathcal{B}$ (3.63–3.64).

Appendix E

Moving least squares interpolation

The solution of the 3-D finite element formulation of the EM induction problem introduced in Chapter 3 is obtained in the form of electromagnetic potentials $\boldsymbol{A}$, Φ, and U. To express the solution by means of a quantity measurable by ground based and satellite born magnetometers, the magnetic induction vector $\boldsymbol{B}$, the first order derivatives of potentials, namely $\operatorname{curl} \boldsymbol{A}$ and $\operatorname{grad} U$ are needed. The potentials are parameterized by piecewise linear base functions with piecewise constant analytical derivatives. Therefore, the magnetic induction $\boldsymbol{B}$ obtained by direct differentiation of the base functions would change discontinuously across the boundaries of neighbouring tetrahedra. We prefer instead the moving least squares method (MLS) which is used for numerical differentiation of irregularly sampled fields in fluid dynamics (Gossier, 2001).

The MLS method is based on approximation of a scalar function $f(x, y, z)$ in the vicinity of a point (x_0, y_0, z_0) by a polynomial $\tilde{f}$ of j-th order,

$$f(x,y,z) \approx \tilde{f}(x,y,z) = \sum_{k,l,m\geq 0}^{k+l+m=j} f_{klm} \left(\frac{x-x_0}{a}\right)^k \left(\frac{y-y_0}{a}\right)^l \left(\frac{z-z_0}{a}\right)^m, \qquad \text{(E 1)}$$

where the Earth's radius is a natural choice for the scaling factor a. Let gridpoints (x_i, y_i, z_i), $i = 1, \ldots, n$ be the n nearest neighbours of point (x_0, y_0, z_0). The values $f_i = f(x_i, y_i, z_i)$ are known. Then we determine the coefficients f_{klm} of the polynomial (E 1) by minimizing the least squares misfit

$$\chi^2 = \sum_{i=1}^{n} w_i \left(f_i - \tilde{f}(x_i, y_i, z_i)\right)^2 = \min, \qquad \text{(E 2)}$$

where the importance of each node can be optionally weighted by w_i, usually a decreasing function of distance from (x_0, y_0, z_0).

Problem (E 1–E 2) can be easily arranged in a matrix form. The condition number of the least squares matrix depends on the number and position of neighbours and often the matrix is ill conditioned. Following Press et al. (1992) we use the singular value decomposition (SVD) method to obtain the minimum norm solution of (E 1–E 2). During this process, the non-significant data can be detected by their small singular values and excluded from the fit. Once the coefficients f_{klm} are found, the first-order derivatives of

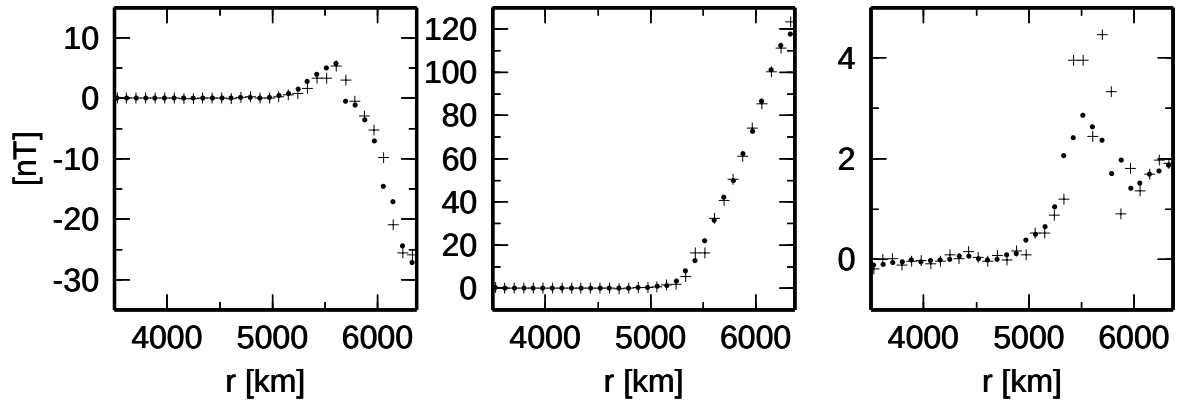

Figure E 1: The high-resolution FE solution at $t = 72$ h for nested spheres conductivity model (see Figure 3.5 for details) obtained by direct differentiation of base functions (shown by crosses) and by MLS fit of quadratic polynomials into 10 nearest neighbours (dots). Note the large oscillation of the B_φ component (right plate) yielded by the former method.

$\tilde{f}$ at (x_0, y_0, z_0) are simply,

$$\left.\frac{\partial \tilde{f}}{\partial x}\right|_{(x_0,y_0,z_0)} = f_{100}, \tag{E 3}$$

$$\left.\frac{\partial \tilde{f}}{\partial y}\right|_{(x_0,y_0,z_0)} = f_{010}, \tag{E 4}$$

$$\left.\frac{\partial \tilde{f}}{\partial z}\right|_{(x_0,y_0,z_0)} = f_{001}. \tag{E 5}$$

Applying the MLS method on A_x, A_y, A_z in the Earth's mantle and on U in the insulating surroundings yields the magnetic induction vector $\boldsymbol{B}$. Detailed discussion of importance of various parameters on the MLS fit can be found in Gossier (2001). We experienced best results by using non-weighted ($w_i = 1$) fit of a quadratic polynomial ($j = 2$) into $n = 10$ neighbours. An example comparing the induction vector $\boldsymbol{B}$ obtained by direct differentiation of base functions and by MLS fit is shown in figure E 1.

Appendix F

Notation

F.1 Used symbols

$\boldsymbol{r}$	position vector
(r, ϑ, φ)	spherical coordinates: radius ($r \geq 0$), colatitude ($0 \leq \vartheta \leq \pi$), and longitude ($0 \leq \varphi \leq 2\pi$)
Ω	abbreviated notation of angular coordinates, $\Omega = (\vartheta, \varphi)$
(x, y, z)	Cartesian coordinates
$\boldsymbol{e}_r, \boldsymbol{e}_\vartheta, \boldsymbol{e}_\varphi$	unit base vectors of spherical coordinate system
$\boldsymbol{e}_x, \boldsymbol{e}_y, \boldsymbol{e}_z$	unit base vectors of Cartesian coordinate system
G	computational domain filled with conductor (sphere or spherical shell)
∂G	boundary of G; if G is a spherical shell, then $\partial G = \partial G_1 \cup \partial G_2$, where ∂G_1, ∂G_2 is the inner and the outer boundary, respectively
A	spherical shell surrounding G which is filled with insulator
∂A	boundary of A, $\partial A = \partial A_1 \cup \partial A_2$, where ∂A_1, and ∂A_2 is the inner and the outer boundary, respectively
$\boldsymbol{n}$	outer normal to a boundary; in spherical geometry $\boldsymbol{n} = \boldsymbol{e}_r$ on $\partial G_2 \cup \partial A_2$, while $\boldsymbol{n} = -\boldsymbol{e}_r$ on $\partial G_1 \cup \partial A_1$
a	Earth's radius, $a = 6371\,\mathrm{km}$
a_{CMB}	radius of the Core-Mantle boundary, $a_{CMB} \doteq 0.546\,a$
a_O	radius of the outermost boundary ∂A_2
$Y_{jm}(\Omega)$	scalar spherical harmonic functions
$\boldsymbol{S}^{(\lambda)}_{jm}(\Omega)$	vector spherical harmonic functions
$\psi_k(r)$	piecewise linear 1-D nodal finite elements
$\Psi_k(\boldsymbol{r})$	piecewise linear 3-D nodal finite elements defined on a tetrahedral grid

$\chi_k(r)$	piecewise linear functions based on $\psi_k(r)$ to express $\operatorname{curl} \psi_k(r)\, \boldsymbol{S}_{jm}^{(\lambda)}(\Omega)$
t, Δt	time, time-step (s)
σ	electrical conductivity ($^{\mathrm{S}}/_{\mathrm{m}}$)
ρ	electrical resistivity ($\Omega\,\mathrm{m}$)
μ_0	magnetic permeability, $\mu_0 = 4\,\pi\,10^{-7}\,{}^{\mathrm{H}}/_{\mathrm{m}}$
$\boldsymbol{B}$	magnetic induction vector (T)
$\boldsymbol{H}$	magnetic field intensity vector ($^{\mathrm{A}}/_{\mathrm{m}}$)
$\boldsymbol{E}$	electrical field intensity vector ($^{\mathrm{V}}/_{\mathrm{m}}$)
$\boldsymbol{j}$	electrical current density vector ($^{\mathrm{A}}/_{\mathrm{m}^2}$)
$\boldsymbol{j}^{(e)}$	electrical current density of primary inducing field of external origin ($^{\mathrm{A}}/_{\mathrm{m}^2}$)
$\boldsymbol{j}_S$	electrical current surface density vector ($^{\mathrm{A}}/_{\mathrm{m}}$)
$\boldsymbol{A}$	vector magnetic potential (A)
U	scalar magnetic potential (A)
$U^{(e)}$, $U^{(i)}$	scalar magnetic potential of external (primary, inducing) and internal (secondary, induced) field
ϕ	scalar electrical potential (V)
Φ	time-integrated scalar electrical potential (V s)

F.2 Overview of functional spaces

$C(G)^k$	space of scalar ($k = 1$) and vector ($k = 3$) functions continuous on the domain G
$C^n(G)^k$	space of scalar ($k = 1$) and vector ($k = 3$) functions whose classical derivatives up to the n-th order belong to $C(G)^k$
$C^1\left(\langle 0, \infty)\right)^k$	space of scalar ($k = 1$) and vector ($k = 3$) functions continuously differentiable with respect to t on interval $\langle 0, \infty)$
$D^0(G)$	space of smooth (infinitely differentiable) scalar functions with compact support in G which are zero on ∂G
$L_2(G)^k$	space of scalar ($k = 1$), vector ($k = 3$), and tensor ($k = 9$) functions

that are square-integrable in G; the scalar products

$$\begin{aligned}(f,g) &= \int_G f\,g\,dV,\\ (\boldsymbol{f},\boldsymbol{g}) &= \int_G \boldsymbol{f}\cdot\boldsymbol{g}\,dV,\end{aligned}$$

of functions from $L_2(G)^1$ and $L_2(G)^3$, respectively, induce the norms

$$\begin{aligned}||f||_{L_2} &= (f,f)^{\frac{1}{2}},\\ ||\boldsymbol{f}||_{L_2} &= (\boldsymbol{f},\boldsymbol{f})^{\frac{1}{2}}\end{aligned}$$

$L_\infty^+(G)$ space of positive ($f > 0$) scalar functions bounded in G; the norm in $L_\infty^+(G)$ is defined as

$$||f||_{L_\infty} = \max_G |f|$$

$W^{1,2}(G)^k$ Sobolev's space of scalar ($k = 1$) and vector ($k = 3$) functions from $L_2(G)^k$ whose partial derivatives belong to $L_2(G)^{3k}$; the scalar products

$$\begin{aligned}(f,g)_{W^{1,2}} &= \int_G [f\,g + \operatorname{grad} f\cdot\operatorname{grad} g]\;dV,\\ (\boldsymbol{f},\boldsymbol{g})_{W^{1,2}} &= \int_G \left[\boldsymbol{f}\cdot\boldsymbol{g} + \operatorname{grad}\boldsymbol{f} : (\operatorname{grad}\boldsymbol{g})^T\right]\;dV,\end{aligned}$$

of functions from $W^{1,2}(G)^1$ and $W^{1,2}(G)^3$, respectively, induce the norms

$$\begin{aligned}||f||_{W^{1,2}} &= (f,f)^{\frac{1}{2}}_{W^{1,2}},\\ ||\boldsymbol{f}||_{W^{1,2}} &= (\boldsymbol{f},\boldsymbol{f})^{\frac{1}{2}}_{W^{1,2}}\end{aligned}$$

$W_{01}^{1,2}(G)^k$ space of scalar ($k = 1$) and vector ($k = 3$) functions from $W^{1,2}(G)^k$ that are zero on the inner boundary ∂G_1

$W_{02}^{1,2}(A)$ space of scalar functions from $W^{1,2}(A)$ that are zero on the outer boundary ∂A_2

H_{curl} space of vector functions from $L_2(G)^3$ whose rotation also belongs to $L_2(G)^3$; the scalar product

$$(\boldsymbol{f},\boldsymbol{g})_{H_{\mathrm{curl}}} = \int_G [\boldsymbol{f}\cdot\boldsymbol{g} + \operatorname{curl}\boldsymbol{f}\cdot\operatorname{curl}\boldsymbol{g}]\;dV,$$

induces the norm

$$|\boldsymbol{f}||_{H_{\mathrm{curl}}} = (\boldsymbol{f},\boldsymbol{f})^{\frac{1}{2}}_{H_{\mathrm{curl}}}$$

$H_{\mathrm{curl},0}$ space of vector functions from H_{curl} whose tangential component is zero on the boundary ∂G